

# The Problem of Two Fixed Centers: Bifurcations, Actions, Monodromy

Holger Waalkens<sup>a,b,\*</sup>, Holger R. Dullin<sup>a,c</sup>, and Peter H. Richter<sup>a</sup>

<sup>a</sup> Institut für Theoretische Physik, Universität Bremen, Germany

<sup>b</sup> School of Mathematics, University of Bristol, UK

<sup>c</sup> Mathematical Sciences, Loughborough University, UK

March 20, 2006

## Abstract

A comprehensive analysis of the Euler-Jacobi problem of motion in the field of two fixed attracting centers is given, first classically and then quantum mechanically in semiclassical approximation. The system was originally studied in the context of celestial mechanics but, starting with Pauli's dissertation, became a model for one-electron molecules such as  $\text{H}_2^+$  (symmetric case of equal centers) or  $\text{HHe}^{2+}$  (asymmetric case of different centers). The present paper deals with arbitrary relative strength of the two centers and considers separately the planar and the three-dimensional problems. All versions represent non-trivial examples of integrable dynamics and are studied here from the unifying point of view of the energy momentum mapping from phase space to the space of integration constants. The interesting objects are the critical values of this mapping, i. e., its bifurcation diagram, and their pre-images which organize the foliation of phase space into Liouville-Arnold tori. The classical analysis culminates in the explicit derivation of the action variable representation of iso-energetic surfaces. The attempt to identify a system of global actions, smoothly dependent on the integration constants wherever these are non-critical, leads to the detection of monodromy of a special kind which is here described for the first time. The classical monodromy has its counterpart in the quantum version of the two-center problem where it prevents the assignments of unique quantum numbers even though the system is separable.

PACS: 05.45.-a Nonlinear dynamics and nonlinear dynamical systems

03.65.Sq Semiclassical theories and applications

31.10.+z Theory of electronic structure, electronic transitions, and chemical binding

**Keywords:** Two-center problem; Integrable systems; Action variables; Monodromy

---

\* Corresponding author. Fax: +44-117-928-7999.

E-mail address: H.Waalkens@bris.ac.uk (H. Waalkens)

## 1 Introduction

The two-center problem was first considered by Euler in 1760 and is without question one of the most famous integrable problems of classical mechanics. It describes the motion of a test particle in the field of two space fixed Newtonian centers of attraction. Jacobi showed that the equations of motion can be integrated in terms of elliptic functions; explicit solutions are given in his “Vorlesungen über Dynamik” [33].

The system has played an important role as a model both in the macroscopic and in the microscopic world. In celestial mechanics it represents the motion of a test particle which is attracted by two space fixed stars. Charlier used this admittedly unrealistic situation as a starting point for a discussion of the restricted three-body problem [13]. In molecular physics the two centers are atomic nuclei and the test particle is an electron; this is the simplest model of a diatomic molecule. The assumption that the nuclei are fixed (their distance being an important parameter in quantum mechanics) is known, in this context, as Born-Oppenheimer approximation. Pauli, then a student of Sommerfeld, applied the model to the hydrogen molecular ion  $\text{H}_2^+$  in his doctoral thesis [43]. This work was completed in 1922, well before Schrödinger’s formulation of wave mechanics in 1926, hence it was conceived in the spirit of old quantum mechanics, i. e., action quantization. At that time it was not well understood why action quantization worked for some systems while it failed for others, even though Einstein [26] had effectively pointed out as early as 1917 that a system must be integrable for this quantization to work.

From this point of view, Pauli had made a good choice because the problem of two fixed centers is separable and therefore Liouville integrable. The brilliance of Pauli’s work is only slightly diminished by his wrong prediction that the hydrogen molecular ion can at best exist in a metastable state. The reasons for this failure are three-fold: (i) the concept of Liouville-Arnold tori foliating the phase space of a compact integrable system was not clear at the time; (ii) Pauli’s classification of the motion from symmetry principles led him to quantizing the wrong tori (he excluded electronic motion which approaches the nuclei too closely); (iii) he could not know of the correction to naive action quantization in terms of Maslov indices as introduced by Keller [36] a long time after G. Wentzel, H. A. Kramers and L. Brillouin had shown that action quantization is an approximation to Schrödinger’s quantum mechanics [52, 37, 10]. A modern treatment incorporating these aspects was presented by M. P. Strand and W. P. Reinhardt [46] and gave excellent semi-classical results for bond length and bond energy, see also [42, 22, 23].

The contribution of the present work is the global picture of how phase space is foliated by invariant tori, the derivation of bifurcation diagrams, an analysis of the energy surfaces in action space, and a pursuit of the question if and how global action variables can be constructed. Classically, the action quantization rests on the Liouville-Arnold theorem which guarantees that most orbits in a Liouville integrable system with  $n$  degrees of freedom are confined to  $n$ -dimensional tori. Such regular tori foliate the bulk of the  $2n$ -dimensional phase space and its  $(2n - 1)$ -dimensional energy surfaces. To understand the global structure of this foliation we need to identify its topological changes, or bifurcations, which involve special tori of lower dimension. The technical tool for achieving this is an analysis of the *energy momentum map*, in particular, the determination of its critical values.

Our system has three commuting integrals: energy, an angular momentum, and a third “momentum like” integral. The critical values are those values of energy and conserved momenta for which the three conserved quantities are not functionally independent. As a consequence, the Liouville-Arnold theorem does not apply at these values. The first, longer, part of this paper deals with the identification of this set of critical values – a stratified subset of  $\mathbb{R}^3$ . This will incorporate the large body of knowledge about the

problem that has accumulated in the course of time. Few special results in this part are original, but the coherent presentation from the point of view of the energy momentum map is new; it organizes all classical results in a comprehensive way.

The possible types of motion in the *planar* two-center problem were already identified by Charlier [13], and more systematically in later work by Deprit [21]. These results belong to the invariant subsystem, with zero angular momentum, of the full problem with three degrees of freedom. We shall analyze in detail how the bifurcations of the planar system are related to the full bifurcation scheme. This will be done for equal and unequal centers of attraction (referred to as *symmetric* and *asymmetric* cases). Recent results by Howard and Wilkerson [32] about saddle-center bifurcations of relative equilibria will be used in this connection. Given the separability of the system in terms of elliptic coordinates, the determination of critical values of the energy momentum map boils down to the analysis of the discriminant surface of a polynomial, i. e., the set of energy and momentum values for which the polynomial has multiple roots.

For each type of motion the actions are identified in terms of elliptic integrals (except for the angular momentum which is an action by itself). Since the Hamiltonian may be expressed as a function of action variables only, it is meaningful to determine the hypersurfaces of constant energy (referred to as *energy surfaces* for short) in the space of these variables. Such energy surfaces in the space of actions are important from two points of view. Geometrically, they are a convenient representation of tori; the normal vectors to these surfaces give the frequencies of the orbits on the corresponding tori, hence they are relevant for stability considerations based on the Kolmogorov-Arnold-Moser theorem. From the point of view of quantum mechanics, discretization of the action space in units of  $\hbar$  is the key to semi-classical spectra of energy and momenta.

It appears natural to use the separating variables for the definition and calculation of actions. The actions so determined are therefore called *natural actions*. On the other hand it is well known that any particular choice of actions corresponds to a certain basis of the homology group of fundamental paths on the invariant tori. The natural actions single out the paths defined by the separating coordinate system, but this system has singularities. As a consequence, the natural actions as functions of energy and momenta may not be smooth at points where there is no bifurcation. This interesting phenomenon is related to a non-trivial *monodromy* of the two-center problem, an obstruction to the existence of global, smooth, and single valued action variables. The possibility in principle of such topological obstructions was first noted by Duistermaat [24]. Since then this has become an active field of investigations, see [18, 55, 15, 19, 20, 45] and the references therein. The two-center problem exhibits monodromy of a particularly interesting kind in the asymmetric case. This is here described for the first time. We calculate the monodromy matrices from an attempt to construct smooth actions from the natural ones. A similar approach for different systems has already been used in [16, 49, 48].

In the last part of this paper we discuss the quantum version of the two-center problem. More than 10 years after Pauli's semi-classical treatment, the Schrödinger equation was applied to the problem by Jaffé [34] and by Baber & Hasse [6]. However, even though their approach is in principle exact, the quantization conditions are obtained from Sturm-Liouville problems in a perturbation analysis near the low-lying Kepler-like states. For this reason the authors could not see the non-trivial global geometry of the quantum spectrum.

There exist three commuting observables corresponding to the classical constants of motion. Quantum states are defined to be simultaneous eigenstates of all three observables and, accordingly, may be labelled by triples of the corresponding eigenvalues. The Einstein-Brillouin-Keller-Maslov quantization of actions gives a surprisingly good account of the exact (numerical) spectra. Noticeable differences arise only in the neighborhood of critical values where the classical bifurcations are reflected in changes of the local lattice

structure of the spectra. Monodromy describes spectral lattices with a non-trivial global topology. This phenomenon is referred to as *quantum monodromy* and was introduced by Cushman and Duistermaat in [31], see also [40, 41, 45, 49]. A short report on the quantum monodromy of the two-center problem has already been given in the letter [50].

The following six sections of this paper are organized as follows. The two-center problem together with its separating coordinates and constants of motion, in two and three dimensions, is introduced in Sec. 2. The planar motion is analyzed in Sec. 3; four types of motion are identified, together with their bifurcation scheme. Particular attention is given to the nature of critical periodic orbits and their stability properties because these are the key structural elements of the phase space organization. Motion in three dimensions, with arbitrary values of the angular motion, is considered in Sec. 4. Even though there are only two topological types of motion, the bifurcation scheme is more involved than in the planar case (which must of course be recovered in the limit of vanishing angular momentum). Since it is practically impossible to give illustrations of the bifurcation set in the 3D-space of energy and momenta, we present various projections and cross sections. Bifurcations in the topology of energy surfaces are discussed in terms of relative equilibria, but there are other bifurcations of the foliation due to changes of critical tori.

Actions are addressed in Sec. 5. We give expressions in terms of elliptic integrals, first for the planar case, then for arbitrary angular momentum. All possible types of energy surfaces in the space of natural actions are discussed. Bifurcations are clearly identified as boundaries of the surfaces or lines with logarithmic divergencies, but in addition there are edges where no critical behavior takes place. This phenomenon is related to monodromy, the subject of Sec. 6. There we attempt to construct actions which are smooth across the edges, and find that this is only piecewise possible; monodromy forbids a global smoothing. The interesting and new feature of the two-center problem is that with non-zero angular momentum, there exist *two* critical objects in the energy momentum space which give rise to monodromy: one a line as usual, the other a line which fans out like a leaf. The consequences of this classical behavior for the quantum mechanical spectra are discussed in Sec. 7. We conclude with a brief summary in Sec. 8.

## 2 Separation and constants of the motion

Given a space fixed Cartesian coordinate system, we assume two fixed centers to be located at  $\mathbf{f}_{1,2} = (0, 0, \mp a)$  on the  $z$ -axis. The equations of motion for a particle of mass  $m$  at  $\mathbf{r} = (x, y, z)$  derive from the Hamiltonian

$$H = \frac{\mathbf{p}^2}{2m} - \frac{\mu_1}{r_1} - \frac{\mu_2}{r_2}, \quad (1)$$

where  $r_1$  and  $r_2$  are the lengths of the vectors  $\mathbf{r}_{1,2} = \mathbf{r} - \mathbf{f}_{1,2}$ . The centers are assumed to be attractive,  $\mu_{1,2} > 0$ . In the gravitational case the parameters are  $\mu_i = GmM_i$  with  $G$  the gravitational constant,  $M_1$  and  $M_2$  the masses of the two fixed stars. In the molecular case  $\mu_i/e = Z_i e$  are the charges of the two nuclei.

We introduce dimensionless variables by measuring distances in units of  $a$ , momenta in units of  $\sqrt{m(\mu_1 + \mu_2)}/a$ , energy in  $(\mu_1 + \mu_2)/a$  and time in  $\sqrt{ma^3}/(\mu_1 + \mu_2)$ . The scaled Hamiltonian then reads

$$\tilde{H} = \frac{\tilde{\mathbf{p}}^2}{2} - \frac{\mu}{\tilde{r}_1} - \frac{1-\mu}{\tilde{r}_2} \quad (2)$$

where tildes denote scaled variables and  $\mu \equiv \mu_1/(\mu_1 + \mu_2) \in (0, 1)$  is a reduced strength of attraction. Since only scaled variables will be used, we omit the tildes in the following. Without restriction we may assume  $\mu \leq 1/2$ , i. e., the stronger center is at the top  $\mathbf{f}_2$ .

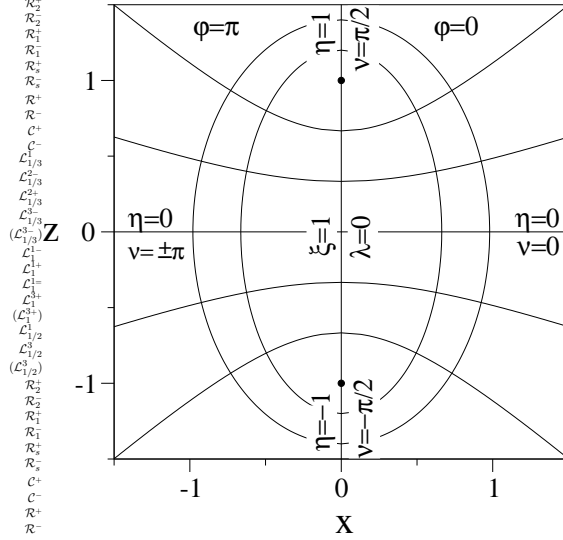


Figure 1: Coordinate lines  $\eta = \text{const}$  and  $\xi = \text{const}$  in the  $(x, z)$ -plane.

The configuration space is  $\mathbb{Q}_3 = \mathbb{R}^3 \setminus \{\mathbf{f}_1, \mathbf{f}_2\}$  where  $\mathbf{f}_{1,2} = (0, 0, \mp 1)$  are the two centers. We shall also consider planar motion in the  $(x, z)$ -plane. The configuration space is then  $\mathbb{Q}_2 = \mathbb{R}^2 \setminus \{\mathbf{f}_1, \mathbf{f}_2\}$  with  $\mathbf{f}_{1,2} = (0, \mp 1)$ . The punctuation at  $\mathbf{f}_{1,2}$  is not essential because collisions, as in Kepler's case, can be regularized [47, 11, 51].

Hamilton's equations of motion can be separated in several steps. First, the rotational symmetry with respect to the  $z$ -axis suggests to introduce cylindrical coordinates,  $(x, y, z) \mapsto (\rho, \varphi, z) \in \mathbb{R}^+ \times \mathbb{S}^1 \times \mathbb{R}$ . The Jacobian  $\partial(x, y, z)/\partial(\rho, \varphi, z)$  of this transformation has determinant  $\rho$ , hence the new coordinates are singular along the  $z$ -axis. But the angular momentum  $p_\varphi$  is a constant of the motion,  $p_\varphi = l$ , and the separated  $\varphi$ -equation reads  $\dot{\varphi} = l/\rho^2$ . For  $l \neq 0$  the centrifugal repulsion dominates the potential for small  $\rho$  preventing trajectories from reaching the  $z$ -axis. The coordinate singularity is accessible only in the case of planar motion,  $l = 0$ , which will be considered in Sec. 3.

The second step of the separation procedure, in the  $(\rho, z)$ -plane, is achieved by the introduction of elliptical coordinates:  $(\rho, z) \mapsto (\xi, \eta) \in [1, \infty) \times [-1, 1]$  with

$$\rho = \sqrt{(\xi^2 - 1)(1 - \eta^2)}, \quad z = \xi\eta, \quad (3)$$

and the inverse

$$2\xi = \sqrt{\rho^2 + (z+1)^2} + \sqrt{\rho^2 + (z-1)^2}, \quad 2\eta = \sqrt{\rho^2 + (z+1)^2} - \sqrt{\rho^2 + (z-1)^2}. \quad (4)$$

In the  $(\rho, z)$ -plane lines  $\xi = \text{const}$  are half-ellipses with foci at  $\mathbf{f}_{1,2}$ , lines  $\eta = \text{const}$  are confocal half-hyperbolas. For  $\xi = 1$  the coordinate  $\eta$  parameterizes the  $z$ -axis interval between the two centers, and for  $\eta = 1$  ( $\eta = -1$ ) the coordinate  $\xi$  parameterizes the positive (negative)  $z$ -axis for  $|z| > 1$ . The Jacobian of this transformation has determinant  $(\xi^2 - \eta^2)/\rho$ . For  $\mathbb{Q}_3$  this implies that the Jacobian  $\mathbf{J}_3$  of the combined transformation  $(x, y, z) \mapsto (\varphi, \eta, \xi)$  has determinant  $\xi^2 - \eta^2 = r_1 r_2$  which vanishes only at the foci  $(\xi, \eta) = (1, -1)$  ( $r_1 = 0$ ), and  $(\xi, \eta) = (1, 1)$  ( $r_2 = 0$ ).

In order to cover the  $(x, z)$ -plane of the configuration space  $\mathbb{Q}_2$  it requires half-ellipses  $\xi = \text{const}$  and half-hyperbolas  $\eta = \text{const}$  with  $\varphi = 0$  and  $\varphi = \pi$ , see Fig. 1. Alternatively, we set  $\xi = \cosh \lambda$ ,  $\eta = \sin \nu$  and obtain the transformation  $(x, z) \mapsto (\lambda, \nu)$ ,

$$x = \sinh \lambda \cos \nu, \quad z = \cosh \lambda \sin \nu; \quad (5)$$

it is regular except at the foci  $(\lambda, \nu) = (0, \mp \frac{\pi}{2})$ , as its Jacobian  $\mathbf{J}_2$  has again determinant  $\xi^2 - \eta^2 = \cosh^2 \lambda - \sin^2 \nu$  [39]. A single covering of  $\mathbb{Q}_2$  by the  $(\lambda, \nu)$ -coordinate strip

$\mathbb{R} \times [-\frac{\pi}{2}, \frac{\pi}{2}]$  would have discontinuities along the  $z$ -axis, for  $z^2 > 1$  (a change in sign of  $\lambda$ ). To avoid this, we take the cylinder

$$(\lambda, \nu) \in \mathbb{R} \times S^1[-\pi, \pi] \quad (6)$$

as a modified configuration space  $\bar{Q}_2$ . It is a two-sheeted cover with branch points at the foci  $(0, \pm\frac{\pi}{2})$ . The two sheets are related by point reflection at the two foci,

$$\lambda \mapsto -\lambda, \quad \nu \mapsto \pi - \nu \quad (7)$$

which leaves the Cartesian coordinates in (5) unchanged. We shall see that planar collisions can be regularized with these coordinates.

Consider now the canonical momenta. In the case of  $Q_3$ , with cylindrical coordinates  $(\rho, \varphi, z)$ , we may use the momenta  $(p_\rho, p_\varphi, p_z)$  and write down the corresponding Hamiltonian. By the separation of  $\varphi$  and the constancy of  $p_\varphi = l$ , the analysis can be restricted, for given  $l$ , to the *reduced* phase space  $T^*Q_2^l(\rho, z, p_\rho, p_z)$  with Hamiltonian <sup>1</sup>

$$H = \frac{1}{2}(p_\rho^2 + p_z^2) + V_{\text{eff}}, \quad V_{\text{eff}} = \frac{l^2}{2\rho^2} - \frac{\mu}{\sqrt{\rho^2 + (z+1)^2}} - \frac{1-\mu}{\sqrt{\rho^2 + (z-1)^2}}. \quad (8)$$

For  $l \neq 0$  it is equivalent to start with coordinates  $(\varphi, \eta, \xi)$ , introduce the canonical momenta  $(p_x, p_y, p_z) = (p_\varphi, p_\eta, p_\xi)\mathbf{J}_3^{-1}$ , and work in the reduced phase space  $T^*Q_2^l(\xi, \eta, p_\xi, p_\eta)$ . The Hamiltonian then reads

$$H = \frac{1}{\xi^2 - \eta^2}(H_\xi + H_\eta) \quad (9)$$

with

$$\begin{aligned} H_\xi &= \frac{1}{2}(\xi^2 - 1)p_\xi^2 + \frac{1}{2}\frac{l^2}{\xi^2 - 1} - \xi, \\ H_\eta &= \frac{1}{2}(1 - \eta^2)p_\eta^2 + \frac{1}{2}\frac{l^2}{1 - \eta^2} - (1 - 2\mu)\eta. \end{aligned} \quad (10)$$

Multiplying Eq. (9) by  $\xi^2 - \eta^2$  and separating terms which depend only on  $(\xi, p_\xi)$  or  $(\eta, p_\eta)$ , yields a third constant of motion besides  $H$  and  $p_\varphi$ : the separation constant

$$G = \xi^2 H - H_\xi = \eta^2 H + H_\eta = \frac{H_\eta \xi^2 + H_\xi \eta^2}{\xi^2 - \eta^2}. \quad (11)$$

A physical interpretation of the phase space function  $G$  derives from  $G = H + \Omega$  where  $\Omega$  is given by

$$\Omega = \frac{1}{2}(\mathbf{L}^2 - p_x^2 - p_y^2) + (z+1)\frac{\mu}{r_1} - (z-1)\frac{1-\mu}{r_2}. \quad (12)$$

Here  $\mathbf{L} = \mathbf{r} \times \mathbf{p}$  is the scaled angular momentum vector (about the origin). Going back to unscaled variables, it can be shown that in the limiting case  $a \rightarrow 0$  of the Kepler problem,  $\Omega$  becomes the squared angular momentum, while for  $a \rightarrow \infty$  (two Kepler problems) it is related to the Runge-Lenz vector [17].

With  $H$ ,  $p_\varphi$  and  $G$  we have three independent invariant functions on phase space. Since they appear as separation constants they must be in involution. This establishes the integrability of the problem of two fixed centers. In the following we denote the numerical values of  $H$ ,  $p_\varphi$  and  $G$ , for a given point in phase space, by  $h$ ,  $l$  and  $g$ , respectively.

<sup>1</sup>The Hamiltonian functions for the various systems of phase space coordinates will all be denoted by  $H$ . It will be clear from the context which function the symbol  $H$  refers to.

In the case of  $\bar{Q}_2$  the canonical momenta are obtained from

$$(p_x, p_z) = (p_\lambda, p_\nu) \mathbf{J}_2^{-1} \quad (13)$$

which leads to the Hamiltonian

$$H = \frac{H_\lambda + H_\nu}{\cosh^2 \lambda - \sin^2 \nu} \quad (14)$$

with

$$\begin{aligned} H_\lambda &= \frac{p_\lambda^2}{2} - \cosh \lambda, \\ H_\nu &= \frac{p_\nu^2}{2} - (1 - 2\mu) \sin \nu. \end{aligned} \quad (15)$$

The separation procedure gives the expression

$$G = H \cosh^2 \lambda - H_\lambda = H \sin^2 \nu + H_\nu = \frac{H_\nu \cosh^2 \lambda + H_\lambda \sin^2 \nu}{\cosh^2 \lambda - \sin^2 \nu} \quad (16)$$

for the second conserved quantity besides  $H$ .

Extending the involution (7) to the phase space  $T^*\bar{Q}_2$ , we get

$$\mathcal{I} : (\lambda, \nu, p_\lambda, p_\nu) \mapsto (-\lambda, \pi - \nu, -p_\lambda, -p_\nu). \quad (17)$$

$T^*Q_2$  is obtained from  $T^*\bar{Q}_2$  by factorization with respect to  $\mathcal{I}$ .

### 3 Bifurcation diagrams for planar motion $l = 0$

The Liouville-Arnold theorem [2] holds for compact invariant sets. Although we concentrate on bound motion with  $h < 0$  only, the Liouville-Arnold theorem cannot be applied to the collision orbits in the phase space  $T^*Q_2$  because they lead to infinite momenta. However, if we consider the motion in  $T^*\bar{Q}_2$  and introduce an appropriate scaling of time,  $dt \mapsto d\tau$  with

$$dt = r_1 r_2 d\tau = (\cosh^2 \lambda - \sin^2 \nu) d\tau, \quad (18)$$

together with the corresponding Hamiltonian  $\bar{H} = (H - h)dt/d\tau$ , then the level sets  $\bar{H} = 0$ , or  $H = h$ , are compact for each  $h < 0$  [47, 11]. An interesting feature of this transformation is that in the symmetric case  $\mu = 1/2$ , it turns the double cover of the planar two-center problem into the superposition of an anharmonic oscillator  $H_\lambda - h \cosh^2 \lambda = -g$  and a pendulum  $H_\nu + h \sin^2 \nu = g$ , cf. Eqs. (22) and use  $2 \sin^2 \nu = 1 - 2 \cos 2\nu$  [22].

The level sets  $H = h$  in  $T^*\bar{Q}_2$  are foliated by two-dimensional invariant manifolds  $T_{h,g}$  obtained by fixing  $H = h$  and  $G = g$ . They are pre-images of the energy momentum mapping [1],

$$\mathcal{M}_2 : T^*\bar{Q}_2 \rightarrow \mathbb{R}^2, \quad (\mathbf{q}, \mathbf{p}) \mapsto (H, G)(\mathbf{q}, \mathbf{p}) = (h, g). \quad (19)$$

Here  $\mathbf{q} = (\lambda, \nu)$  are configuration space variables, and  $\mathbf{p} = (p_\lambda, p_\nu)$  the conjugate momenta. The invariant sets  $T_{h,g} = \mathcal{M}_2^{-1}(h, g)$  are two-dimensional tori when  $(h, g)$  is a regular value of  $\mathcal{M}_2$ . When  $(h, g)$  is a critical value of the energy momentum map  $\mathcal{M}_2$  the topology of  $T_{h,g}$  can be more complicated.<sup>2</sup> The set of critical values of the energy momentum map is called the bifurcation diagram  $\Sigma^0$ ,

$$\Sigma^0 := \{(h, g) \in (-\infty, 0) \times \mathbb{R} \mid \exists (\mathbf{q}, \mathbf{p}) \in T^*\bar{Q}_2 : \mathcal{M}_2(\mathbf{q}, \mathbf{p}) = (h, g) \wedge \text{rk } D\mathcal{M}_2(\mathbf{q}, \mathbf{p}) < 2\}. \quad (20)$$

<sup>2</sup>Depending on their dynamics we will call the sets of critical points (the critical invariant sets) equilibria or periodic orbits. If the pre-image of the critical value  $(h, g)$  contains non-critical points, the critical invariant set is unstable, otherwise stable. For brevity, and if no confusion can arise, we shall use the term ‘‘periodic orbit’’ instead of ‘‘critical periodic orbit’’.

The superscript indicates that here  $l = 0$ .  $\Sigma^0$  consists of curves which separate regions of regularity, or *phases*, in the  $(h, g)$ -half-plane of negative  $h$ . Within a given phase, the corresponding invariant tori in phase space, i. e., the pre-images of the mapping  $\mathcal{M}_2$ , can be smoothly deformed into each other.

### 3.1 Types of planar motion

Even though the coordinates  $(\xi, \eta) = (\cosh \lambda, \sin \nu)$  are singular along the  $z$ -axis, they are convenient for part of the analysis. Two half strips  $[1, \infty) \times [-1, 1]$  are needed to cover  $\mathbb{Q}_2$  (one for each of the two signs of  $x$ ), and four to cover  $\mathbb{Q}_2$ . The corresponding momenta  $(p_\xi, p_\eta)$  at given  $(h, g)$  are functions of  $\xi$  and  $\eta$ , respectively,

$$\begin{aligned} p_\xi^2 &= \frac{2h\xi^2 + 2\xi - 2g}{\xi^2 - 1}, \\ p_\eta^2 &= \frac{-2h\eta^2 + 2(1 - 2\mu)\eta + 2g}{1 - \eta^2}. \end{aligned} \quad (21)$$

Phase portraits of the invariant tori, see Fig. 6, will be given in terms of the variables  $(\lambda, \nu, p_\lambda, p_\nu)$ , with  $(\lambda, \nu)$  from the cylinder (6), and momenta

$$\begin{aligned} p_\lambda^2 &= 2h \cosh^2 \lambda + 2 \cosh \lambda - 2g, \\ p_\nu^2 &= -2h \sin^2 \nu + 2(1 - 2\mu) \sin \nu + 2g. \end{aligned} \quad (22)$$

Classically allowed motion requires the squared momenta to be positive. We discuss this in terms of the zeros of the polynomials

$$P_\mu^0(s) = 2(s^2 - 1)(hs^2 - (1 - 2\mu)s - g) \quad (23)$$

with  $s = \xi$  or  $s = \eta$  and the understanding that formally  $\mu = 1$  if  $s = \xi$ .  $P_\mu^0(s)$  is related to the momenta via  $(\xi^2 - 1)p_\xi = \pm \sqrt{P_1^0(\xi)}$  and  $(1 - \eta^2)p_\eta = \pm \sqrt{P_\mu^0(\eta)}$ . The roots of  $P_1^0(\xi)$  and  $P_\mu^0(\eta)$  are

$$\xi_{1,2} = \pm 1, \quad \xi_{3,4} = \pm \sqrt{\frac{g}{h} + \frac{1}{4h^2} - \frac{1}{2h}}, \quad (24)$$

$$\eta_{1,2} = \pm 1, \quad \eta_{3,4} = \pm \sqrt{\frac{g}{h} + \frac{(1 - 2\mu)^2}{4h^2} + \frac{1 - 2\mu}{2h}}, \quad (25)$$

respectively. In both variables, the polynomials have two fixed roots  $\pm 1$  and two moveable roots,  $\xi_{3,4}$  or  $\eta_{3,4}$ , which depend on the constants of motion. Double roots appear when the discriminant

$$\text{discr}(P_\mu^0(s), s) = 256(h + 1 - 2\mu - g)^2(h - 1 + 2\mu - g)^2((1 - 2\mu)^2 + 4hg) \quad (26)$$

vanishes. For each  $\mu \neq 1/2$  this gives three curves in the lower half  $(g, h)$ -plane. They are

$$\mathcal{L}_\mu^1 := \{g = h - 1 + 2\mu\}, \quad \mathcal{L}_\mu^2 := \{g = h + 1 - 2\mu\}, \quad \mathcal{L}_\mu^3 := \{4gh = -(1 - 2\mu)^2\}. \quad (27)$$

For  $\mu = 1/2$  the lines  $\mathcal{L}_\mu^1 = \mathcal{L}_\mu^2 = \{g = h\}$  coincide, and  $\mathcal{L}_\mu^3 = \{g = 0\}$ . Fig. 2a shows these curves for  $\mu = 1/3$ . Line  $\mathcal{L}_\mu^3$  has a tangency with  $\mathcal{L}_\mu^2$  if  $\mu < 1/2$ , and with  $\mathcal{L}_\mu^1$  if  $\mu > 1/2$ . The point of tangency is  $(g, h) = (|\frac{1}{2} - \mu|, -|\frac{1}{2} - \mu|)$ . It will be convenient to introduce the notation  $\mathcal{L}_\mu^{k+}$  and  $\mathcal{L}_\mu^{k-}$  for the parts of  $\mathcal{L}_\mu^k$  above and below this point, respectively. Together these lines divide the lower half  $(g, h)$ -plane into five regions with characteristic arrangements of roots; we label them by Latin numbers I through V. The polynomial



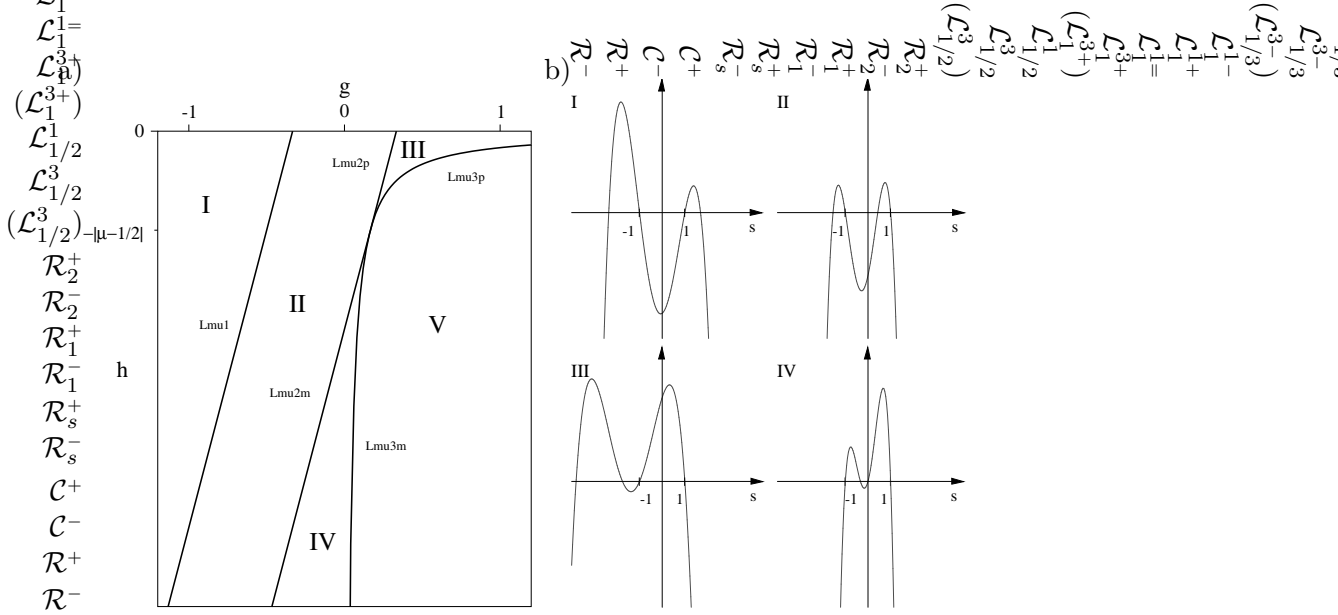


Figure 2: (a) Lines of vanishing discriminant of  $P_\mu^0(s)$  in the lower half  $(g, h)$ -plane for  $\mu = 1/3$ ; (b) representative polynomials  $P_\mu^0(s)$  for regions I to IV.

$P_{1/3}^0(\eta)$  is sketched for the cases I-IV in Fig. 2b. In region I the polynomial is negative for all physical values of  $\eta \in [-1, 1]$ , hence no motion is possible. Upon entering region II across  $\mathcal{L}_\mu^1$ ,  $\eta_3$  moves below 1, and oscillatory motion in the  $\eta$ -range  $[\eta_3, 1]$  becomes possible; this means motion in the neighborhood of the stronger center  $\mathbf{f}_2$ . The next transition is either to III or to IV, depending on  $h$ . At  $\mathcal{L}_\mu^{2+}$  the zero  $\eta_3$  decreases below  $-1$  which opens the way for rotational motion in the variable  $\eta$ : motion around both centers. At  $\mathcal{L}_\mu^{2-}$ , on the other hand,  $\eta_4$  increases above  $-1$  so that two disjoint intervals  $[\eta_3, 1]$  and  $[-1, \eta_4]$  of oscillatory  $\eta$ -motion exist, one about each center. The transition to region V involves a collision of  $\eta_3$  and  $\eta_4$ ; the only real roots in region V are  $\pm 1$ . This is the same situation as in region III. In fact, the distinction between III and V involves roots in the non-physical range. Consequently, it does not correspond to a physical transition.

The bifurcation scheme associated with  $P_1^0(\xi)$  is similar. The differences are that now  $\mathcal{L}_1^1$  lies to the right of  $\mathcal{L}_1^2$ , and that the physical  $\xi$ -range is  $[1, \infty)$ . As a result, the non-physical regions are now IV and V.

To get the complete bifurcation diagram  $\Sigma^0$  of bounded motion, we must superimpose the critical lines of  $\eta$ - and  $\xi$ -motion, and the enclosed regions must be physically meaningful. This leads to Fig. 3a for  $\mu = 1/3$  and to Fig. 3b for the symmetric case  $\mu = 1/2$ . For the part of  $\mathcal{L}_1^1$  which lies below the intersection with  $\mathcal{L}_\mu^3$  we introduce the notation  $\mathcal{L}_1^{1=}$ , and we anticipate the identification given in Table I of line segments with icons representing the corresponding critical orbits. The left boundary of the physically meaningful  $(g, h)$ -region is defined by  $\mathcal{L}_\mu^1 = \dot{\cdot}$ , the right boundary by  $\mathcal{L}_1^{1=} = \dot{\cdot}$  and  $\dot{\cdot}$ ,  $\mathcal{L}_1^{1-} = \dot{\cdot}$ , and  $\mathcal{L}_1^{3+} = \odot$  and  $\odot$ . The region so defined is partitioned into four phases by the inner critical lines  $\mathcal{L}_\mu^2 = \dot{\cdot}$ ,  $\mathcal{L}_\mu^3 = \dot{\cdot}$  and  $\mathcal{L}_1^{1+} = \dot{\cdot}$ . In the symmetric case  $\mu = 1/2$  there are only three phases due to the identity of  $\mathcal{L}_\mu^1$  and  $\mathcal{L}_\mu^2$ . As indicated in the figures, they are denoted by  $\mathbf{t}_s$ ,  $\mathbf{t}_1$ ,  $\mathbf{t}_p$  and, in the asymmetric case,  $\mathbf{t}_s$ . This notation goes back to Charlier [13] and Pauli [43]. Representative trajectories in configuration space, and the corresponding caustics, are shown in Fig. 4.

The tori of phase  $\mathbf{t}_s$  are ‘‘satellite’’ motion around the stronger center at  $\mathbf{f}_2$ . The order of zeros is  $\eta_4 < -1 < \eta_3 < 1$  ( $\eta$ -region II) and  $-1 < \xi_4 < 1 < \xi_3$  ( $\xi$ -region II). The caustic is formed by arcs of the ellipse  $\xi = \xi_3$  and the hyperbola  $\eta = \eta_3$ . In the symmetric

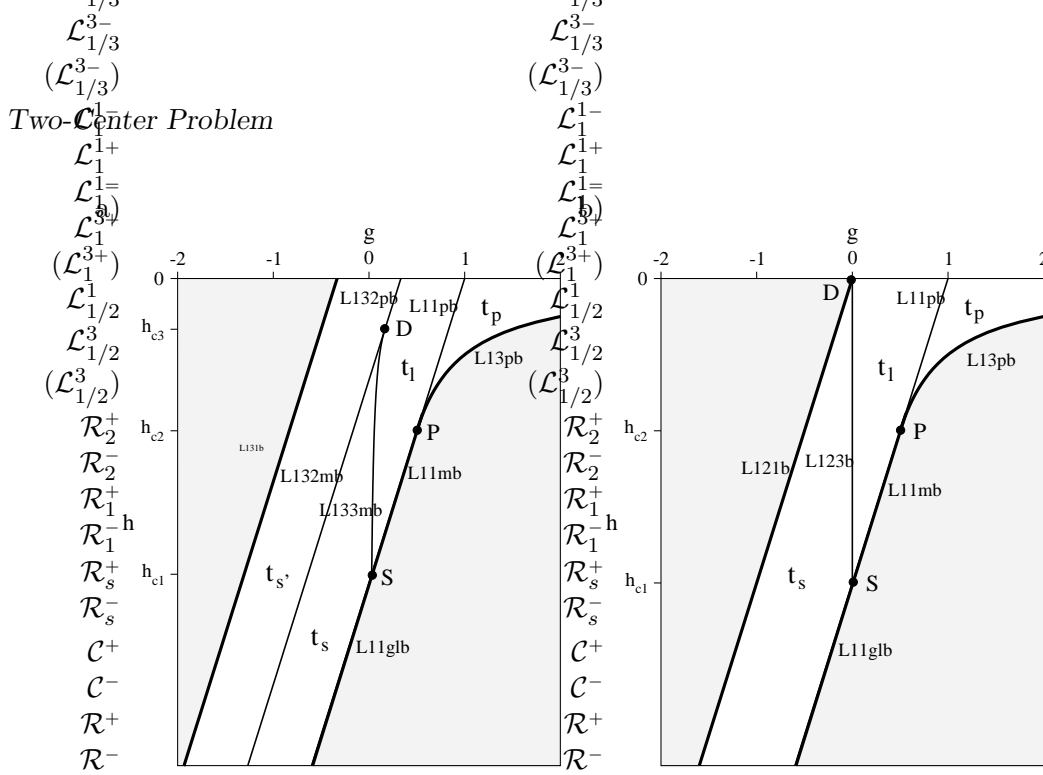


Figure 3: Bifurcation diagrams  $\Sigma^0$  for the planar two-center problem; (a) asymmetric case with  $\mu = 1/3$ , (b) symmetric case  $\mu = 1/2$ .

two-center problem this phase does not exist because then  $\eta_3 = -\eta_4$ .

Phase  $\mathbf{t}_s$  has two disjoint pre-images in phase space, representing “satellite” motion around either center. The  $\xi$ -zeros are ordered as in phase  $\mathbf{t}_{s'}$ , but the  $\eta$ -zeros are as in region IV:  $-1 < \eta_4 < \eta_3 < 1$ . Motion around the center at  $\mathbf{f}_1$  is the same type as in  $\mathbf{t}_{s'}$ ; its caustic is formed by arcs of the ellipse  $\xi = \xi_3$  and the hyperbola  $\eta = \eta_4$ . In the symmetric case the two caustics are mirror images of each other.

Phase  $\mathbf{t}_1$  has been called “lemniscate” motion. Trajectories fill the interior of the ellipse  $\xi = \xi_3$  as there is no restriction to  $\eta$  in the range  $[-1, 1]$ . The arrangement of  $\eta$ -zeros is that of regions III or V. The  $\xi$ -zeros are still in the order of region II. The pre-image of phase  $\mathbf{t}_1$  in phase space has only one connected component.

Phase  $\mathbf{t}_p$  is referred to as “planetary” motion; the trajectories are confined to the region between the two ellipses  $\xi = \xi_4$  and  $\xi = \xi_3$ . The difference to phase  $\mathbf{t}_1$  is the arrangement of  $\xi$ -zeros:  $1 < \xi_4 < \xi_3$ . There is no restriction in  $\eta$ . Corresponding to the two senses of rotation there are two disjoint pre-images of phase  $\mathbf{t}_p$  in phase space.

### 3.2 Foliations of energy surfaces

Let us now discuss the topological structure and bifurcation schemes of energy surfaces

$$\bar{\mathcal{E}}_h^0 := \{(\mathbf{q}, \mathbf{p}) \in T^*\bar{Q}_2 \mid H(\mathbf{q}, \mathbf{p}) = h\} \quad \text{and} \quad \mathcal{E}_h^0 := \bar{\mathcal{E}}_h^0 / \mathcal{I} \subset T^*Q_2, \quad (28)$$

where  $\mathcal{I}$  is the involution defined in (17). The “physical” energy surfaces  $\mathcal{E}_h^0$  contain lines of singularities which correspond to collisions. These lines are given by  $(\lambda, \nu) = (0, \pm \frac{\pi}{2})$  and  $(p_\lambda, p_\nu)$  as functions of  $(h, g)$ :

$$\frac{p_\lambda^2}{2} = h - g + 1, \quad \frac{p_\nu^2}{2} = -h + g \pm (1 - 2\mu). \quad (29)$$

Without the identification by  $\mathcal{I}$ , the manifolds  $\bar{\mathcal{E}}_h^0 \subset T^*\bar{Q}_2$  are smooth for almost every  $h$ . The exceptional or critical energies  $h$  correspond to the energies of equilibrium points, where  $\bar{\mathcal{E}}_h^0 \subset T^*\bar{Q}_2$  changes its topology. The topology of  $\bar{\mathcal{E}}_h^0$  may be inferred from the nature of the accessible region in configuration space  $\bar{Q}_2$  [9]. The nature of this region

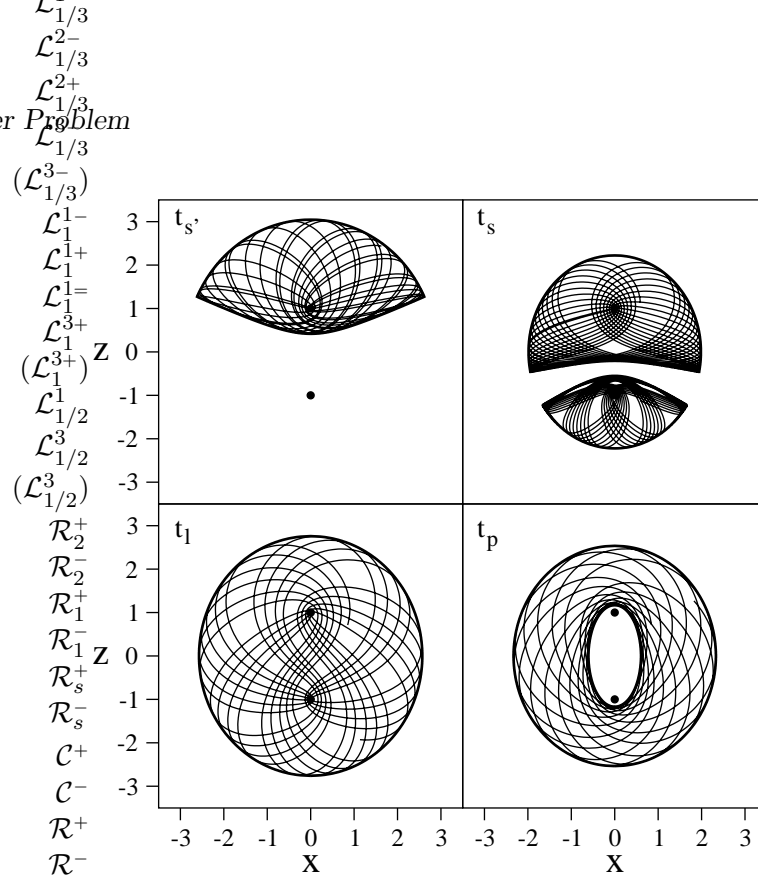


Figure 4: The four types of orbits, and their caustics, for planar motion with  $\mu = 1/3$ . The constants of motion are  $(h, g) = (-0.35, -0.20)$  for  $t_s'$ ,  $(-0.44, 0.05)$  for  $t_s$ ,  $(-0.31, 0.40)$  for  $t_1$  and  $(-0.27, 0.80)$  for  $t_p$ .

changes at the energy of the saddle point of the potential in the Hamiltonian (2) which lies on the  $z$ -axis at

$$z = -\frac{1 - 2\sqrt{\mu(1-\mu)}}{1 - 2\mu}. \quad (30)$$

The corresponding energy is

$$h_{c1} = -\sqrt{\mu(1-\mu)} - \frac{1}{2}. \quad (31)$$

For  $h$  below  $h_{c1}$ , the accessible region in  $\bar{Q}_2$  consists of two disks. For  $h$  above  $h_{c1}$  it consists of an annulus. Accordingly, the energy surface is the disjoint union of two 3-spheres  $S^3$  as long as motion is confined to the neighborhoods of the two centers, whereas it has the topology of  $S^1 \times S^2$  for energies above the saddle point energy.

We are interested in how the energy surfaces  $\bar{\mathcal{E}}_h^0$  are foliated by the invariant sets  $T_{h,g}$  which are tori for almost every possible  $g$ . The intersections  $h = \text{const}$  of bifurcation lines in Fig. 3a suggest that there is only one foliation of  $\bar{\mathcal{E}}_h^0$  for  $h < h_{c1}$  and three different foliations for  $h > h_{c1}$ . The critical energy values where the foliation changes are

$$h_{c2} = -\frac{1}{2}, \quad h_{c3} = \mu - \frac{1}{2}. \quad (32)$$

In the symmetric case, we have  $h_{c1} = -1$ ,  $h_{c2} = -1/2$ ,  $h_{c3} = 0$ .

To represent the foliations in  $\mathcal{E}_h^0$ , we use Fomenko graphs [28] as shown in Figures 5a, b, for representative energy values  $h_1 < h_{c1} < h_2 < h_{c2} < h_3 < h_{c3} < h_4 < 0$ . The horizontal coordinate of the graphs increases with  $g$ , the vertical direction has only symbolic meaning. The graphs consist of several branches which may or may not be connected at vertices. Each branch represents a family of 2-tori that can be smoothly deformed into each other. Except for endpoints and vertices, every point of the graph represents exactly one regular physical torus. (Note that after lifting the identification with  $\mathcal{I}$ , the graphs ought to be doubled to the right of  $g = -(1 - 2\mu)^2/4h$  for  $h_{c1} < h < h_{c3}$ , and to the right of  $g =$

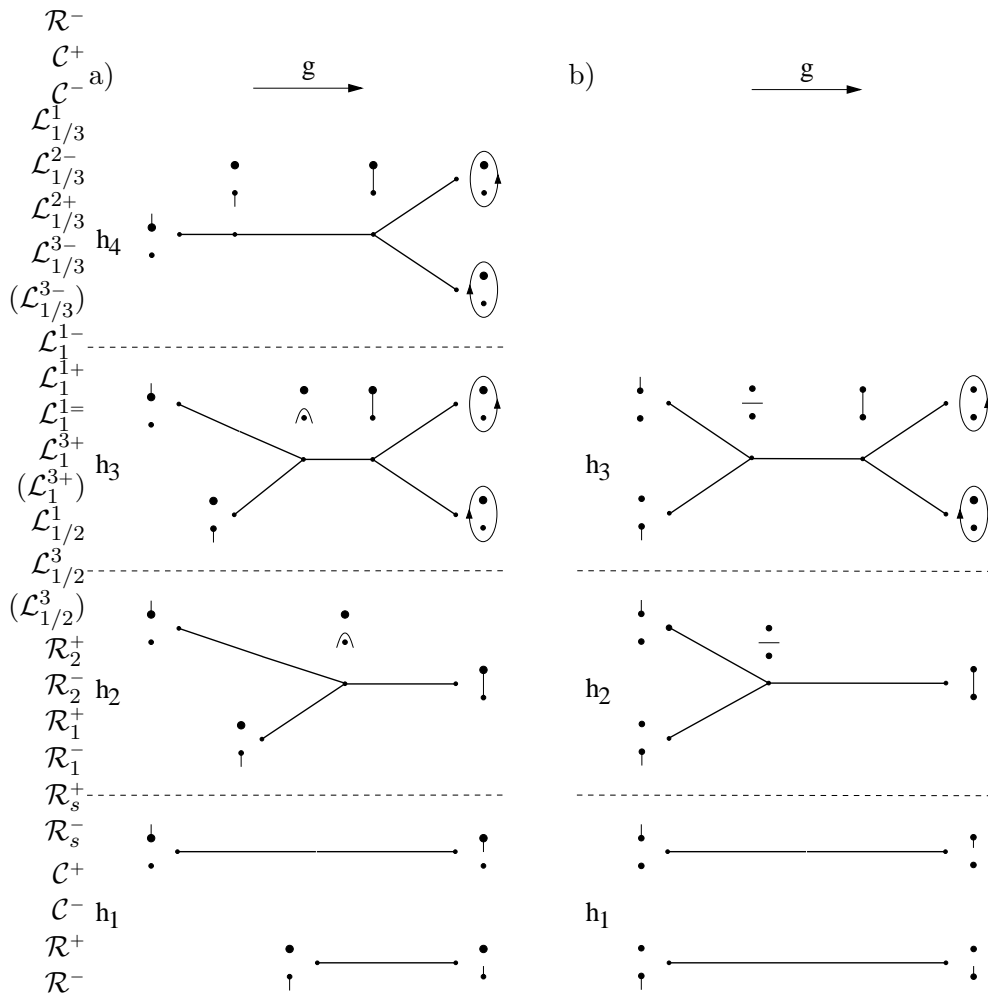


Figure 5: Fomenko graphs for energy surfaces  $\mathcal{E}_h^0$  in the asymmetric (a) and symmetric (b) planar two-center problem. Each inner point of a branch represents a regular physical torus. The periodic orbits associated with endpoints and vertices are illustrated by sketches of their projections to configuration space. In the corresponding Fomenko graphs for  $\bar{\mathcal{E}}_h^0$ , the part to the right of the leftmost unstable periodic orbit is doubled.

$h+1-2\mu$  for  $h > h_{c3}$ .) The endpoints are stable periodic orbits, the vertices correspond to unstable periodic orbits plus the attached separatrices. Note that the endpoints correspond to Lyapunov stable periodic orbits when the constant  $G$  has a local maximum or minimum there, which is generically the case. We see that for given  $h$  and  $g$  there are at most two regular tori. For low energies like  $h_1$ , the graphs are just two disconnected branches; above  $h_{c1}$  they are connected and possess one or two vertices (one or three in the corresponding graphs for  $\bar{\mathcal{E}}_h^0$ ).

Comparison of Figures 3 and 5 reveals the non-trivial relationship between phases in  $(h, g)$ -space and families of tori in phase space. For example, the family of satellite orbits about the strong center  $\mathbf{f}_2$  represents the upper branch of the Fomenko graph for  $h = h_1$ . It is unaffected by the transition from  $\mathbf{t}_s$  to  $\mathbf{t}_s$ , i.e., the family exists in both phases. However, in phase  $\mathbf{t}_1$  there is a one-to-one correspondence of points  $(h, g)$  and tori in  $\mathcal{E}_h^0$ .

### 3.3 Phase Portraits

Fig. 5 contains little sketches of the periodic orbits in configuration space (the  $z$ -axis pointing upward). To obtain this and more information about possible types of motion at given energy, consider the phase portraits of Fig. 6. They show the relations  $\lambda$  vs.  $p\lambda$  and  $\nu$  vs.  $p\nu$  as given by Eq. (22), for the energy values  $h_1, \dots, h_4$ , and, for each  $h$ , with

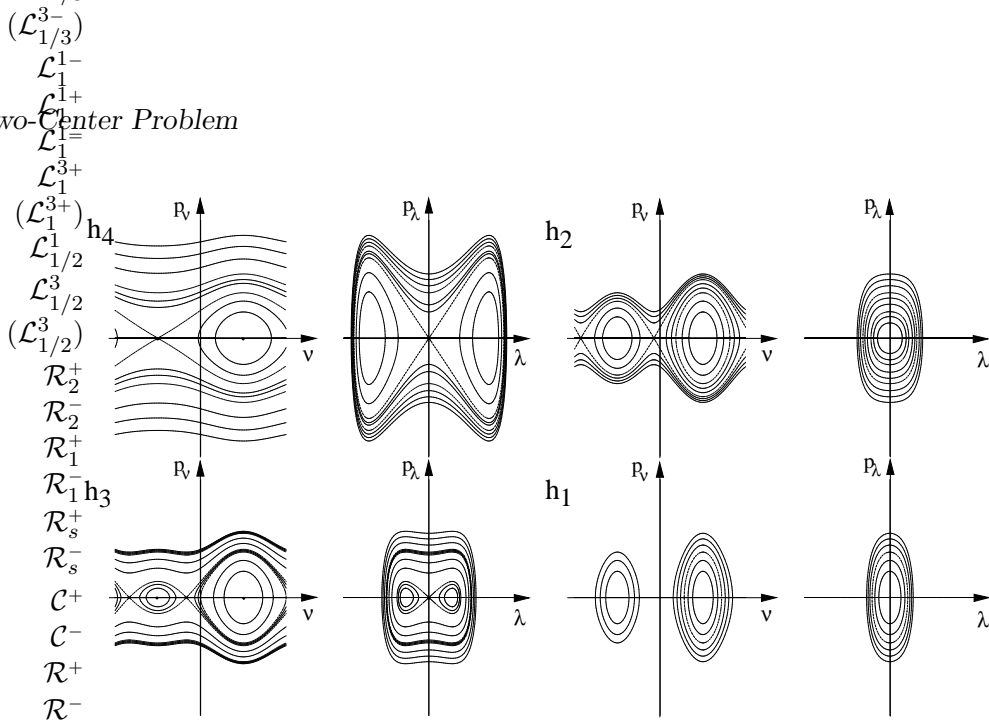


Figure 6: Phase portraits of the asymmetric planar two-center problem. The energy values are  $h_1 = -1.47$ ,  $h_2 = -0.74$ ,  $h_3 = -0.33$  and  $h_4 = -0.08$ . The coordinate ranges are  $\nu \in [-\pi, \pi]$ ,  $p_\nu \in [-3, 3]$ ,  $\lambda \in [-3.5, 3.5]$ ,  $p_\lambda \in [-3, 3]$ .

different values of  $g$ . These phase portraits hold for  $T^*\bar{Q}_2$  because  $\nu$  extends along the circle  $S^1 = [-\pi, \pi]$ . In  $T^*Q_2$  the  $(\nu, p_\nu)$ -cylinder is reduced to the strip  $[-\frac{\pi}{2}, \frac{\pi}{2}] \times \mathbb{R}$ , and points at its boundaries with opposite signs of  $p_\nu$  are identified according to (17). This connects the *two* rotational branches of  $\nu$ -motion (for  $h > h_{c1}$ ) into *one* oscillation. The period of this oscillation is the same as that of the two former rotations. The periods of the former oscillatory orbits, on the other hand, are reduced by one half. We shall discuss orbits in  $T^*\bar{Q}_2$  or  $T^*Q_2$ , whatever is more convenient in the context.

The  $(\lambda, p_\lambda)$ -plane and the  $(\nu, p_\nu)$ -cylinder are foliated by topological circles  $S^1_{h,g}(\lambda, p_\lambda)$  and  $S^1_{h,g}(\nu, p_\nu)$ , respectively. Together, the product of two such circles forms a torus  $T^2_{h,g} \subset \bar{\mathcal{E}}_h^0$ . With increasing  $g$ , the circles  $S^1_{h,g}(\lambda, p_\lambda)$  shrink, while the circles  $S^1_{h,g}(\nu, p_\nu)$  grow. At the smallest possible  $g$ , for the two families of tori in phases  $\mathbf{t}_s$  and  $\mathbf{t}_s$ , the  $\nu$ -motion is frozen at  $+\frac{\pi}{2}$  or  $-\frac{\pi}{2}$ , corresponding to collision orbits along the  $z$ -axis,  $\dot{\circ}$  above  $\mathbf{f}_2$ , or  $\dot{\circ}$  below  $\mathbf{f}_1$ , respectively. At the highest possible  $g$ , the  $\lambda$ -motion is frozen: at  $\lambda = 0$  for  $h < h_{c2}$ , and at  $\cosh \lambda = -1/2h$  for  $h > h_{c2}$ ; combining this with the corresponding circles  $S^1_{h,g}(\nu, p_\nu)$ , we see that for  $h < h_{c1}$  the motion consists of collision orbits  $\dot{\circ}$  and  $\dot{\circ}$  between the two centers; in the range  $h_{c1} < h < h_{c2}$  these two orbits have joined across the potential barrier to form the double collision orbit  $\dot{\circ}$ , and for  $h > h_{c2}$  the orbits with maximum  $g$  at given  $h$  are the two ellipses  $\left(\dot{\circ}\right)$  and  $\left(\dot{\circ}\right)$  with  $\lambda = \text{const}$ , differing in the sense of rotation.

The bifurcation at  $h_{c1}$  is a bifurcation of the energy surface  $\bar{\mathcal{E}}_h^0$ . Comparison of the two portraits for  $h_1$  and  $h_2$  in Fig. 6 shows that the bifurcation takes place in the  $(\nu, p_\nu)$ -circles. Their merging gives rise to a transition (at maximum  $g$ ) from the two disconnected orbits  $\dot{\circ}$  and  $\dot{\circ}$  to a stable orbit of type  $\dot{\circ}$  plus an unstable isolated orbit  $\dot{\circ}$  with a fixed negative value of  $\nu$ : oscillation along a piece of the corresponding hyperbola.

The bifurcations at  $h_{c2}$  and  $h_{c3}$  are not associated with topological changes of the energy surface. Instead, they are bifurcations of periodic orbits. At  $h = h_{c2}$  the elliptic center  $(0, 0)$  in the  $(\lambda, p_\lambda)$ -plane undergoes a pitchfork bifurcation: the oscillation  $\dot{\circ}$  becomes unstable and ejects two stable rotations  $\left(\dot{\circ}\right)$  and  $\left(\dot{\circ}\right)$ . At  $h = h_{c3}$  there is a bifurcation

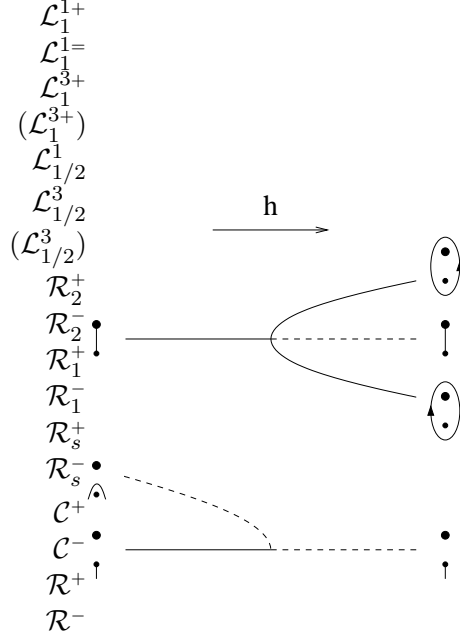


Figure 7: Top: Pitchfork bifurcation at  $h_{c2}$ : the oscillatory center-to-center orbit gives birth to two planetary orbits, with different sense of rotation, on the same ellipse. Bottom: Inverse period doubling bifurcation at  $h_{c3}$  of the collision orbit below  $\mathbf{f}_1$ . Solid (dashed) lines mark stable (unstable) periodic orbits.

at  $(-\frac{\pi}{2}, 0)$  in the  $(\nu, p_\nu)$ -plane. It has different interpretations in  $\mathbb{T}^*\mathbb{Q}_2$  and  $\mathbb{T}^*\bar{\mathbb{Q}}_2$ . In the physical phase space  $\mathbb{T}^*\mathbb{Q}_2$  it is an inverse period doubling: the oscillation  $\dot{\cdot}$  below  $\mathbf{f}_1$  loses its stability after merging with the unstable oscillation  $\hat{\wedge}$  of twice its period. In the smooth space  $\mathbb{T}^*\bar{\mathbb{Q}}_2$  we have an inverse pitchfork bifurcation where all orbits have the same period. (In the symmetric case this transition does not occur because then  $h_{c3} = 0$ .) The two scenarios are sketched for  $\mathbb{T}^*\mathbb{Q}_2$  in Fig. 7.

Except for type  $\mathbf{t}_p$ , every torus  $\mathbb{T}_{h,g}$  has points  $(\lambda, \nu) = (0, \pm\pi/2)$  corresponding to collision with the centers. The corresponding  $(p_\lambda, p_\nu)$  are given by Equations (22). These points exhibit no particular criticality in the phase space  $\mathbb{T}^*\mathbb{Q}_2$ . In  $\mathbb{T}^*\mathbb{Q}_2$ , on the other hand, they correspond to infinities of the momenta.

The phase portraits for the symmetric case  $\mu = 1/2$  differ from those in Fig. 6 in that the  $(\nu, p_\nu)$  pictures are symmetric with respect to the axis  $\nu = 0$ .

Table I collects the information obtained so far on periodic orbits. The first column identifies the orbits by their icons. The second specifies the fixed coordinate  $\nu$  or  $\lambda$ ; correspondingly,  $p_\nu$  or  $p_\lambda$  are zero. The third column gives the associated line in the bifurcation diagram. The last four columns show in which of the four energy ranges the orbit exists and whether it is stable (s) or unstable (u). The arrows indicate bifurcations already described. Notice there is a one-to-one correspondence of icons and lines, but the same icon may represent stable or unstable periodic orbits. This is distinguished by the sign in the upper index:  $\dot{\cdot}$  is stable along  $\mathcal{L}_\mu^{2-}$ , unstable along  $\mathcal{L}_\mu^{2+}$ ; similarly,  $\hat{\wedge}$  is stable along  $\mathcal{L}_1^{1-}$  and unstable along  $\mathcal{L}_1^{1+}$ . A detailed stability analysis is given next.

### 3.4 Stability of Periodic Orbits

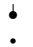


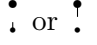
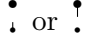

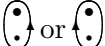
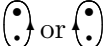
Regularizing the motion in  $\mathbb{T}^*\bar{\mathbb{Q}}_2$  by using the time  $\tau$  defined in (18), we obtain the following equations of motion ( $'$  means differentiation with respect to  $\tau$ ):

$$\begin{aligned} \lambda' &= p_\lambda & p_\lambda' &= (1 + 2h \cosh \lambda) \sinh \lambda \\ \nu' &= p_\nu & p_\nu' &= (1 - 2\mu - 2h \sin \nu) \cos \nu \end{aligned} \quad (33)$$

To discuss the stability of the eight isolated periodic orbits listed in Table I, we analyze the variational equations for  $(\delta\mathbf{q}(\tau), \delta\mathbf{p}(\tau))^t = \mathbf{S}(\tau)(\delta\mathbf{q}(0), \delta\mathbf{p}(0))^t$  in their neighborhood:

$$\mathbf{S}' = \mathbf{J} \mathbf{D}^2 H \mathbf{S}, \quad (34)$$

Table I: Critical periodic orbits: icons, definition, and stability properties.

orbit	fix coordinate	$(h, g)$ -line	$(-\infty, h_{c1})$	$(h_{c1}, h_{c2})$	$(h_{c2}, h_{c3})$	$(h_{c3}, 0)$
	$\nu = \frac{\pi}{2}$	$\mathcal{L}_\mu^1$	s	s	s	s
	$\nu = -\frac{\pi}{2}$	$\mathcal{L}_\mu^2$	s	s	s $\rightarrow$	u
	$\sin \nu = \frac{1-2\mu}{2h}$	$\mathcal{L}_\mu^{3-}$	-	u	u $\nearrow$	-
 or 	$\lambda = 0$	$\mathcal{L}_1^{1=}$	s $\nearrow$ s $\searrow$	-	-	-
	$\lambda = 0$	$\mathcal{L}_1^1$	-	s	$\rightarrow$ u	u
 or 	$\cosh \lambda = -\frac{1}{2h}$	$\mathcal{L}_1^{3+}$	-	-	$\searrow$ s	s

where  $\mathbf{J}$  is the symplectic matrix and  $D^2H$  the Hessian of the Hamiltonian with respect to  $(\mathbf{q}, \mathbf{p})$ . Integrating over a period  $T = \oint d\tau$  of the physical motion (as opposed to the regularized motion), with  $\mathbf{S}(0) = \mathbf{1}$ , we obtain the monodromy matrix  $\mathbf{S}(T)$ . Two of its eigenvalues are 1, corresponding to perturbations along the periodic orbits and perpendicular to the energy shell in  $T^*Q_2$ . The other two eigenvalues  $\sigma_{1,2}$  are related by  $\sigma_1\sigma_2 = 1$ . Using Greene's residue [30]

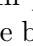
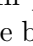
$$R := \frac{4 - \text{tr } \mathbf{S}}{4} \quad (35)$$

they can be expressed as



$$\sigma_{1,2} = 1 - 2R \pm 2\sqrt{R(R-1)} = \cos 2\pi W \pm i \sin 2\pi W, \quad (36)$$

where the latter equation is meaningful in the case  $0 < R < 1$  of elliptic periodic orbits, where it gives the rotation number  $W$ .

Fig. 8 presents the results of numerical integration of Eq. (34), where due care has been taken of the differences of periods in  $T^*\bar{Q}_2$  and  $T^*Q_2$ .

In principle the residue  $R$  may be calculated in terms of elliptic integrals. We shall come back to this in Sec. 5, but let us indicate for the example of orbits  and  how this is done. For orbits of elliptic stability the rotation number is the ratio of periods of the  $\nu$ - and the  $\lambda$ -motion,  $W = T_\nu/T_\lambda$ . The period  $T_\lambda = 2\pi/\omega_\lambda$  is obtained by linearizing the first equation in (33) about  $\lambda = 0$ :  $\lambda'' = (1 + 2h)\lambda =: -\omega_\lambda^2 \lambda$ . Determination of  $T_\nu$  may proceed from (14) with  $\lambda = 0$ ,  $H_\lambda = -1$ , and  $p_\nu = \nu'$ . Substituting  $\sin \nu = \eta$ , we get the complete elliptic integral of the first kind

$$T_\nu = \oint d\tau = \oint \frac{d\eta}{\sqrt{P_\mu^0(\eta)}}, \quad (37)$$

where the polynomial  $P_\mu^0(\eta)$  is given in (23). The orbit  lives in the  $\eta$ -range  $-1 < \eta < \eta_4$ , and  in  $\eta_3 < \eta < 1$ . But the complete integrals (37) are the same for both orbits because

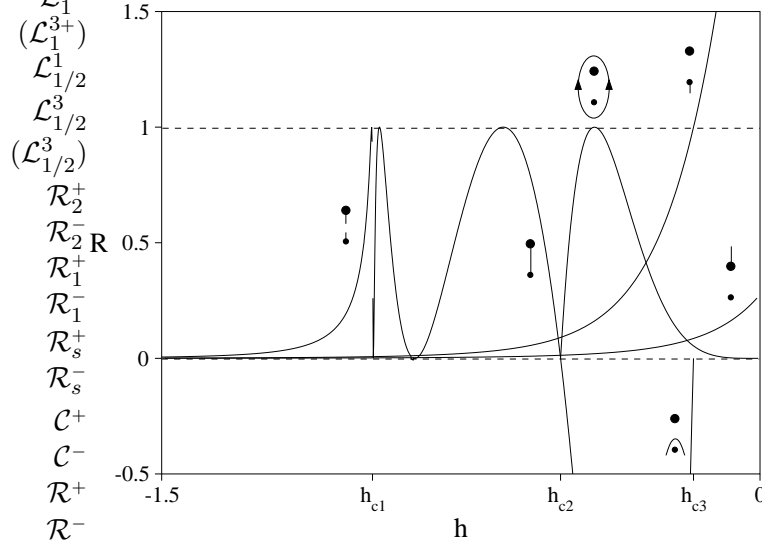


Figure 8: Greene’s residue  $R$  of the isolated periodic orbits of the planar asymmetric two-center problem.

the two corresponding closed paths on the elliptic curve  $w^2 = P_\mu^0(\eta)$  are homologous. Hence, both orbits have the same rotation number  $W$ . With  $h$  approaching  $h_{c1}$  from below,  $T_\nu$  diverges logarithmically whereas  $T_\lambda$  has only a mild  $h$ -dependence, hence  $W$  diverges to  $\infty$ . Using  $2R = 1 - \cos 2\pi W$  we see that the residue performs infinitely many oscillations as  $h \rightarrow h_{c1}$ . This is a typical behavior in the neighborhood of unstable equilibria. Only the beginning of these oscillations is visible in Fig. 8. Their “mirror image” on the side  $h > h_{c1}$  appears in the residue  $R(h)$  of the orbit  $\dot{\downarrow}$  which is stable for  $h < h_{c2}$ , then turns unstable in a pitchfork bifurcation and gives birth to the two stable orbits  $\dot{\circ}$  and  $\dot{\circ}$ .

The orbit  $\dot{\downarrow}$  is stable for any negative energy  $h$ ; as  $h$  increases from  $-\infty$  to 0,  $R$  increases monotonously from 0. The residue of the orbit  $\dot{\downarrow}$  is everywhere larger and reaches the value 1 at  $h = h_{c3}$ ; this corresponds to  $W = 1/2$  and period doubling. The orbit with twice the period of  $\dot{\downarrow}$ , at  $h_{c3}$ , is  $\dot{\wedge}$ . It is hyperbolic in the entire range  $h_{c1} < h < h_{c3}$  of its existence, as  $R$  is everywhere negative, approaching 0 as  $h$  grows towards  $h_{c3}$ .

## 4 Bifurcation diagrams for motion with general $l$

The aim of this section is to present the bifurcation diagram  $\Sigma$  of the energy-momentum mapping

$$\mathcal{M}_3 : \mathbb{T}^*Q_3 \rightarrow \bar{\Sigma} := \mathcal{M}_3(\mathbb{R}^6) \subset \mathbb{R}^3, \quad (\mathbf{q}, \mathbf{p}) \mapsto (H, G, p_\varphi)(\mathbf{q}, \mathbf{p}) = (h, g, l), \quad (38)$$

for bound motion,  $h < 0$ . Here  $\bar{\Sigma}$  denotes the image of the energy momentum map; the bifurcation diagram  $\Sigma$  is the subset of all those values  $(h, g, l)$  in the image which possess pre-images where  $r := \text{rk } D\mathcal{M}_3$  is smaller than 3 for some point in the pre-image. The complement of  $\Sigma$  in  $\bar{\Sigma}$  is the set of regular values  $(h, g, l)$  where  $r = 3$  for every point in the pre-image.  $\Sigma$  has a natural stratification into components of 2, 1, and 0 dimensions. The *regular part*<sup>3</sup> of the critical set  $\Sigma$  is the two-dimensional set of values  $(h, g, l)$  which have pre-images where the minimal rank is  $r = 2$ . The *singular part* of  $\Sigma$  is the one-dimensional

<sup>3</sup>The regular part of the critical set  $\Sigma$  is not to be mistaken with the set of regular values  $\bar{\Sigma} \setminus \Sigma$ , which have full rank. Likewise, the adjective “singular” is used in different connotations; it may refer to



set of  $(h, g, l)$  which have pre-images where the minimal rank is  $r = 1$ . Finally the *super-singular part* of  $\Sigma$  is the discrete set of values with pre-images where the minimal rank is  $r = 0$ .

In general the topology of the singular fibers  $T_{h,g,l} = \mathcal{M}_3^{-1}(h, g, l)$  of critical values  $(h, g, l)$  can be quite complicated. In the simplest case the dimension of the set of critical values equals the rank and the dimension of the corresponding invariant set of critical points in the pre-image. Under certain additional assumptions this set of critical points is a torus. In many examples of systems with three degrees of freedom, the regular points in  $\bar{\Sigma} \setminus \Sigma$  have 3-tori in their pre-image, the regular parts of  $\Sigma$  have 2-tori in their pre-image, the singular parts of  $\Sigma$  have 1-tori (or periodic orbits) in their pre-image, and, finally, equilibrium points are in the pre-image of super-singular points of  $\Sigma$ . Note that the pre-image of a critical value often contains non-critical points, hence it can be larger than the invariant torus composed of critical points just mentioned. Typically these additional points in the pre-image belong to the stable and/or unstable manifolds (“separatrices”) of the critical invariant torus. The dimension of the invariant manifolds increases when the dimension of the critical set decreases. If a connected component of the fiber  $T_{h,g,l}$  contains critical and non-critical points (which in our case always belong to separatrices) we will say that the critical torus contained in it is unstable, otherwise stable.

Based on the following analysis we can be more precise. In the two-center problem pre-images of regular parts of  $\Sigma$  are either stable 2-tori or unstable 2-tori with their stable and unstable manifolds. All these 2-tori are *relative periodic orbits* (RPOs), i. e., they are 2-tori obtained from periodic orbits of the reduced system by lifting them to the full phase space. We use the designation “RPO” for both: the periodic orbit in the reduced system, and for the corresponding 2-torus in the full system. Pre-images of the singular part of  $\Sigma$  are either relative equilibria, other periodic orbits, or bifurcating RPOs (plus possible separatrices). Again, we use the term “relative equilibrium” for both: the equilibrium in the reduced system, and for the corresponding periodic orbit in the full systems. Periodic orbits of the full system that are *not* relative equilibria do exist and play a very important role. They are confined to the set of fixed points under rotations, hence they are periodic orbits both in the full and in the reduced system. Their projections to configuration space are orbits along the  $z$ -axis. The *super-singular part* of  $\Sigma$  corresponds to equilibrium points or bifurcating relative equilibria or bifurcating periodic orbits (plus possible separatrices).

#### 4.1 The structure of $\Sigma$ and $\bar{\Sigma}$ for $\mu < 1/2$

To give a first impression of what  $\Sigma$  looks like, the projection  $\pi_g \Sigma$  of its singular and super-singular parts to the  $(h, l)$ -half-plane of negative  $h$  is shown – for the asymmetric case with  $\mu = 1/3$  in Fig. 9a, and for the symmetric case with  $\mu = 1/2$  in Fig. 9b. The calculations leading to these pictures will be outlined in the following subsections, based on an analysis of the effective potential  $V_{\text{eff}}$  and of the zeros of polynomials  $P_\mu^l(s)$ . A mental picture of the set  $\Sigma$  in  $\mathbb{R}^3(h, g, l)$  may be obtained by imagining the curves of Fig. 9 as lifted to  $(h, g, l)$ -space by  $\pi_g^{-1}$ , and connected by regular  $\Sigma$  sheets. Note, however, that not all singular lines are intersections of (closures of) regular components. We shall see that the bifurcation diagram contains isolated lines: two in the asymmetric, and one in the symmetric case. A comprehensive view of  $\Sigma$  will be given later, in terms of cross sections  $l = \text{const}$ , see Figures 10, 11, 14, and cross sections  $h = \text{const}$ , see Figures 13, 15. We again consider  $\mu = 1/3$  as a typical asymmetric case.

$\Sigma$  possesses five super-singular values  $(h, g, l)$ :

---

the collision singularity or to a codimension 2 subset of  $\Sigma$ , but this should not be a cause of confusion. In order not to clutter the exposition when we talk about “intersection of regular parts” of  $\Sigma$  we mean “intersection of the closure of the regular parts”; otherwise they would be disjoint.

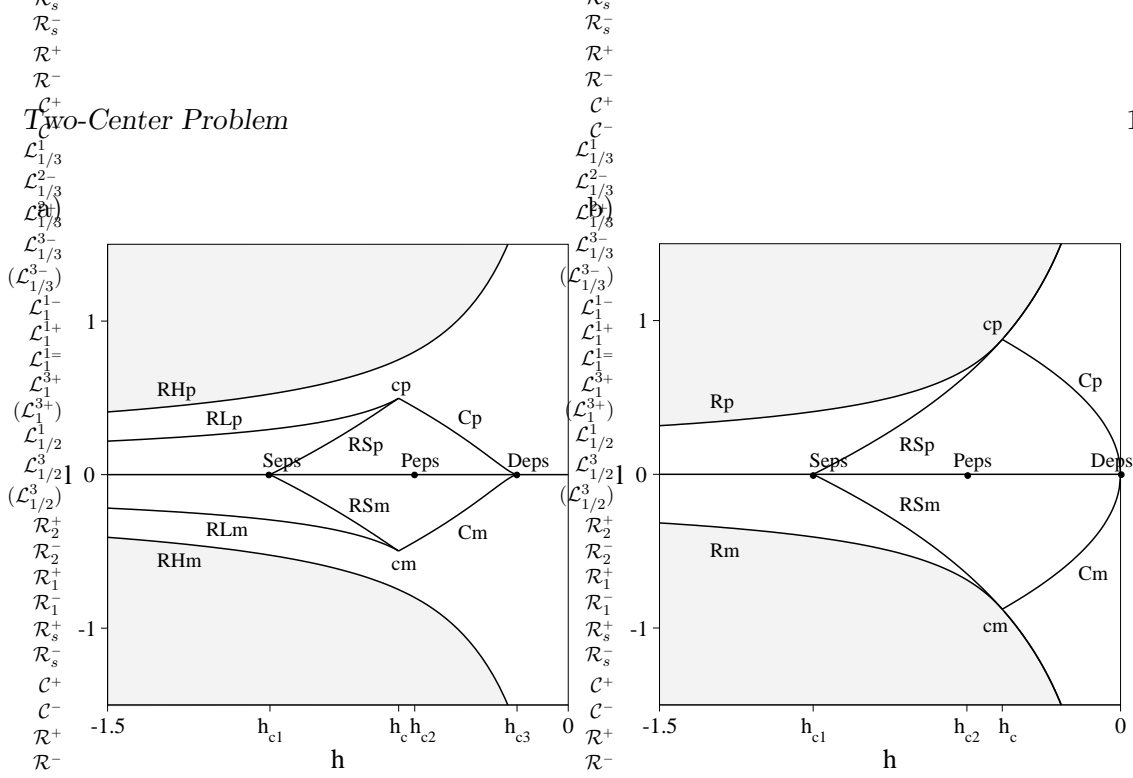


Figure 9: Projection  $\pi_g \Sigma$  of the bifurcation diagram  $\Sigma$  to the  $(h, l)$ -plane; (a) asymmetric case with  $\mu = 1/3$  and (b) symmetric case with  $\mu = 1/2$ .

$S = (h_{c1}, h_{c1} + 1, 0)$  corresponding to the equilibrium point on the axis between the centers. Since this lies on the symmetry axis,  $S$  is an equilibrium in the reduced and in the full system.

$P = (h_{c2}, h_{c2} + 1, 0)$  the pitchfork bifurcation of the planar system, see top of Fig. 7; in the full system this is a Hamiltonian Hopf bifurcation;

$D = (h_{c3}, -h_{c3}, 0)$  the point of inverse period doubling in the planar system, Fig. 7 bottom; again, this a (subcritical) Hamiltonian Hopf bifurcation in the full system;

$C^\pm = (h_c, g_c, \pm l_c) = (-0.5542, 0.1928, \pm 0.4920)$  the points corresponding to the saddle-center bifurcation of the effective potential, i. e., bifurcations of relative equilibria.

A comment is in order on how the pitchfork/period doubling bifurcations are related to the Hamiltonian Hopf bifurcation. In the reduced system both bifurcations are symmetry breaking transitions. This means that the central orbit in the bifurcation consists of fixed points with respect to rotation, while the new orbits do not. Letting the rotation act on these orbits in order to obtain the picture in the full system, the symmetric orbit stays a periodic orbit, while the non-symmetric orbit turns into a 2-torus (in fact, into an RPO).

Before the super-singular set will be analyzed to greater depth, in the next subsection, consider the various curves in  $\pi_g \Sigma$ . The outer boundary is formed by projections of the curves  $\mathcal{R}_2^+$ ,  $\mathcal{R}_2^-$  of maximum  $l^2$  at given energy, or minimum energy at given angular momentum. These curves, as we shall see, represent stable *relative equilibria*, i. e., stable equilibria of the reduced Hamiltonian (8), in this case corresponding to the absolute minimum of the effective potential. The only motion in relative equilibria is rotation in  $\varphi$ , with positive orientation for  $l > 0$ , negative for  $l < 0$ .

The inner curves in  $\pi_g \Sigma$  are projections of four different kinds of curves:

1. The curves  $\mathcal{R}_1^\pm$  extending from the cusps  $C^\pm$  to  $h \rightarrow -\infty$ , are again stable relative equilibria, corresponding to the higher minima of  $V_{\text{eff}}$ .
2. The curves  $\mathcal{R}_s^+$  and  $\mathcal{R}_s^-$  between the cusps and the point  $S$  are unstable relative equilibria, corresponding to saddle points of  $V_{\text{eff}}$ .

3. The curves  $\mathcal{C}^+$  and  $\mathcal{C}^-$  joining the cusps to the point  $D$  correspond to saddle-center bifurcations of RPOs.
4. The line  $l = 0$ ,  $h < 0$ , contains the projections of the three bifurcation lines  $\mathcal{L}_\mu^1$ ,  $\mathcal{L}_\mu^2$ , and  $\mathcal{L}_1^1$  in Fig. 3a. The lines  $\mathcal{L}_\mu^{3-}$  and  $\mathcal{L}_1^{3+}$  are *not* contained in the singular part of  $\Sigma$  in the full system .

These curves divide  $\pi_g \Sigma$  into six regions, three for each sign of  $l$ . Each inner point  $(h, l)$  of these regions is lifted by  $\pi_g^{-1}$  to two, three or four points within regular sheets of  $\Sigma$ . The number is 2 in the outer regions; the two  $\Sigma$ -sheets intersect along the singular curve  $\mathcal{R}_2^\pm$ . The region between  $\mathcal{R}_1^\pm$  and  $\mathcal{R}_s^\pm$  is covered by 3  $\Sigma$ -sheets of critical tori, and the quadrangle with corners  $C^\pm$ ,  $S$  and  $D$  is covered by 4 sheets. The new  $\Sigma$ -sheets branch off the high- $g$  sheet along  $\mathcal{R}_1^\pm$  and  $\mathcal{R}_s^\pm$ ; they vanish in their intersection along the curves  $\mathcal{C}^\pm$ .

To see how the plane  $l = 0$  fits into this picture we recall from Fig. 3a and Eq. (27) that points  $(h, 0)$  on the negative  $h$ -axis are lifted by  $\pi_g^{-1}$  to three singular curves of  $\Sigma$ , and depending on  $h$  up to two additional lines that are part of regular sheets of  $\Sigma$ . It may be helpful to consult Fig. 13 in connection with the following assertions.

$\mathcal{L}_\mu^1$  is the singular line of minimal  $g$  at given  $h$ , associated with the family of motion  $\dot{\cdot}$  that with growing energy first appears near the center  $\mathbf{f}_2$ . Two regular sheets coming from  $\mathcal{R}_2^\pm$  intersect there.

$\mathcal{L}_\mu^2$  is the singular line of lowest  $g$  for the family of motion  $\dot{\cdot}$  that emerges near  $\mathbf{f}_1$ . Two regular sheets coming from  $\mathcal{R}_1^\pm$  meet along  $\mathcal{L}_\mu^{2-}$ . The piece  $\mathcal{L}_\mu^{2+}$  is an isolated singular line joining the point  $D$  to  $(0, 1 - 2\mu, 0)$ .

$\mathcal{L}_1^1$  is the singular line of maximal  $g$  at given  $h$ , provided  $h < h_{c2}$ . Below  $h_{c1}$ , two regular sheets coming from  $\mathcal{R}_2^\pm$  meet in the  $\dot{\cdot}$  part of  $\mathcal{L}_1^{1=}$ , and two other sheets, coming from  $\mathcal{R}_1^\pm$ , meet in the  $\dot{\cdot}$  part of  $\mathcal{L}_1^{1=}$ . Between  $h_{c1}$  and  $h_{c2}$ , two regular sheets coming from  $\mathcal{R}_s^\pm$  meet in the line  $\mathcal{L}_1^{1-}$  which represents the family of stable orbits  $\dot{\cdot}$ . The piece  $\mathcal{L}_1^{1+}$  is a second isolated singular line joining the point  $P$  to  $(0, 1, 0)$ .

$\mathcal{L}_1^{3+}$  is the regular curve of maximal  $g$  for energies  $h > h_{c2}$ . Even though this is a line of critical points for the two degree of freedom system  $l = 0$  ( $\mathcal{M}_2$  has corank 1) it does not lead to a singular line of the bifurcation diagram for the full system ( $\mathcal{M}_3$  has also corank 1). Instead the two regular sheets coming from  $\mathcal{R}_2^\pm$  join smoothly. Nevertheless it turns out to be special as a line representing stable resonant 2-tori.

$\mathcal{L}_\mu^{3-}$  is the regular curve of highest  $g$  for the second family of tori. Like  $\mathcal{L}_1^{3+}$  this is not a singular part of  $\Sigma$ . Two regular sheets coming from  $\mathcal{C}^\pm$  join smoothly. The special feature here is that  $\mathcal{L}_\mu^{3-}$  is a line of unstable resonant 2-tori.

The singular curves  $\mathcal{L}_\mu^1$ ,  $\mathcal{L}_\mu^{2-}$ ,  $\mathcal{L}_1^{1-}$ , are at the intersection of the (closure of) regular sheets;  $\mathcal{L}_1^{3+}$  and  $\mathcal{L}_\mu^{3-}$  are just parts of regular sheets; finally  $\mathcal{L}_\mu^{2+}$  and  $\mathcal{L}_1^{1+}$  are isolated singular lines. They give rise to the monodromy which is the subject of Sec. 6. The reason for the different behavior of  $\mathcal{L}^{1,2}$  and  $\mathcal{L}^3$  under reduction is that the corresponding sets of critical points are sets of fixed points under rotation in the first case, while in the latter case they are not and hence form RPOs.

The closure of the regular sheets of  $\Sigma$  divides the three-dimensional set  $\bar{\Sigma} = \mathcal{M}_3(\mathbb{T}^*Q_3)$  into just two regular connected (but not simply connected, see Sec. 6) parts with topologically different types of motion. This is explained next.

PSfrag replacement

PSfrag replacement

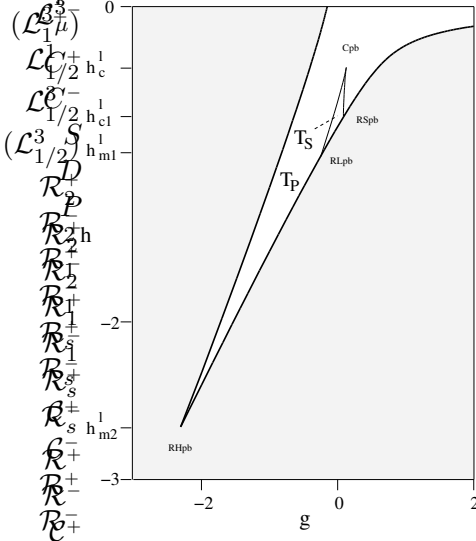
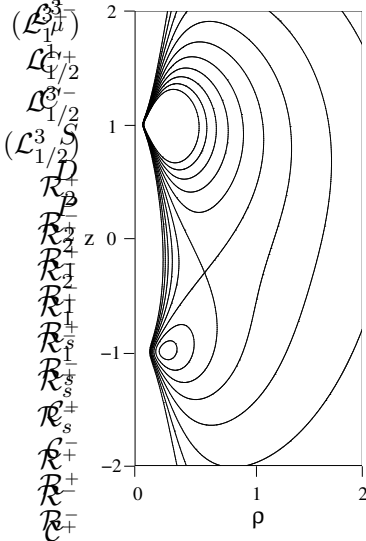


Figure 10: (a) Level lines of the effective potential  $V_{\text{eff}}(\rho, z)$  for  $\mu = 1/3$  and  $l = 0.3$ . (b) Bifurcation diagram  $\Sigma_{g,h}^{0,1/3}$ .

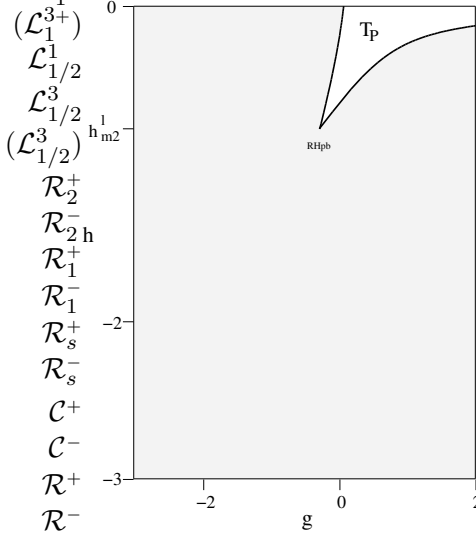
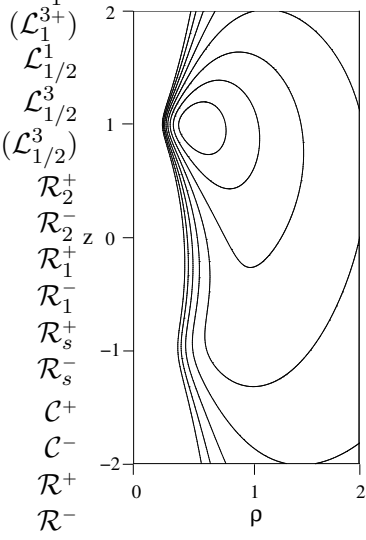


Figure 11: (a) Level lines of the effective potential  $V_{\text{eff}}(\rho, z)$  for  $\mu = 1/3$  and  $l = 0.6$ . (b) Bifurcation diagram  $\Sigma_{g,h}^{0,6}$ .

## 4.2 Relative equilibria and types of motion

A key for understanding the general motion with non-zero angular momentum  $l$  is the analysis of the effective potential  $V_{\text{eff}}$  in (8), see [32]. Our analysis combines this approach for  $l \neq 0$  with the analysis of the case  $l = 0$  into one coherent picture. The centrifugal term  $l^2/2\rho^2$  dominates the potential near the  $z$ -axis, even at the two centers. As a consequence,  $V_{\text{eff}}$  develops two minima of finite depth, the deeper one, with level  $h_{m2}^l$ , near the strong center  $\mathbf{f}_2$ , the higher, with level  $h_{m1}^l$ , near  $\mathbf{f}_1$ . An example, with  $l = 0.3$ , is shown in Fig. 10a. The saddle point has moved away from the point (30) on the  $z$ -axis; we denote its energy level by  $h_{c1}^l$  (for  $l \rightarrow 0$  it approaches  $h_{c1}$ ). When  $l^2$  increases, the higher minimum and the saddle merge in a saddle-centre bifurcation, but the stronger minimum survives for all values of  $l^2$ . The example of  $l = 0.6$  is shown in the left part of Fig. 11. The transition from two minima to one takes place at  $l^2 = l_c^2 = 0.2421$  and  $h = h_c = -0.5542$ , cf. the cusp in Fig. 9. Howard and Wilkerson [32] have shown how to determine these values and, more generally, the curves of relative equilibria, from a critical point analysis of  $V_{\text{eff}}$ . The implications of non-zero angular momentum for (reduced) energy surfaces and possible types of motion are far-reaching.

First, the energy surfaces in the *reduced phase space*  $T^*Q_2^l$ ,

$$\mathcal{E}_h^l := \{(\mathbf{q}, \mathbf{p}) \in T^*Q_2^l \mid H(\mathbf{q}, \mathbf{p}) = h\}, \quad (39)$$

are compact. They may be constructed as usual [9] from the accessible regions in  $Q_2^l$ . As these are always topological disks, the topology of  $\mathcal{E}_h^l$  is *one*  $S^3$  in the range  $h_{m2}^l < h < h_{m1}^l$ , where the motion is confined to the neighborhood of the absolute minimum, *two*  $S^3$  in the range  $h_{m1}^l < h < h_{c1}^l$ , where motion near either minimum is possible, and again *one*  $S^3$  in the range  $h_{c1}^l < h < 0$  where the two neighborhoods have merged.

Second, in contrast to the case  $l = 0$ , there exist only two topologically different types of motion, or regular tori. This is best seen from the analogue of Equations (21) for  $l \neq 0$ , which follows by solving Equations (10) and (11) for  $p_\xi, p_\eta$ :

$$\begin{aligned} p_\xi^2 &= \frac{(\xi^2 - 1)(2h\xi^2 + 2\xi - 2g) - l^2}{(\xi^2 - 1)^2}, \\ p_\eta^2 &= \frac{(1 - \eta^2)(-2h\eta^2 + 2(1 - 2\mu)\eta + 2g) - l^2}{(1 - \eta^2)^2}. \end{aligned} \quad (40)$$

The analysis of their zeros involves the polynomials

$$P_\mu^l(s) = 2(s^2 - 1)(hs^2 - (1 - 2\mu)s - g) - l^2 = P_\mu^0(s) - l^2 \quad (41)$$

which are not as easily factorizable as  $P_\mu^0(s)$ . But clearly,  $P_1^l(\xi)$  is negative in finite  $\xi$ -neighborhoods of  $\pm 1$ , and  $P_\mu^l(\eta)$  is negative in finite  $\eta$ -neighborhoods of  $\pm 1$ . This implies that for any given  $l \neq 0$ , irrespective of the values of  $h$  and  $g$ , certain regions of  $Q_2^l$  are inaccessible to the motion. It would be nice if the roots  $\eta_i$  and  $\xi_i$  could be numbered in such a way that as  $l \rightarrow 0$ , they approach their values in the planar case  $l = 0$ , and at the same time their ordering does not change in continuous deformations of tori. But this is not possible due to collisions of roots in the unphysical ranges  $(-\infty, -1)$  and  $(1, \infty)$  for  $\eta$  and  $(-\infty, 1)$  for  $\xi$ . Therefore we arbitrarily choose the schemes  $1 > \eta_1 > \eta_2 > \eta_3 > \eta_4$  (where the latter two inequalities are only meaningful for real  $\eta_{3,4}$ ) and  $\xi_1 > \xi_2 > 1 > \xi_3 > \xi_4$ . The inaccessible regions are then the interior of the ellipsoid  $\xi = \xi_2 > 1$ ; the interior of the hyperboloid  $\eta = \eta_1 < 1$  with the  $z$ -axis above  $\mathbf{f}_2$ , and the interior of another hyperboloid  $\eta = \text{const}$  containing the  $z$ -axis below  $\mathbf{f}_1$ . The level lines of  $V_{\text{eff}}$  near the  $z$ -axis, in the left parts of Figures 10 and 11, reflect this centrifugal repulsion. A little contemplation shows that the only physically possible types of motion are

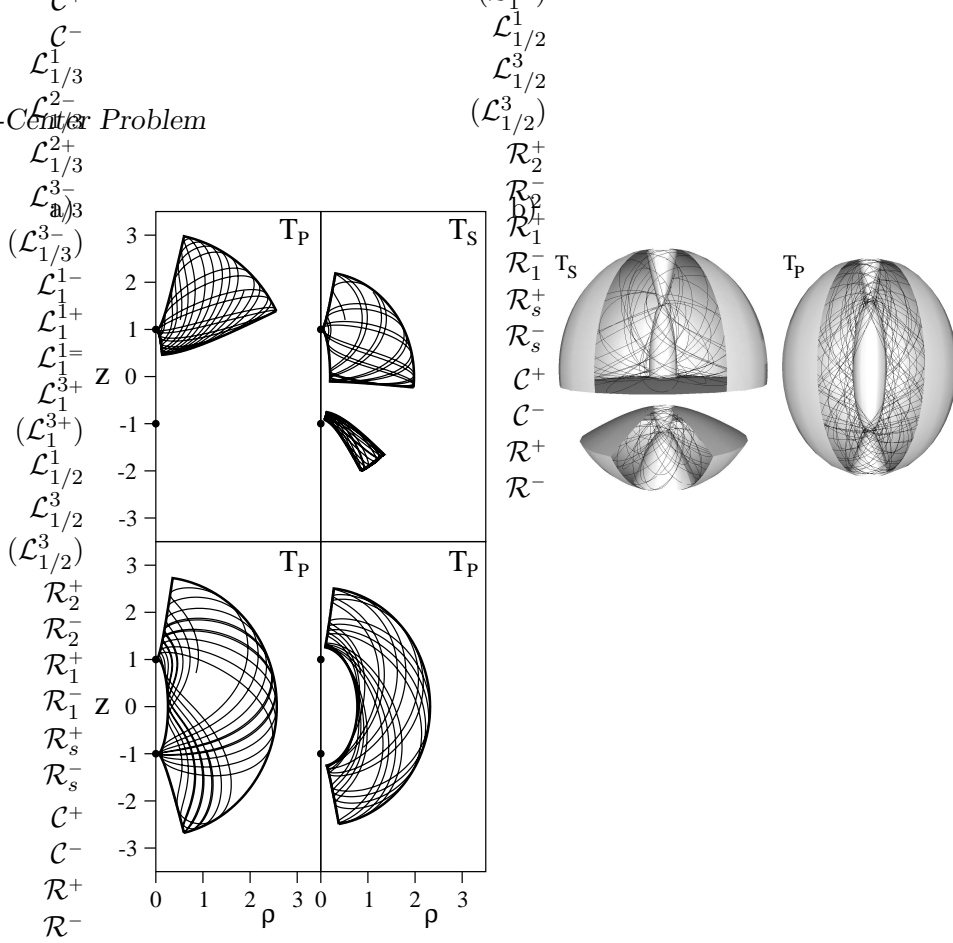


Figure 12: (a) The two types of caustics in the  $(\rho, z)$ -plane for motion with  $l \neq 0$ . The caustics are for the same values of  $g$  and  $h$  as the caustics of the planar system in Fig. 4 but now for a small angular momentum  $l = 0.2$ . The small angular momentum turns all three planar caustics  $\mathbf{t}_s$ ,  $\mathbf{t}_1$  and  $\mathbf{t}_p$  into caustics of type  $\mathbf{T}_P$  while the planar caustic  $\mathbf{t}_s$  leads to  $\mathbf{T}_S$ ; (b) caustics  $\mathbf{T}_S$  ( $(h, g, l) = (-0.525, 0.050, 0.200)$ ) and  $\mathbf{T}_P$  ( $(h, g, l) = (-0.525, 0.200, 0.200)$ ) in  $\mathbb{R}^3(x, y, z)$ .

$$\mathbf{T}_P: \quad 1 < \xi_2 \leq \xi \leq \xi_1 \quad \text{and} \quad -1 < \eta_2 \leq \eta \leq \eta_1 < 1;$$

$$\mathbf{T}_S: \quad 1 < \xi_2 \leq \xi \leq \xi_1 \quad \text{and} \quad -1 < \eta_4 \leq \eta \leq \eta_3 \quad \text{or} \quad \eta_2 \leq \eta \leq \eta_1 < 1.$$

In order to show how these types of motion are related to the four phases of planar motion Fig. 12 shows  $\mathbf{T}_P$  and  $\mathbf{T}_S$  for the same  $h$  and  $g$  as in Fig. 4 but now with a small angular momentum,  $|l| > 0$ . The small angular momentum turns the caustics of each of the phases  $\mathbf{t}_s$ ,  $\mathbf{t}_1$  and  $\mathbf{t}_p$  into caustics of type  $\mathbf{T}_P$ ; the planar phase  $\mathbf{t}_s$  turns into motion of type  $\mathbf{T}_S$ . In phase space,  $\mathbf{T}_S$  consists of two 3-parameter families of 3-tori,  $\mathbf{T}_P$  of only one. We shall see in the next subsection, cf. Fig. 13, that the upper family in  $\mathbf{T}_S$  connects continuously to the  $\mathbf{T}_P$  family, whereas the family of motion in the neighborhood of the light center  $\mathbf{f}_1$  is a disjoint component in phase space (attached to the other family across a separatrix). We introduce the symbols  $\mathcal{T}_H$  for the bigger family, and  $\mathcal{T}_L$  for the smaller.

However,  $V_{\text{eff}}$  does not tell the whole story. The caustics do not follow its level lines. They also depend on the separation constant  $g$ . Let us therefore proceed to a detailed bifurcation analysis using the energy momentum map.

### 4.3 Cross sections of bifurcation diagrams

In principle, like in the case of vanishing  $l$ , the bifurcations could be studied in terms of the discriminant of the polynomials  $P_1^l(\xi)$  and  $P_\mu^l(\eta)$ . However, the expressions turn out to be too complicated to solve them for, say,  $g$  as a function of  $h$  and  $l$ . Therefore we use a trick to obtain cross sections  $\Sigma_{g,h}^l$  ( $l = \text{const}$ ) or  $\Sigma_{g,l}^h$  ( $h = \text{const}$ ) of  $\Sigma$ . (The cross section  $g = \text{const}$  would also be possible but will not be considered.) In these cross sections  $\Sigma$  is a system of lines which may be parameterized by the double zeros  $d_\xi$  of  $P_1^l(\xi)$  or  $d_\eta$

of  $P_\mu^l(\eta)$ . Hence we compare  $P_\mu^l(s)$  with the ansatz

$$P_\mu^l(s) = (s-d)^2(as^2 + bs + c), \quad (42)$$

and equating the coefficients of different powers of  $s$ , we find

$$a = 2h, \quad b = 4hd - 2(1 - 2\mu), \quad c = 2hd^2 - \frac{d^2 + 1}{d}(1 - 2\mu). \quad (43)$$

With  $h$  and  $d$  as parameters, we get for  $\Sigma_{g,l}^h$

$$g(h, d) = h(2d^2 - 1) - \frac{3d^2 - 1}{2d}(1 - 2\mu), \quad (44)$$

$$l^2(h, d) = \left(-2h + \frac{1 - 2\mu}{d}\right)(d^2 - 1)^2. \quad (45)$$

Solving the last equation for  $h$ , we obtain

$$2h(l, d) = -\frac{l^2}{(d^2 - 1)^2} + \frac{1 - 2\mu}{d}, \quad (46)$$

which together with (44) allows us to determine the cross section  $\Sigma_{g,h}^l$ .

These expressions are to be evaluated with  $d = d_\xi$  for  $\mu = 1$  and  $d = d_\eta$  for any  $\mu < 1/2$ . Care must be taken with the choice of parameter ranges for  $d_\xi$  and  $d_\eta$ . We are only interested in  $d_\xi > 1$  and  $-1 < d_\eta < 1$ , but there are further restrictions. Consider, for example, the branch in  $\Sigma_{g,h}^l$  where  $d_\eta = \eta_1 = \eta_2$ . With  $d_\eta$  too close to 1, (46) gives a value for  $h$  below the minimum  $h_{m2}^l$ ; with  $d_\eta$  too close to 0, the energy  $h$  becomes positive. With the appropriate control of  $d_\eta$ , we obtain the branches of minimal  $g$  (at given  $h$ ) in Figures 10b and 11b. For the analogous branch in  $\Sigma_{g,l}^h$ , we start with  $d_\eta = 1$ ,  $l = 0$  and  $g = h - 1 + 2\mu$  (which we know from Fig. 3); upon decreasing  $d_\eta$  we must check whether for the corresponding set  $(h, g, l)$  there exists a  $\xi$ -range  $> 1$  where  $P_1^l(\xi) > 0$ . The branch ends when it meets the branch  $d_\xi = \xi_1 = \xi_2$ . In this way we obtain the left boundaries (for positive and negative  $l$ ) in the diagrams  $\Sigma_{g,l}^h$  of Fig. 13. Similar considerations lead to the other curves in Figures 10b, 11b, and 13.

To analyze the cusps in some of these figures, i. e., the intersections of the curves  $\mathcal{C}^\pm$  with the planes  $l = \text{const}$  in Fig. 10b and  $h = \text{const}$  in Fig. 13, we use the following properties of Equations (44)-(46):

$$\frac{\partial g}{\partial d}\Big|_l = d^2 \frac{\partial h}{\partial d}\Big|_l = \frac{d^2}{1 - d^2} \frac{\partial g}{\partial d}\Big|_h \quad \text{and} \quad \frac{\partial l^2}{\partial d}\Big|_h = 2(1 - d^2) \frac{\partial g}{\partial d}\Big|_h. \quad (47)$$

They show that the cusps  $\partial l^2 / \partial d|_h = 0 = \partial g / \partial d|_h$  in Fig. 13 and  $\partial h / \partial d|_l = 0 = \partial g / \partial d|_l$  in Fig. 10b are given by the zeros of  $\partial g / \partial d|_h$ . Taking the derivative in Eq. (44) and evaluating for  $h$ , then  $l$  and  $g$ , we obtain the relations

$$h = (1 - 2\mu) \frac{3d^2 + 1}{8d^3}, \quad l^2 = (1 - 2\mu) \frac{(d^2 - 1)^3}{4d^3}, \quad g = (1 - 2\mu) \frac{-6d^4 + 3d^2 - 1}{8d^3}. \quad (48)$$

The first two were used to draw the pieces  $\mathcal{C}^\pm$  in Fig. 9.

Let us discuss the cross sections of  $\Sigma$  together with the projection  $\pi_g \Sigma$ . First observe in Fig. 9 that there are just two qualitatively different sections  $\Sigma_{g,h}^l$  (for  $l > 0$ ), and five different types of sections  $\Sigma_{g,l}^h$ . The two  $\Sigma_{g,h}^l$  correspond to whether or not there exists a second minimum of  $V_{\text{eff}}$  besides the absolute minimum. The two parts of Fig. 10 belong to the same value  $l = 0.3$  and are typical for  $l^2 < l_c^2$ . The bifurcation diagram  $\Sigma_{g,h}^l$  consists of four curves and four singular points. The curves are intersections with four

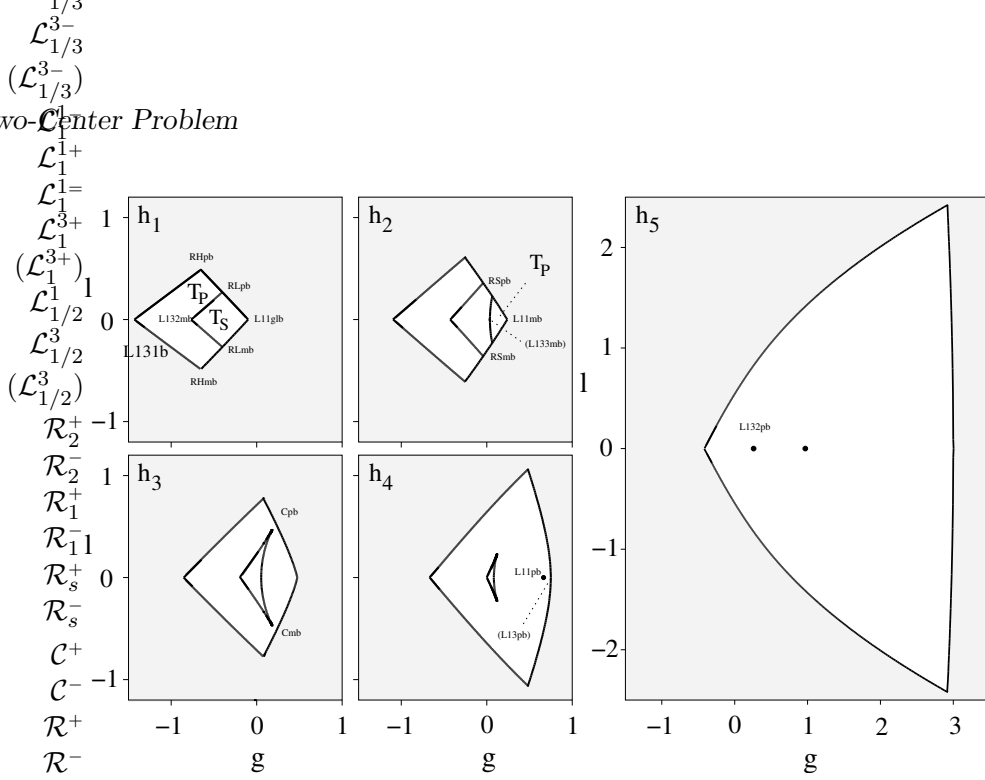


Figure 13: Bifurcation diagrams  $\Sigma_{g,l}^h$  for  $\mu = 1/3$ . Corners and intersection points correspond to the singular part of  $\Sigma$ . The points in parantheses represent resonant RPOs. The energies are  $h_1 = -1.100$ ,  $h_2 = -0.761$ ,  $h_3 = -0.525$ ,  $h_4 = -0.333$  and  $h_5 = -0.083$ . They are separated by  $h_{c1}, h_c, h_{c2}, h_{c3}$ , in this order.

regular sheets of  $\Sigma$ , the points are intersections with singular lines:  $\mathcal{R}_2^+$  at the bottom tip as well as  $\mathcal{R}_1^+$  and  $\mathcal{R}_s^+$  further up on the right boundary, are relative equilibria. The cusp where the two inner curves meet is the intersection with line  $\mathcal{C}^+$ . The triangle  $\mathcal{R}_1^+, \mathcal{R}_s^+, \mathcal{C}^+$  defines the region  $\mathbf{T}_S$  where two tori coexist; its complement in the section with  $\bar{\Sigma}$  is  $\mathbf{T}_P$ . The bottom tip  $\mathcal{R}_2^+$  is a stable relative equilibrium. From it emerge the two non-linear normal modes, which are stable periodic orbits of the  $l$ -reduced system, or stable critical 2-dimensional tori of the full system. These 2-tori are obtained by rotating a periodic orbit of the reduced system, hence they are RPOs. The caustics of the RPOs are rotationally symmetric (pieces of) coordinate-surfaces. The boundary at left in Fig. 10b is given by  $0 < \eta_1 = \eta_2 < 1$ , i. e., the stable RPO projects onto the hyperboloid in the range  $\xi_2 \leq \xi \leq \xi_1$ . Remember that in addition to motion along the hyperbola  $\eta = \eta_1 = \eta_2$  there is  $\varphi$ -motion in the full system: this is what makes the periodic orbit into an RPO. The right boundary is defined by  $1 < \xi_1 = \xi_2$ , and the corresponding stable RPO projects onto one or two pieces of the ellipsoid  $\xi = \xi_1 = \xi_2$ : *one* piece  $\eta_2 \leq \eta \leq \eta_1$  in the energy range  $h < h_{m1}^l$  below  $\mathcal{R}_1^+$ ; *two* pieces  $\eta_4 \leq \eta \leq \eta_3$  and  $\eta_2 \leq \eta \leq \eta_1$  in the energy range  $h_{m1}^l < h < h_{c1}^l$  between  $\mathcal{R}_1^+$  and  $\mathcal{R}_s^+$ ; again only *one* piece  $\eta_2 \leq \eta \leq \eta_1$  above  $\mathcal{R}_s^+$  where  $\eta_3$  and  $\eta_4$  have moved into the complex plane. The piece between  $\mathcal{R}_1^+$  and  $\mathcal{C}^+$  is defined by  $-1 < \eta_4 = \eta_3$ , and the caustic of the stable RPO is on the corresponding hyperboloid. The two families of stable RPOs emerging from  $\mathcal{R}_1^+$  are again non-linear normal modes of that relative equilibrium. The branch between  $\mathcal{R}_s^+$  and  $\mathcal{C}^+$  is defined by the coincidence of roots  $\eta_3 = \eta_2$  and corresponds to an unstable RPO. The stable and unstable families of RPOs annihilate in a saddle-center bifurcation at  $\mathcal{C}^+$ . This diagram can be interpreted as a bifurcation diagram of the  $l$ -reduced system with two degrees of freedom. It is simple enough for the reader to draw the three different Fomenko diagrams (they are similar at low and high energies).

The two parts of Fig. 11 belong to the value  $l = 0.6$  and are typical for  $l^2 > l_c^2$ . Since the saddle and the upper minimum of  $V_{\text{eff}}$  have disappeared,  $\mathbf{T}_P$  is the only type of motion left, starting, at minimal  $g$ , as a stable RPO with caustic on a hyperboloid, and ending, at maximal  $g$ , as a stable RPO with caustic on an ellipsoid.

Consider now the five diagrams  $\Sigma_{g,l}^h$  in Fig. 13, which represent all possible motions for



fixed energy. Their left boundaries correspond to the left boundaries in  $\Sigma_{g,h}^l$ , for the same set of  $(h, g, l)$ -values: they are stable RPOs with caustics on hyperboloids  $\eta = \eta_1 = \eta_2$ . Likewise, the right boundaries correspond to the curves of maximal  $g$  in  $\Sigma_{g,h}^l$ , i. e., to stable RPOs with caustics on ellipsoids  $\xi = \xi_1 = \xi_2$ . The two boundaries meet in the relative equilibria of maximal  $l^2$ , i. e., in the intersections with the singular lines  $\mathcal{R}_2^\pm$ . The other two relative equilibria, if they exist at the given  $h$ , are seen as intersections of the right boundary with inner lines of the diagram: at low energies (energy  $h_1$  in Fig. 13) only  $\mathcal{R}_2^\pm$  and  $\mathcal{R}_1^\pm$  appear. Then  $\mathcal{R}_s^\pm$  emerge, at  $h = h_{c1}$ , from the right apex  $P$  where  $\mathcal{L}_1^{1-}$  turns into  $\mathcal{L}_1^{1-}$ ;  $\mathcal{R}_s^+$  and  $\mathcal{R}_s^-$  are connected by a new internal line of regular values of  $\Sigma$  corresponding to unstable RPOs. In the range  $h_{c1} < h < h_c$  (energy  $h_2$  in Fig. 13) all three relative equilibria are present at the same energy (with both signs of  $\varphi$ -rotation). The saddle-center bifurcation of  $V_{\text{eff}}$  at  $h = h_c$  sees  $\mathcal{R}_1^\pm$  and  $\mathcal{R}_s^\pm$  merging in two cusps  $C^\pm$  on the boundary. The cusps then move inside along the curves  $\mathcal{C}^\pm$  (from  $h_3$  to  $h_4$  in Fig. 13), shrink with growing energy and disappear on the line  $l = 0$  at  $h = h_{c3}$ , leaving behind as an isolated point the intersection with the line  $\mathcal{L}_\mu^{2+}$  (energy  $h_5$  in Fig. 13).

When  $l \neq 0$  every regular value in  $\Sigma$  is a RPO, and every singular value is either a relative equilibrium or a bifurcation of RPOs (at  $\mathcal{C}^\pm$ ). The reason for this simple relation between the reduced and the full system is that the reduction of the rotation is regular when the angular momentum  $l \neq 0$ . If, however,  $l = 0$  this reduction is singular, and neither do all equilibrium points of the reduced system correspond to periodic orbits of the full system, nor do all periodic orbits of the reduced system correspond to 2-tori of the full system. The explanation is simple: whenever the invariant object in the reduced system is fixed under the symmetry operation (i. e., rotation around the  $z$ -axis, lifted to phase space) it does not increase its dimension upon passage to the full system. Hence equilibrium points/periodic orbits of the reduced system that are on the  $z$  axis are also equilibrium points/periodic orbits in the full system. This applies to the lines  $\mathcal{L}_\star^{1,2}$ . As a result these points have corank 1 with respect to  $\mathcal{M}_2$  but corank 2 with respect to  $\mathcal{M}_3$ . The orbits corresponding to  $\mathcal{L}_\star^3$  are not on the symmetry axis, so a rotation turns them into 2-tori of the full system. Their corank therefore stays the same, which explains why they appear as part of regular sheets in  $\Sigma$ .

For points on the line  $l = 0$ , where the centrifugal contribution in  $V_{\text{eff}}$  disappears, we recover the sections  $h = \text{const}$  of the bifurcation diagram  $\Sigma^0$  in Fig. 3a. The point with minimal  $g$  corresponds to the stable orbit  $\dot{\bullet}$  of the planar system. It is the intersection with line  $\mathcal{L}_\mu^1$  and exists for all energies. The point with maximal  $g$  (intersections with lines  $\mathcal{L}_1^{1-}$  and  $\mathcal{L}_1^{3+}$ ) has different interpretations at different values of  $h$ . It corresponds to the *two* stable orbits  $\dot{\bullet}$  and  $\dot{\bullet}$  as long as  $h < h_{c1}$  (energy  $h_1$  in Fig. 13); for  $h_{c1} < h < h_{c2}$  it represents the *one* stable orbit  $\dot{\bullet}$  ( $h_2$  and  $h_3$  in Fig. 13). So far all points with minimal or maximal  $g$  correspond to stable periodic orbits confined to the  $z$ -axis and involving collisions with one or both centers. For  $h > h_{c2}$ , however, see the pictures for energies  $h_4$  and  $h_5$  in Fig. 13, the tangent at the intersection with the line  $\mathcal{L}_1^{3+}$  of the planar system is continuous; at the same time the intersection with  $\mathcal{L}_1^{1+}$  has been ejected to the interior of  $\bar{\Sigma}_{g,l}^h$ , as an isolated point which now corresponds to an *unstable* orbit  $\dot{\bullet}$ . The boundary point with maximal  $g$  is now a RPO and therefore marked by  $(\mathcal{L}_1^{3+})$ . It has the additional special structure that the 2-torus is *resonant*, i. e., it is foliated by periodic orbits of elliptical shape and elliptic-parabolic stability, with different orientation  $\varphi = \text{const}$  of their planes. This bifurcation scheme which for the planar system reduces to the pitchfork bifurcation at the top of Fig. 7, corresponds to a Hamiltonian Hopf bifurcation in the full system.

The lines in the interior of  $\bar{\Sigma}_{g,l}^h$  are of two types. Starting from the singular orbits  $\dot{\cdot}$ , at  $(g, l) = (h + 1 - 2\mu, 0)$  and increasing  $l^2$ , we have RPOs confined to the hyperboloids  $\eta = \eta_3 = \eta_4 > -1$ . For energies  $h < h_c$ , this line meets the outer boundary,  $\xi = \xi_1 = \xi_2$ , in  $\mathcal{R}_1^\pm$ . The phase  $\mathbf{T}_S$  extends to the right of these lines. The other line, connecting the relative equilibria  $\mathcal{R}_s^+$  and  $\mathcal{R}_s^-$ , is characterized by  $\eta_3 = \eta_2$  which means that the RPOs are confined to the neighborhoods of the two centers merge; this is typical for an unstable critical orbit associated with a separatrix. At  $l = 0$  this family of RPOs is the unstable orbit  $\dot{\wedge}$  rotated about the  $z$ -axis. This point is marked by  $(\mathcal{L}_\mu^3 m)$  in Fig. 13. Again, the 2-torus is resonant, foliated by hyperbolic-parabolic orbits of hyperbolic shape  $\dot{\wedge}$  with different orientations  $\varphi = \text{const}$ . At  $h = h_c$  the two internal lines join in a cusp on the outer boundary, and for  $h_c < h < h_{c3}$  form a kite completely inside  $\bar{\Sigma}_{g,l}^h$ . For every  $(h, g, l)$  from inside the kite, there exist two invariant tori; this is motion of type  $\mathbf{T}_S$ . Outside the kite there is exactly one torus for each point  $(h, g, l)$ ; this is motion of type  $\mathbf{T}_P$ . The left apex of the kite (and its continuation to lower energies) is the stable periodic orbit  $\dot{\cdot}$ . This orbit becomes unstable and is the only trace of the kite at  $h \geq h_{c3}$ , when it shrinks to the point  $(g, l) = (h + 1 - 2\mu, 0)$ , the intersection of line  $\mathcal{L}_\mu^{2+} \subset \Sigma$  with the plane  $h = \text{const}$ . This bifurcation is the inverse period doubling bifurcation of the planar system, see Fig. 7 bottom, and is a subcritical Hamiltonian Hopf bifurcation of the general system.

In conclusion, Fig. 13 gives the following picture of the bifurcation scheme in the three-dimensional  $(h, g, l)$ -space of constants of motion. At low energies  $h < h_{c1}$ , the pre-image of  $\mathbf{T}_S$  in phase space consists of two disconnected components. This shows that the interior bifurcation lines  $\mathcal{R}_1^+ - \mathcal{L}_\mu^{2-} - \mathcal{R}_1^-$  are not critical for the family  $\mathcal{T}_H$  of tori; they only mark the birth of the family  $\mathcal{T}_L$  somewhere else in phase space. By continuity we conclude that the lines  $\mathcal{C}^+ - \mathcal{L}_\mu^{2-} - \mathcal{C}^-$  are also not critical for  $\mathcal{T}_H$ . The lines  $\mathcal{C}^+ - \mathcal{L}_\mu^{3-} - \mathcal{C}^-$ , on the other hand, are critical for both families; their pre-images consist of separatrices where the families are singularly connected. This shows that the image  $\mathcal{M}_3(\mathcal{T}_H)$  in  $(h, g, l)$ -space of the family  $\mathcal{T}_H$ , under the momentum mapping, contains two singular objects in its interior: one is the line  $\mathcal{L}_1^{1+}$ , attached to the boundary in the point  $P$ ; the other is the union of line  $\mathcal{L}_\mu^{2+}$  and the two-dimensional set of all images  $\mathcal{C}^+ - \mathcal{L}_\mu^{3-} - \mathcal{C}^-$  of the separatrices.  $D$  is the point where the latter singular object changes from being a line to being two-dimensional.  $C^\pm$  are the points where the singular object first meets the boundary as  $h$  is decreased; it is attached to the boundary along the lines  $\mathcal{R}_s^\pm$ , and disappears in the point  $S$ . By contrast, the image  $\mathcal{M}_3(\mathcal{T}_L)$  of the family  $\mathcal{T}_L$ , i. e., area  $\mathbf{T}_S$ , contains no singularity in its interior.

#### 4.4 The symmetric system $\mu = 1/2$

The symmetric case  $\mu = 1/2$  is simpler but deserves special attention. The projection of its bifurcation diagram  $\Sigma$  to the  $(h, l)$ -plane is shown in Fig. 9b. The curves of relative equilibria are now organized in a different manner. As shown in detail by Howard and Wilkerson [32],  $V_{\text{eff}}(\rho, z)$  has a single minimum at  $(\rho, 0)$  with  $\rho > \sqrt{2}$  for sufficiently large  $l^2$ . With decreasing  $l^2$ , this critical point undergoes a pitchfork bifurcation at  $(V_{\text{eff}}, l^2) = (h_c, l_c^2) = (-2, 4)\sqrt{3}/9 = (-0.3849, 0.7698)$ . It turns into a saddle point at  $(\rho, 0)$  with  $\rho < \sqrt{2}$  and ejects two symmetric minima which approach the centers  $\mathbf{f}_1$  and  $\mathbf{f}_2$  as  $l^2 \rightarrow 0$ . Because of the system's symmetry the curves  $\mathcal{R}_2^+$  and  $\mathcal{R}_1^+$  ( $\mathcal{R}_2^-$  and  $\mathcal{R}_1^-$ ) are now identical and will be called  $\mathcal{R}^+$  ( $\mathcal{R}^-$ ). For  $l^2 < l_c^2$ ,  $\mathcal{R}^+$  and  $\mathcal{R}^-$  each represent *two* stable relative equilibria, as limiting cases of the two disjoint caustics of type  $\mathbf{T}_S$ . For  $l^2 > l_c^2$ , they correspond to limiting cases of the single type  $\mathbf{T}_S$ . The curves  $\mathcal{R}_s^\pm$  related to the unstable relative equilibria meet in  $(h, l) = (-1, 0)$ . For energies below  $h = h_{c1} = -1$  there is no motion of type  $\mathbf{T}_P$ .

The super-singular points are  $S = (-1, 0, 0)$ ,  $P = (-\frac{1}{2}, \frac{1}{2}, 0)$ ,  $D = (0, 0, 0)$ , cf. Fig. 3

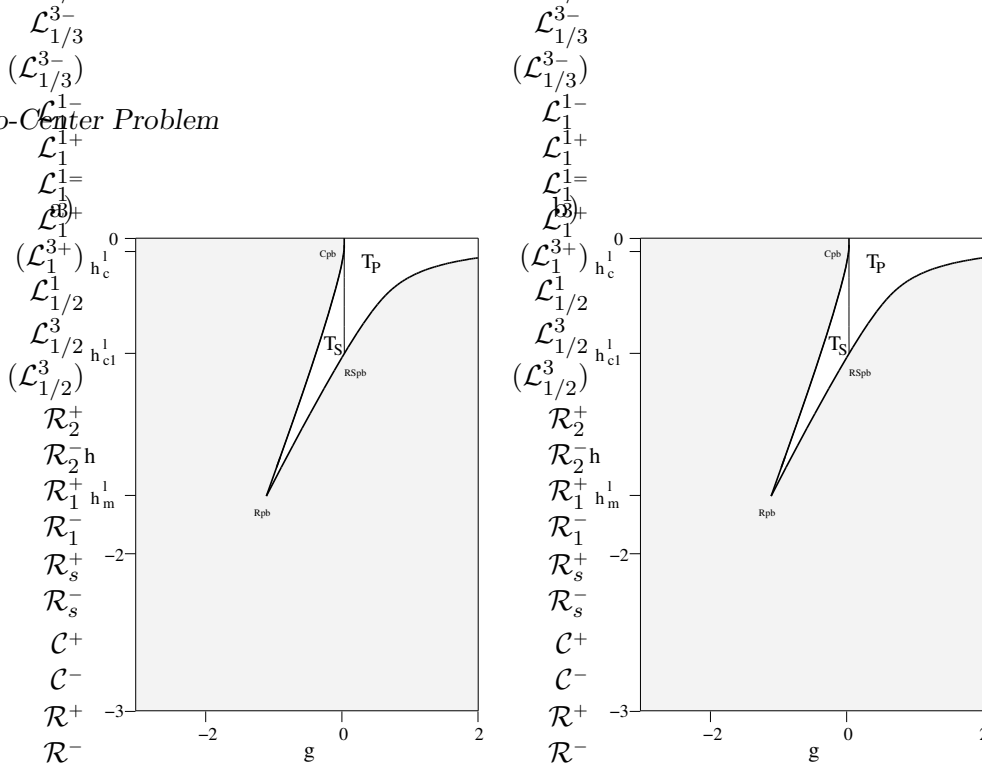


Figure 14: Bifurcation diagrams  $\Sigma_{g,h}^l$  for the symmetric system  $\mu = 1/2$ ;  $l = 0.3$  (a) and  $l = 0.9$  (b).

and Eq. (32), and the points  $C^\pm = (h_c, g_c, \pm l_c) = (-0.3849, 0.3849, \pm 0.8774)$  related to the saddle-center bifurcation of  $V_{\text{eff}}$ , see [32]. To derive the curves  $C^\pm$  in Fig. 9b as well as the cross sections  $\Sigma_{g,h}^l$  in Fig. 14 and  $\Sigma_{g,l}^h$  in Fig. 15, we study again the double zeros of the polynomials  $P_\mu^l(s)$ . Nothing changes for  $P_1^l(\xi)$ , but  $P_{1/2}^l(\eta)$  has new features because it is even in  $\eta$ . Assuming  $d_\eta$  to be a double root we have from (41) and (42)

$$P_{1/2}^l(\eta) = 2h\eta^4 - 2(h+g)\eta^2 + 2g - l^2 = 2h(\eta^2 - d_\eta^2)^2. \quad (49)$$

Comparing coefficients we find, instead of (44) and (45), the following parameterization for the left boundary of  $\Sigma_{g,l}^h$ :

$$g(h, d_\eta) = h(2d_\eta^2 - 1) \quad \text{and} \quad l^2(h, d_\eta) = -2h(d_\eta^2 - 1)^2. \quad (50)$$

Eliminating  $d_\eta$  we obtain

$$g = h + \sqrt{-2hl^2}. \quad (51)$$

This relation may also be used to get the left part of the curves in  $\Sigma_{g,h}^l$ . But notice that it only applies as long as  $d_\eta^2 > 0$ , or  $g < l^2/2$ , or  $g < -h$ . When  $g$  reaches the value  $l^2/2$  at  $h = -l^2/2$ , the fourfold root  $d_\eta = 0$  takes over, and the RPOs are characterized by

$$l^2 = 2g, \quad (52)$$

irrespective of  $h$ . In fact, the singular curves  $C^\pm$  are given by the two conditions

$$l^2 = 2g = -2h. \quad (53)$$

They start at  $C^\pm = (h_c, g_c, \pm l_c) = (h_c, -h_c, \pm\sqrt{-2h_c})$  with  $h_c = -2\sqrt{3}/9 = -0.3849$  and end in  $D = (0, 0, 0)$ . For  $g > -h$  in the rightmost picture of Fig. 15, and for  $h > -l^2/2$  in both pictures of Fig. 14, the relation (52) characterizes stable RPOs with  $\eta = 0$ , i. e., motion in the plane  $z = 0$ . For  $g < -h$  in Fig. 15, and for  $h < -l^2/2$  in Fig. 14a, the same relation characterizes unstable RPOs with  $\eta = 0$ . The distinction is reflected in the second derivative of  $P_{1/2}^l(\eta)$  at  $\eta = 0$  which is  $-4(h+g)$ . If it is negative,  $\eta = 0$  is the only possible value of the RPO; if it is positive, the RPO has a separatrix with a finite range of possible  $\eta$ -values.

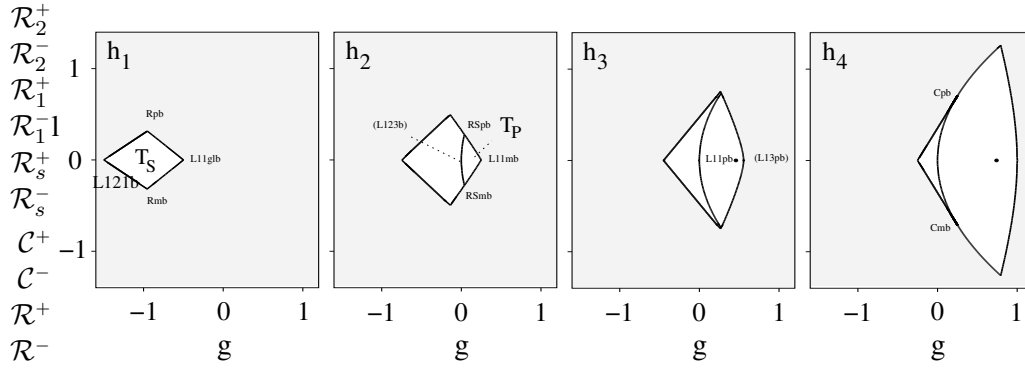


Figure 15: Bifurcation diagrams  $\Sigma_{g,l}^h$  for the symmetric case  $\mu = 1/2$ . Corners and intersection points correspond to the singular part of  $\Sigma$ .  $(\mathcal{L}_1^{3+})$  marks a resonant RPO. The energies are  $h_1 = -1.50$ ,  $h_2 = -0.75$ ,  $h_3 = -0.45$  and  $h_4 = -0.25$ .

Comparing the bifurcation diagrams of Fig. 15 with those in Fig. 13, we observe three major differences. First, motion of type  $\mathbf{T_P}$  occurs only to the right of the curve  $l^2 = 2g$ . Second, the kite structure which contains motion of type  $\mathbf{T_S}$  is always attached to the left boundary. Third, and as a consequence of the last point, there exists at most one isolated singular point, namely, the intersection  $(g, l) = (h + 1, 0)$  with  $\mathcal{L}_1^{1+}$ , for  $h > -0.5$ .

In contrast to the asymmetric case, there are now three families of 3-tori in phase space: two disjoint pre-images of the phase  $\mathbf{T_S}$ , free of internal singularities, and one pre-image of phase  $\mathbf{T_P}$  which contains the singular line  $\mathcal{L}_1^{1+}$ . Their only connection is by separatrices.

## 5 Actions

Action variables can be obtained from integrating the Liouville differential  $\mathbf{p}d\mathbf{q}$  along independent cycles  $\gamma_i$  on the tori in phase space. For a separable system it is natural to choose a basis of cycles whose projections onto configuration space coincide with the coordinate lines of the separating coordinates, in our case

$$\gamma_\varphi : d\eta = d\xi = 0, \quad \gamma_\eta : d\varphi = d\xi = 0, \quad \gamma_\xi : d\varphi = d\eta = 0. \quad (54)$$

The corresponding *natural actions* are

$$I_\varphi := \frac{1}{2\pi} \oint_{\gamma_\varphi} p_\varphi d\varphi = l, \quad I_\eta := \frac{1}{2\pi} \oint_{\gamma_\eta} p_\eta d\eta, \quad I_\xi := \frac{1}{2\pi} \oint_{\gamma_\xi} p_\xi d\xi, \quad (55)$$

where  $p_\eta$  and  $p_\xi$  are given by Eqs. (21) or (40). Any other choice of actions is related to these by a unimodular transformation. The  $(I_\varphi, I_\eta, I_\xi)$  are referred to as “natural” not only because of the separating coordinates:  $I_\varphi = l$  has an immediate physical interpretation, and the vanishing of  $I_\eta$  or  $I_\xi$  indicates stable critical motion. Furthermore, the natural actions respect the discrete symmetry of time reversal combined with inversion of the angular momentum. Different sets of actions do not have these properties as will be explained in the following. When  $l = 0$  the cycles  $\gamma_\eta$  and  $\gamma_\xi$  are not independent due to the coordinate singularity; this is important for the calculation of monodromy, see Sec. 6.

As usual in most non-trivial cases, it is not possible to explicitly express the Hamiltonian in terms of action variables. But if the actions are known as functions of the constants  $(h, g, l)$ , the vector of frequencies  $(\omega_\varphi, \omega_\eta, \omega_\xi)$  of the motion on the Liouville-Arnold tori can be obtained from the identity

$$(1, 0, 0) = (\omega_\varphi, \omega_\eta, \omega_\xi) \frac{\partial(I_\varphi, I_\eta, I_\xi)}{\partial(h, g, l)} \quad (56)$$

where the first row of the Jacobian is simply  $(0, 0, 1)$  since  $I_\varphi = l$ .

Let us first discuss the nature of the action integrals. The computation of  $I_\eta$  and  $I_\xi$  leads to the integrals

$$I_s = \sigma_s \frac{1}{\pi} \int_{s_-}^{s_+} \sqrt{P_\mu^l(z)} \frac{dz}{z^2 - 1}, \quad s = \eta, \xi, \quad (57)$$

where  $\sigma_\eta = -1$  and  $\sigma_\xi = 1$  are just signs introduced for convenience, and the integration boundaries  $s_-$  and  $s_+$  are pairs of successive real roots of the respective polynomial  $P_\mu^l$ , in the interval  $[-1, 1]$  for  $\eta$  and in  $[1, \infty)$  for  $\xi$ . It is useful to consider the integrals in the complex plane. Then, the proper definition of the square root of  $P_\mu^l$  in the integrand gives rise to the introduction of the elliptic curves

$$\Gamma_s := \{(w_s, z) \in \overline{\mathbb{C}}^2 \mid w_s^2 = P_\mu^l(z)\}. \quad (58)$$

On these curves the actions  $I_\eta$  and  $I_\xi$  are complete elliptic integrals

$$I_s = \sigma_s \frac{1}{2\pi} \oint_{c_s} \frac{w_s}{z^2 - 1} dz \quad (59)$$

where the  $c_s$  are closed *real cycles* on the Riemann surfaces  $\Gamma_s$ , i. e., cycles on which both  $z$  and  $w_s$  are real. These cycles are closely related to the cycles  $\gamma_\eta$  and  $\gamma_\xi$  on the Liouville-Arnold tori in phase space, as will become clear in the following.

Note that the action  $I_\varphi = l$  appears as the residue of the differentials in Eq. (59) at  $z = \pm 1$ ,

$$\text{Res}_{z=\pm 1} \frac{w_s}{z^2 - 1} dz = \pm \frac{1}{2} \sqrt{-l^2}. \quad (60)$$

Accordingly, the action integrals  $I_\eta$  and  $I_\xi$  are of the third kind if  $l \neq 0$ . Another pole with non-zero residue lies at infinity. Substituting  $z = 1/t$  and investigating the new integrand at  $t = 0$  we find

$$\text{Res}_{z=\infty} \frac{w_s}{z^2 - 1} dz = \frac{2\mu - 1}{\sqrt{2h}}, \quad (61)$$

again with the understanding that formally  $\mu = 1$  for  $s = \xi$ . We conclude that the action  $I_\xi$  is always of the third kind, while  $I_\eta$  is of the third kind except when  $l = 0$  and  $\mu = 1/2$ , i. e., in the planar symmetric case where  $I_\eta$  is of the second kind.

## 5.1 The case of planar motion

In the planar case the actions  $I_\eta$  and  $I_\xi$  can be rewritten in the form

$$I_s = \frac{-h}{\pi} \oint_{c_s} (s_+ - z)(z - s_-) \frac{dz}{w_s} = \frac{-2h}{\pi} \int_{s_-}^{s_+} (s_+ - z)(z - s_-) \frac{dz}{w_s}, \quad (62)$$

where the integration boundaries  $s_-$  and  $s_+$  are pairs of successive real roots of  $w_s^2 = P_\mu^0(s)$  as defined in Eq. (23). Tab. II summarizes what we obtained in Sec. 3 for the relevant roots  $\eta_\pm$  and  $\xi_\pm$ , in the four phases  $\mathbf{t}_s$ ,  $\mathbf{t}_s$ ,  $\mathbf{t}_1$  and  $\mathbf{t}_p$ . The two senses of rotational motion in phase  $\mathbf{t}_p$  will be taken care of by different signs of  $I_\eta$ . For a systematic discussion of the integrals  $I_s$  it is convenient to interpret them as closed-loop integrals (“periods”) on the elliptic curves  $\Gamma_s$ . The two columns at right in Tab. II show how the loops  $c_\eta$  and  $c_\xi$  surround the relevant roots on  $\Gamma_\eta$  and  $\Gamma_\xi$ , respectively.

We saw in Sec. 3.2 that in the asymmetric case there exist four different types of Liouville foliations of the energy surfaces in phase space, see Fig. 5a, while in the symmetric case the number is three, see Fig. 5b. Let us now consider the action representation of the energy surfaces, i. e., the lines  $h = \text{const}$  in the  $(I_\eta, I_\xi)$ -plane of actions. In such a

2-tori	$\eta_-$	$\eta_+$	$\xi_-$	$c_\eta$	$c_\xi$
$\mathbf{t}_{s'}$	$\eta_3$	1	1		
$\mathbf{t}_s$	$\eta_3$	1	1		
				and	
	-1	$\eta_4$	1		
$\mathbf{t}_1$	-1	1	1		
$\mathbf{t}_p$	-1	1	$\xi_4$		

Table II: Integration boundaries  $s_-$  and  $s_+$  for the actions integrals Eq. (62), and integration paths  $c_s$  on the corresponding elliptic curves  $\Gamma_s$ . The signs below and above the slits on the real axis indicate the sign of  $w_s$ .

representation the frequency vectors  $(\omega_\eta, \omega_\xi)^t$  are normal to the energy surface whereas the rotation numbers

$$W_{\eta\xi} = \frac{\omega_\eta}{\omega_\xi} = - \left. \frac{dI_\xi}{dI_\eta} \right|_h = - \frac{\partial I_\xi / \partial g}{\partial I_\eta / \partial g} \quad (63)$$

are given by their slopes. The latter equality shows that  $W_{\eta\xi}$  can easily be calculated from the derivatives of  $I_s$  with respect to  $g$ ,

$$\frac{\partial I_s}{\partial g} = -\sigma_s \frac{1}{2\pi} \oint_{c_s} \frac{dz}{w_s}. \quad (64)$$

These are elliptic integrals of the first kind.

The action representation of energy surfaces is particularly important for the corresponding quantum system. Then, the EBK quantization is obtained with a regular lattice of mesh width  $\hbar$  in the space of actions: lattice sites on energy surfaces correspond to semi-classical quantum states.

For the asymmetric case the energy surfaces in  $(I_\eta, I_\xi)$ -representation are shown in the top part of Fig. 16. Part b corresponds to the branch of  $\mathbf{t}_s$  where motion is confined to the neighborhood of the light center  $\mathbf{f}_1$ ; the actions on this branch are denoted by  $(I'_\eta, I'_\xi)$ . All other branches of motion (cf. Fig. 5a) are represented in part a. Negative values of  $I_\eta$  correspond to rotational motion with negative sense (at  $h > h_{c2}$ ). The values of  $I_\xi$  are always non-negative.

Let us first interpret points on the axes of the diagram.  $I_\eta = 0$  is motion along the  $z$ -axis,  $\dot{\cdot}$  in Fig. 16a and  $\dot{\cdot}$  in Fig. 16b (for  $h < h_{c3}$ ). Motion with  $I_\xi = 0$  is either rotation along an ellipse,  $\left(\dot{\cdot}\right)$  at  $I_\eta > 0$  and  $\left(\dot{\cdot}\right)$  at  $I_\eta < 0$  (for  $h > h_{c2}$ ), or motion along the  $z$ -axis between the two centers:  $\dot{\cdot}$  in the range  $h_{c1} < h < h_{c2}$ ,  $\dot{\cdot}$  and  $\dot{\cdot}$  for  $h < h_{c1}$ . All this is indicated by the labels that were introduced in Fig. 5 and Table I. The system of separatrices corresponding to the unstable critical orbits  $\dot{\cdot}$ ,  $\dot{\cdot}$  and  $\dot{\cdot}$  is also shown, and their bifurcations are indicated by letters S, P, D, in accordance with the bifurcation diagram Fig. 9. The dashed line connecting  $D$  to the origin in Fig. 16a separates region  $\mathbf{t}_{s'}$  from region  $\mathbf{t}_s$ , i.e. the tori to the right of this line coexist with tori which for the same

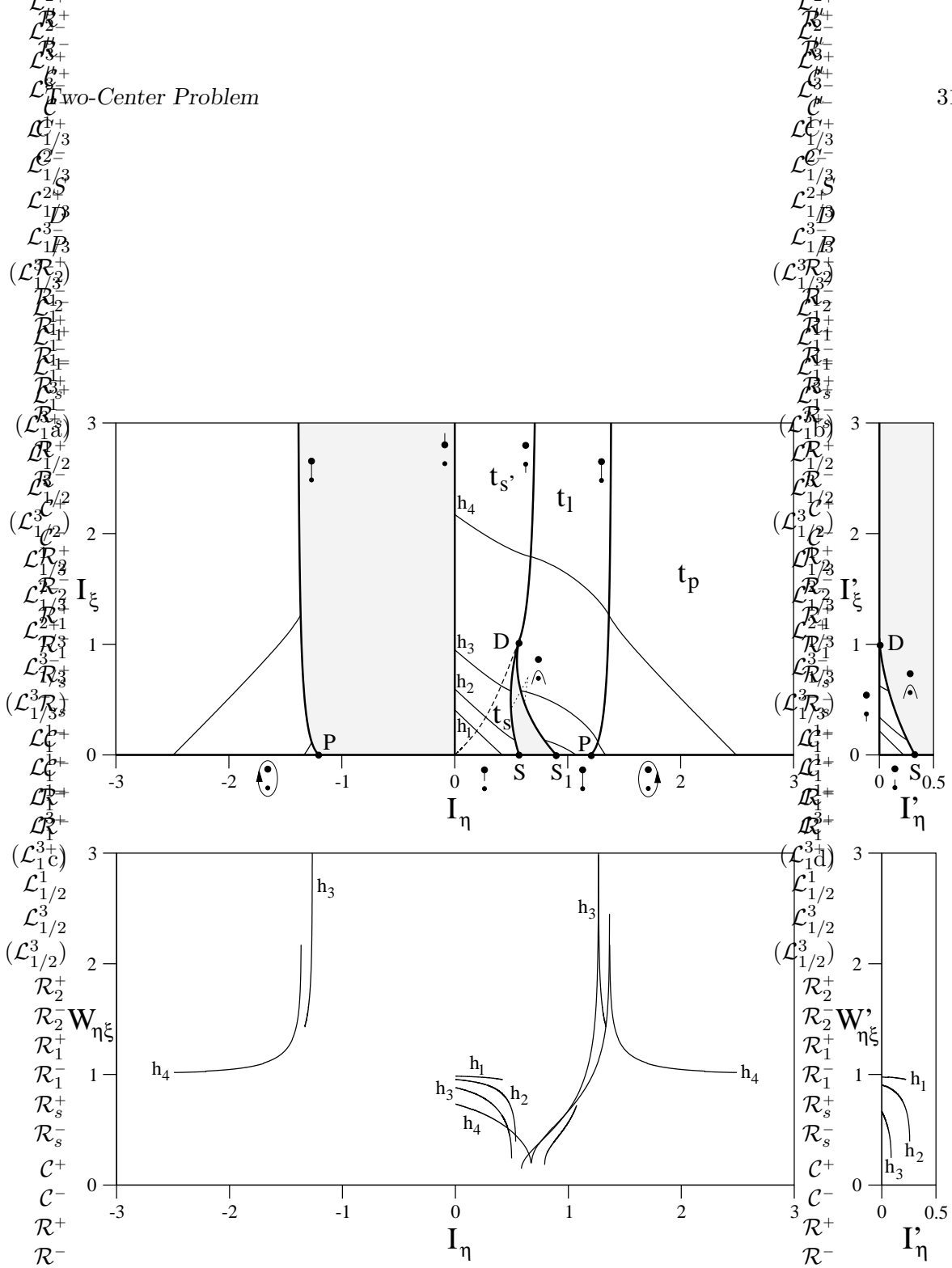


Figure 16: a) Energy surfaces in  $(I_\eta, I_\xi)$ -representation for the asymmetric planar case with  $\mu = 1/3$ , except for the part of phase  $t_s$  where the motion is confined to the neighborhood of the center  $f_1$ . b)  $(I'_\eta, I'_\xi)$  representation of the latter motion in  $t_s$ . The energies are the same as in Fig. 6. c) and d) show the corresponding rotation numbers  $W_{\eta\xi} = \omega_\eta/\omega_\xi$  and  $W'_{\eta\xi}$  as functions of  $I_\eta$  and  $I'_\eta$ , respectively. For reasons of representation  $-W_{\eta\xi}$  is shown for  $I_\eta < 0$ .

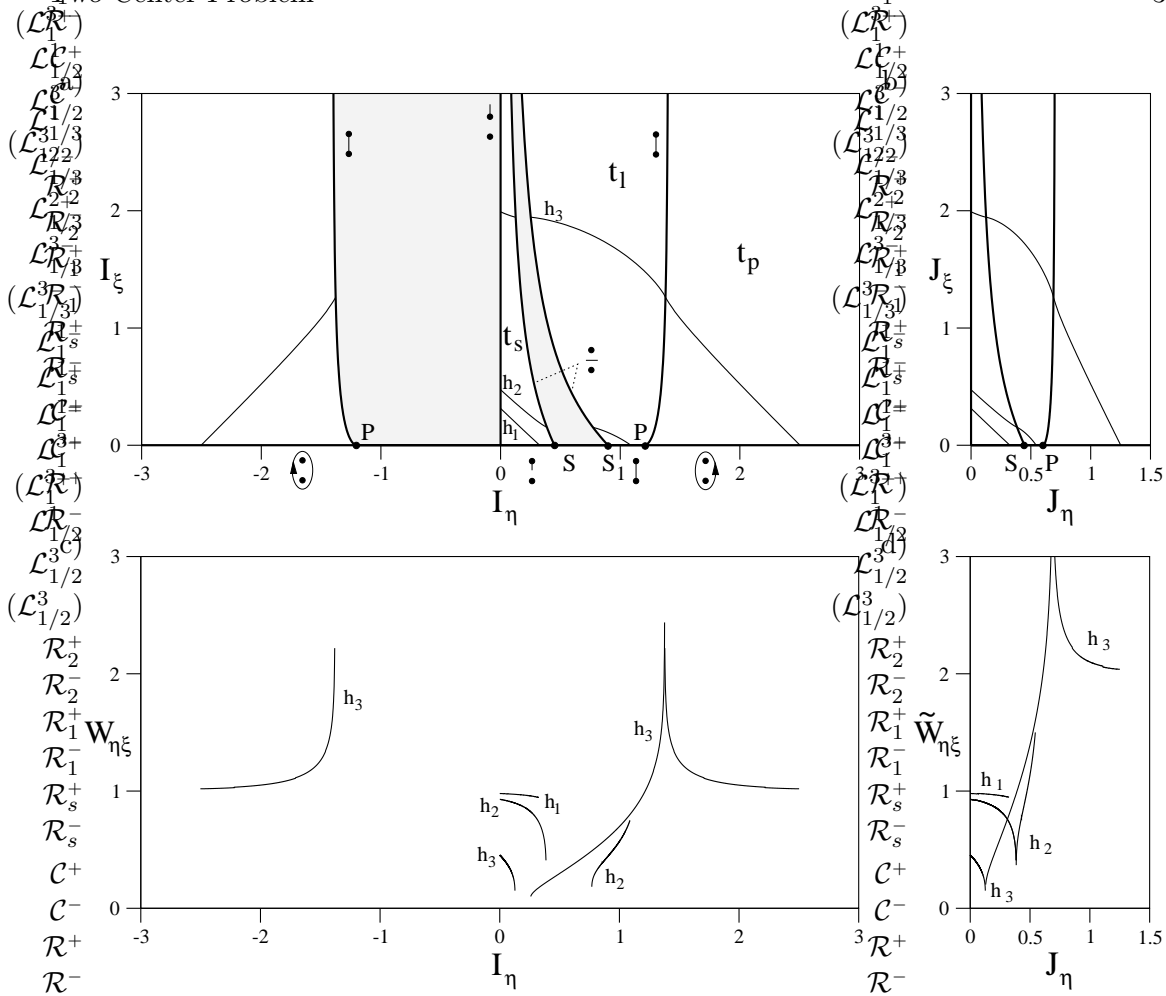


Figure 17: a) Energy surfaces in  $(I_\eta, I_\xi)$ -representation for the symmetric planar case. b) The corresponding actions  $(J_\eta, J_\xi)$  for the symmetry reduced system. The energies  $h_1, h_2, h_3$  are the same as in Fig. 16. c) and d) show the corresponding rotation numbers  $W_{\eta\xi} = \omega_\eta/\omega_\xi$  and  $\tilde{W}_{\eta\xi}$  as functions of  $I_\eta$  and  $J_\eta$ , respectively. For reasons of representation  $-W_{\eta\xi}$  is shown for  $I_\eta < 0$ .

$h$  and  $g$  are located about the light center  $f_1$ . This line represents no separatrix. Pairs  $(I_\eta, I_\xi)$  in the shaded regions do not occur as natural actions. An interesting forbidden region is the triangle in part a) which is bounded on both sides by the unstable critical orbits  $\dot{\rho}$ . Lines of constant energy jump from its left border to the right at fixed  $I_\xi$ , with an increment in  $I_\eta$  which can be read off Fig. 16b. The interpretation of this behavior is that the merging along the orbit  $\dot{\rho}$  of the two tori in phase  $t_s$  is reflected in the additive combination of their  $\eta$ -actions.

The lines of constant energy are shown for the same four parameters  $h_i$  as in Fig. 6. They seem to go smoothly through the separatrices, but closer inspection shows that, as usual, their slopes diverge logarithmically. This is shown in the bottom part of Fig. 16 where the rotation numbers  $W_{\eta\xi}$  are plotted against the actions  $I_\eta$ .

Energy surfaces for the symmetric case, and the corresponding rotation numbers, are shown in Figures 17a and c. Compared to the asymmetric case the main difference is that the point C has moved to infinite values of  $I_\xi$ .

The symmetric planar two center problem possesses reflection symmetry with respect to the two Cartesian coordinate axes  $y = 0$  and  $z = 0$ . This may be used to define a simpler *symmetry reduced system* by factoring out the symmetries, with actions  $(J_\eta, J_\xi)$ . In physical terms, we may think of introducing reflecting planes so that the motion is confined to the quadrant  $x, z \geq 0$ . Rotational motion is thereby turned into oscillatory



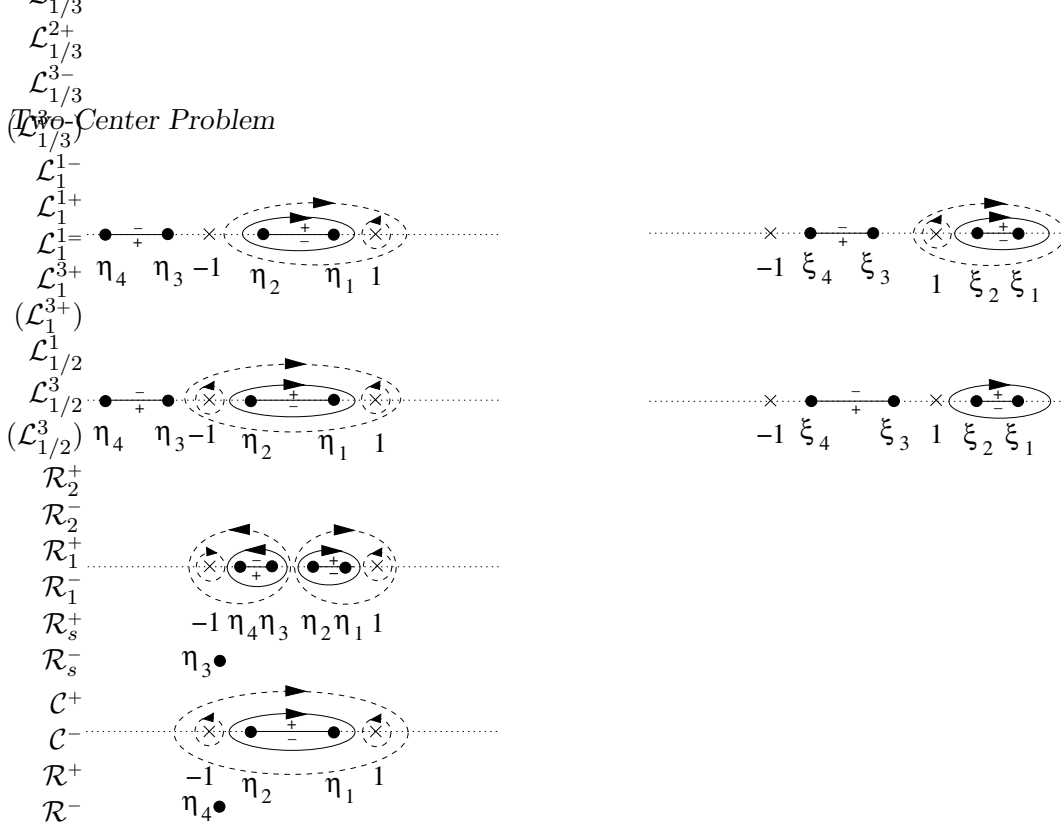


Figure 18: Integration paths  $c_\eta$  (left) and  $c_\xi$  (right) for the integrals  $I_\eta$  and  $I_\xi$  according to Eq. (59). From top to bottom, the left column shows the arrangement of  $\eta$ -zeros resulting from a small non-zero angular momentum  $l$  and values  $(h, g)$  which for  $l = 0$  would lead to  $\eta$ -regions II to V in Fig. 2. Similarly the right column represents the arrangement of  $\xi$ -zeros when a small angular momentum is added in  $\xi$ -regions II and III.

motion, hence all actions are now positive.  $I_\xi$  is unaffected by this reduction,  $J_\xi = I_\xi$ . The same is true for the  $\eta$ -action in phase  $\mathbf{t}_s$ ,  $J_\eta = I_\eta$ , but in phases  $\mathbf{t}_1$  and  $\mathbf{t}_p$  it is reduced to  $J_\eta = \frac{1}{2}I_\eta$ . As a consequence, the energy surface becomes continuous, cf. Figures 17b and d. In this representation they serve as a convenient starting point for a semiclassical quantization. The different parities of the quantum mechanical wave functions of the full system can be taken into account by imposing Dirichlet or Neumann boundary conditions on the symmetry lines.

## 5.2 General $l$

The expression Eq. (59) remains applicable in the case  $l \neq 0$ , but as discussed in Sec. 4, the elliptic curves  $\Gamma_\eta$ ,  $\Gamma_\xi$ , and the integration paths  $c_\eta$  and  $c_\xi$  are different. The real roots  $\eta_{1,2}$  and  $\xi_{1,2}$  are repelled from the points  $z = \pm 1$  which in turn become poles of the action integrand with residues given in Eq. (60). This is depicted in Fig. 18 which shows the various relevant arrangements of roots of  $P_\mu^l(\eta)$  (left) and  $P_1^l(\xi)$  (right), together with the paths  $c_\eta$  and  $c_\xi$ , for the same  $(h, g)$  that lead to the pictures in Tab. II but with a small non-zero angular momentum  $l$ . The full lines correspond to the immediate definition of the integrals, the dashed lines are equivalent deformations and will be discussed in Sec. 6.

There are effectively only two kinds of root structure, corresponding to the phases  $\mathbf{T}_s$  and  $\mathbf{T}_p$ . In phase  $\mathbf{T}_s$  the root structure of  $P_1^l(\xi)$  is given by the first line on the right, that of  $P_\mu^l(\eta)$  by the third line on the left of Fig. 18. Of the two  $\eta$ -loops there, the right one corresponds to motion near the center  $\mathbf{f}_2$  and serves to compute  $I_\eta$ , the left one corresponds to motion near the center  $\mathbf{f}_1$  and serves to compute  $I'_\eta$ . All other root structures evolving from those for  $l = 0$ , see Tab. II, lead to only one kind of oscillatory  $\eta$ -motion, and to only one kind of oscillatory  $\xi$ -motion. This is characteristic of phase  $\mathbf{T}_p$ .

The five different bifurcation diagrams  $\Sigma_{g,l}^h$  of Fig. 13 translate into the five parts of Fig. 19. They show surfaces of constant energy  $\mathcal{E}_h$  in the space of natural actions  $(I_\varphi, I_\eta, I_\xi)$  for the same energies  $h_1$  through  $h_5$ . As in the planar case, separate pictures represent the

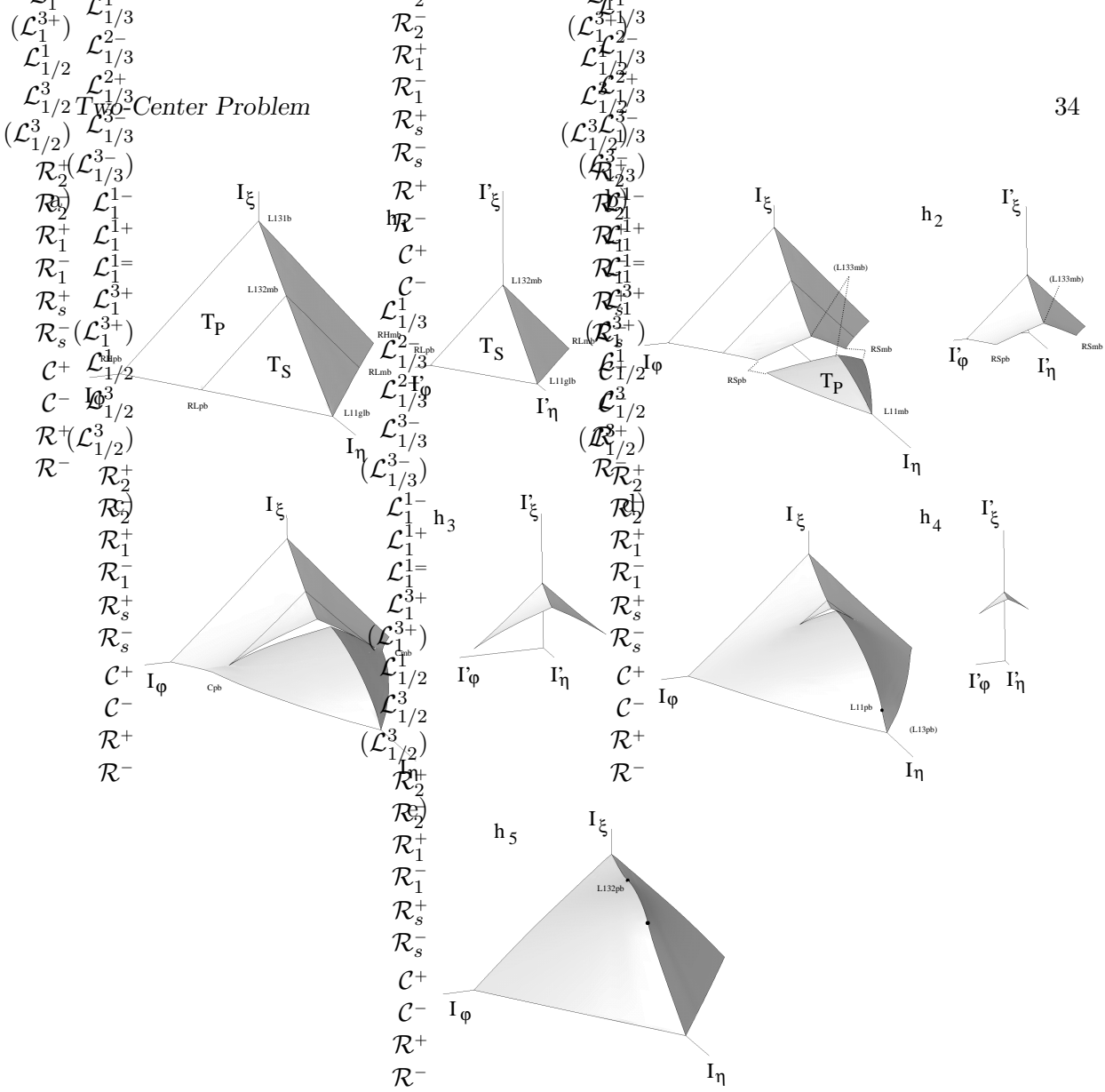


Figure 19: Energy surfaces in action space of the asymmetric two-center problem with  $\mu = 1/3$ . The five different energy values  $h_i$  are the same as in Fig. 13. For reasons of representation the scaling of the axes changes with the energy. For a constant scaling the "size" of the energy surfaces would grow with energy.

motion in phase  $\mathbf{T}_S$  which is confined to the center  $\mathbf{f}_1$ , with actions denoted by  $(I'_\varphi, I'_\eta, I'_\xi)$ .

The individual pictures show more or less tent-like structures. This is familiar from other studies of integrable systems with three degrees of freedom, such as rigid bodies [25] or ellipsoidal billiards [44, 53]. The lines of the bifurcation diagrams  $\Sigma_{g,l}^h$  are mapped to the boundaries of the tent; in this sense the individual parts of Fig. 19 may be viewed as very special versions of bifurcation diagrams. But they are more. Every inner point of the surface represents the actions  $(I_\varphi, I_\eta, I_\xi)$ , or  $(I'_\varphi, I'_\eta, I'_\xi)$ , of a 3-torus with energy  $h$ ; the surface normal gives the vector of frequencies  $(\omega_\varphi, \omega_\eta, \omega_\xi)$ , and rotation numbers may be obtained from the appropriate slopes, by generalization of Eq. (63). The most important application of these surfaces, however, is their use as a basis for semi-classical quantization. This will be discussed in connection with monodromy, in Sec. 7.

The corners of the tent structures represent the singular parts of the bifurcation diagram, as indicated by the same labels as in Fig. 13. This includes the cusps  $\mathcal{C}^\pm$  as well as the singular points  $\mathcal{L}_1^{1+}$  and  $\mathcal{L}_\mu^{2+}$ . Except for the latter two points and the corners  $\mathcal{L}_\mu^1$  and  $\mathcal{L}_1^{1=}$ , the edges at  $l = 0$  do *not* belong to the critical set. The following Sec. 6 will deal with attempts to construct action representations of  $\mathcal{E}_h$  which are smooth at  $l = 0$ .

The boundaries  $I_\eta = 0$  (or  $I'_\eta = 0$ ) connecting the corners  $\mathcal{L}_\mu^1$  and  $\mathcal{R}_2^\pm$  (or  $\mathcal{L}_\mu^{2-}$  and  $\mathcal{R}_1^\pm$ ) have action  $I_\eta = 0$ . They belong to the regular part of the critical set, corresponding to

stable RPOs as discussed in Sec. 4: motion along hyperboloids  $\eta = \text{const.}$  Similarly, the boundaries  $I_\xi = 0$  (or  $I'_\xi = 0$ ) connecting the corners  $\mathcal{L}_1^{1=}$  and  $\mathcal{R}_2^\pm$  (or  $\mathcal{L}_1^{1=}$  and  $\mathcal{R}_1^\pm$ ) have action  $I_\xi = 0$ . They are another regular part of the critical set, corresponding to stable RPOs: motion along ellipsoids  $\xi = \text{const.}$  In the energy range  $h_{c1} < h < h_c$  this boundary is interrupted by the occurrence of the unstable relative equilibria  $\mathcal{R}_s^\pm$ , from where a line of unstable RPOs extends across the tent and breaks it up into two pieces. The pre-images in phase space of the surfaces in  $(I_\varphi, I_\eta, I_\xi)$  and  $(I'_\varphi, I'_\eta, I'_\xi)$  space are connected along these RPOs. This is also true for the unstable RPOs connecting the cusps  $\mathcal{C}^\pm$  in the energy range  $h_c < h < h_{c3}$ , see pictures c) and d) in the Figure.

The essential structural features of the five different types of energy surfaces in action representation are the following.

1. For an energy  $h < h_{c1}$  the energy surface in action representation consists of two disconnected surfaces without inner singularities. They represent the two smooth families of 3-tori  $\mathcal{T}_H$  (the larger one) and  $\mathcal{T}_L$  (the smaller) in the respective energy surface. The line  $\mathcal{R}_1^+, \mathcal{L}_\mu^{2-}, \mathcal{R}_1^-$  separates regions  $\mathbf{T}_S$  and  $\mathbf{T}_P$  on the  $\mathcal{T}_H$ -surface, i. e., tori of family  $\mathcal{T}_H$  below this line coexist with tori with the same  $(h, g, l)$  of family  $\mathcal{T}_L$ . This line is no separatrix.
2. For an energy in the range  $h_{c1} < h < h_c$  the action representation of family  $\mathcal{T}_H$  consists of two disconnected pieces, separated by a line of unstable RPOs. In the original bifurcation diagram, the corresponding two families  $\mathcal{T}_H$  and the family  $\mathcal{T}_L$  are connected at this separatrix (attached to an unstable RPO) in a non-differentiable manner.
3. For an energy  $h_c < h < h_{c2}$  the family  $\mathcal{T}_H$  is again smoothly connected, though not simply connected. It contains an internal line of unstable RPOs which allows for a connection with the family  $\mathcal{T}_L$ . The surface corresponding to  $\mathcal{T}_L$  is always simply connected.
4. The new feature for an energy in the range  $h_{c2} < h < h_{c3}$  is the isolated singularity  $\mathcal{L}_1^{1+}$  on the edge  $l = 0$ . This adds another complication to the connectedness of  $\mathcal{T}_H$ .
5. At energies  $h > h_{c3}$  the family  $\mathcal{T}_L$  has disappeared, and  $\mathcal{T}_H$  is a surface with two point singularities.

To complete the presentation of actions  $(I_\varphi, I_\eta, I_\xi)$ , Fig. 20 shows the four different types of energy surfaces for the symmetric case  $\mu = 1/2$ . Corresponding to the sections at constant energy  $h$  in Fig. 15, the left parts exhibit the action representation for the full system, but it should be borne in mind that the component touching the  $I_\xi$ -axis appears twice: once for each of the two equal centers. This is not shown in separate pictures. Instead, the smaller part in each of the four illustrations shows the symmetry reduced system with actions  $(J_\varphi, J_\eta, J_\xi)$  where  $J_\varphi = I_\varphi/2$  and  $J_\xi = I_\xi$  in general,  $J_\eta = I_\eta/2$  in the phase  $\mathbf{T}_P$ . The latter energy surfaces have the nice property of being continuous even though they possess separatrices.

## 6 Smooth Actions and Monodromy

The edges  $l = 0$  of the energy surfaces appear naturally if the actions are defined through the separating coordinates, but the absence of singularities (except at  $\mathcal{L}_1^{1+}$ ,  $\mathcal{L}_\mu^{3-}$  and  $\mathcal{L}_\mu^{2+}$ ) indicates that they do not represent criticality. Therefore it should be possible to choose actions in terms of which the energy surfaces are smooth at  $l = 0$ . The aim of this section is to find out to what extent this can be done. It will be seen that smooth actions can be

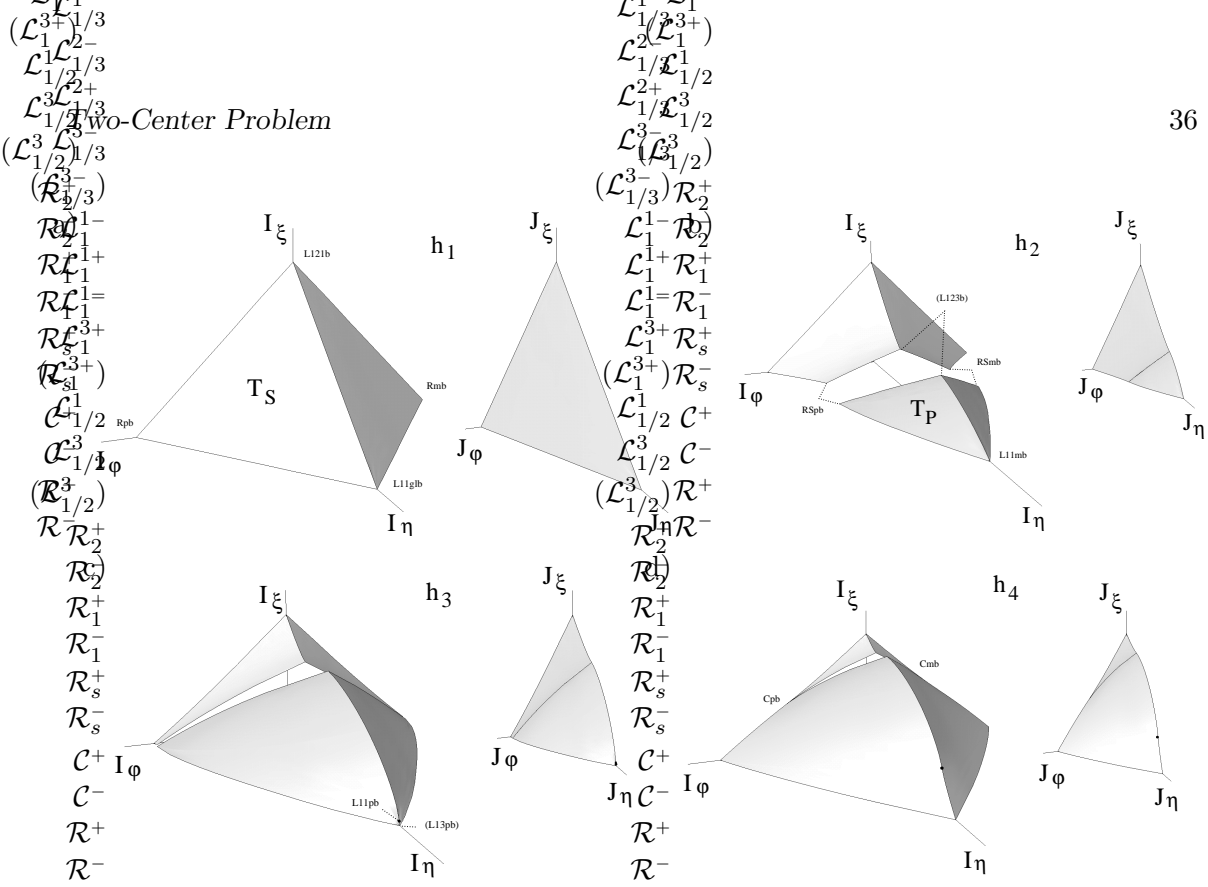


Figure 20: Energy surfaces of the symmetric two-center problem. The values of  $h_i$  are the same as in Fig. 15. For each value of  $h$ , the left part represents the full system while the right part includes symmetry reduction. As in Fig. 19 the scaling of the axes changes with energy for reasons of representation.

found along *pieces* of  $l = 0$ , but not simultaneously along the whole line. The points  $\mathcal{L}_1^{1+}$ ,  $\mathcal{L}_\mu^{3-}$  and  $\mathcal{L}_\mu^{2+}$  are obstacles which give rise to the phenomenon of *monodromy*.

Let us derive new actions  $\mathbf{K} = (K_\varphi, K_\eta, K_\xi)^t$  which coincide with the natural actions  $\mathbf{I} = (I_\varphi, I_\eta, I_\xi)^t$  for  $l \geq 0$ , and which continue smoothly to  $l < 0$ . For  $l < 0$  the actions  $\mathbf{K}$  must be related to the original actions by unimodular transformations  $\mathbf{M}$ :

$$\begin{pmatrix} I_\varphi \\ I_\eta \\ I_\xi \end{pmatrix} \mapsto \mathbf{M} \begin{pmatrix} I_\varphi \\ I_\eta \\ I_\xi \end{pmatrix} =: \begin{pmatrix} K_\varphi \\ K_\eta \\ K_\xi \end{pmatrix}. \quad (65)$$

The matrix  $\mathbf{M}$  has integer components and unit determinant. The requirement alone that the new actions shall be continuous at  $l = 0$  restricts  $\mathbf{M}$  to the form

$$\mathbf{M} = \begin{pmatrix} 1 & 0 & 0 \\ m_\eta & 1 & 0 \\ m_\xi & 0 & 1 \end{pmatrix}. \quad (66)$$

In order to determine the remaining integers  $m_\eta$  and  $m_\xi$  let us consider the derivatives of  $I_\eta$  and  $I_\xi$  with respect to  $l$  in the limit  $l \rightarrow 0+$ . The derivatives are

$$\frac{\partial I_s}{\partial l} = -\sigma_s \frac{l}{2\pi} \oint_{c_s} \frac{1}{z^2 - 1} \frac{dz}{w_s}. \quad (67)$$

Like the integrands in the action integrals (57), the integrands in Eq. (67) have poles at  $\pm 1$ , with residues

$$\text{Res}_{z=\pm 1} \frac{1}{z^2 - 1} \frac{dz}{w_s} = \pm \frac{1}{2} \frac{1}{\sqrt{-l^2}}. \quad (68)$$

The limit  $l \rightarrow 0$  calls for special attention because the branch points of the curves  $\Gamma_\eta$  and  $\Gamma_\xi$  approach the poles at  $\pm 1$ ; it must be checked whether the vanishing of the prefactor

$l$  in (67) is fast enough to compensate the divergence of the integral. In order to see what happens consider once more the integration paths on the curves for small angular momentum as shown in Fig. 18. To evaluate the integrals, it is advantageous to modify the integration paths by pulling them away from the branch points, but as indicated by the dashed lines, this leaves behind small integration paths which encircle the poles. The latter can be evaluated with the calculus of residues, while the contributions from the new large integration paths are finite as  $l \rightarrow 0$  so that the prefactor  $l$  makes them vanish for  $l = 0$ . The remarkably simple result for the integrals (67) in this limit is therefore

$$\lim_{l \rightarrow 0^+} \left( \frac{\partial I_\eta}{\partial l}, \frac{\partial I_\xi}{\partial l} \right) = \begin{cases} (-1/2, -1/2) & \text{for } \mathbf{T}_P \rightarrow \mathbf{t}_{s'} \text{ and } \mathbf{T}_S \rightarrow \mathbf{t}_s \\ (-1, -1/2) & \text{for } \mathbf{T}_P \rightarrow \mathbf{t}_1 \\ (-1, 0) & \text{for } \mathbf{T}_P \rightarrow \mathbf{t}_p \end{cases}. \quad (69)$$

Each collision of a pole and a branch point gives a contribution  $-1/2$ , independent of  $l$ . The same results with opposite signs hold for  $l \rightarrow 0^-$ . In the case  $\mathbf{T}_S \rightarrow \mathbf{t}_s$  the two families of tori give the same results. In the limits  $\mathbf{T}_P \rightarrow \mathbf{t}_p$  and  $\mathbf{T}_P \rightarrow \mathbf{t}_1$  the integrand in  $\partial I_\eta / \partial l$  has contributions from both poles  $\pm 1$ , see the second and the fourth row of the first column in Fig. 18. As indicated in the second row of the second column in Fig. 18, the integral  $\partial I_\xi / \partial l$  is non-critical in the limit  $\mathbf{T}_P \rightarrow \mathbf{t}_p$ , hence there is no need to modify the integration path.

As a byproduct of these results and the last column in the identity (56), we obtain resonances in the frequencies, as  $l \rightarrow 0^\pm$ :

$$\begin{aligned} \omega_\eta + \omega_\xi &= \pm 2\omega_\varphi && \text{for } \mathbf{t}_s \text{ and } \mathbf{t}_{s'}, \\ 2\omega_\eta + \omega_\xi &= \pm 2\omega_\varphi && \text{for } \mathbf{t}_1, \\ \omega_\eta &= \pm \omega_\varphi && \text{for } \mathbf{t}_p. \end{aligned} \quad (70)$$

The integers  $m_\eta$  and  $m_\xi$  in Eq. (66) can now be determined from equating the derivatives as  $l \rightarrow 0^+$  and  $l \rightarrow 0^-$ :

$$\lim_{l \rightarrow 0^+} \frac{\partial I_s}{\partial l} \stackrel{!}{=} \lim_{l \rightarrow 0^-} \frac{\partial K_s}{\partial l} = m_s + \lim_{l \rightarrow 0^-} \frac{\partial I_s}{\partial l} = m_s - \lim_{l \rightarrow 0^+} \frac{\partial I_s}{\partial l}. \quad (71)$$

It follows from Eq. (69) that  $m_\eta$  and  $m_\xi$  depend on whether the phases for  $l = 0$  are  $\mathbf{t}_{s'}/\mathbf{t}_s$ ,  $\mathbf{t}_1$  or  $\mathbf{t}_p$ . Accordingly, we get the three matrices

$$\mathbf{M}_s = \mathbf{M}_{s'} = \begin{pmatrix} 1 & 0 & 0 \\ -1 & 1 & 0 \\ -1 & 0 & 1 \end{pmatrix}, \quad \mathbf{M}_l = \begin{pmatrix} 1 & 0 & 0 \\ -2 & 1 & 0 \\ -1 & 0 & 1 \end{pmatrix}, \quad \mathbf{M}_p = \begin{pmatrix} 1 & 0 & 0 \\ -2 & 1 & 0 \\ 0 & 0 & 1 \end{pmatrix}. \quad (72)$$

The fact that these matrices are different implies that it is not possible to construct energy surfaces which are smooth across all four ( $l = 0$ )-phases simultaneously. Fig. 21 shows how the three transformations remove the corresponding sections of the edges  $l = 0$  of the energy surfaces. The representation in  $\mathbf{I}$ -space, see Fig. 19, is taken to  $\mathbf{K} = (K_\varphi, K_\eta, K_\xi)$ -space. The pictures coincide for  $l \geq 0$  but differ for  $l < 0$ . Let us consider the five energy values  $h = h_1, \dots, h_5$  in some detail.

The energy surface for  $h = h_1 < h_{c1}$  involves only the phases  $\mathbf{t}_s$  and  $\mathbf{t}_{s'}$ ; hence it becomes globally smooth with the transformation  $\mathbf{M}_s = \mathbf{M}_{s'}$ , see Fig. 21a. With decreasing  $h$ , the motion about the two centers is more and more Kepler-like, the two corresponding pieces of the energy surface become flatter and flatter. For energies  $h > h_{c1}$ , at least two types of transitions occur for  $l = 0$ . They are of type  $\mathbf{t}_s/\mathbf{t}_{s'}$  or  $\mathbf{t}_1$  for  $h = h_2, h_3$ , and of

type  $\mathbf{t}_s/\mathbf{t}_s'$ ,  $\mathbf{t}_1$  or  $\mathbf{t}_p$  for  $h = h_4, h_5$ . With actions  $\mathbf{K}$  chosen so that they are smooth across one transition, the other transitions still appear as edges with discontinuities in slope. Fig. 21b and c show the two sets of partially smooth surfaces at  $h = h_2$ , d and e the same for  $h = h_3$ . The three variations each at  $h = h_4$  and  $h = h_5$  are presented in the remaining six illustrations.

The essence of *monodromy* is displayed in these pictures: Consider for example the energy surface for  $h = h_4$ , see Fig. 22 and start with a point on the energy surface with actions  $\mathbf{K} = \mathbf{I}$  of a torus  $\mathbb{T}_{h,g,l}$  of family  $\mathbf{T}_p$  with  $l > 0$ . Fig. 22 shows three smooth paths on different partially smooth energy surfaces which connect this point to actions of the time reversed torus  $\mathbb{T}_{h,g,-l}$ . Since the partially smooth energy surface involve different smoothing matrices, the actions of  $\mathbb{T}_{h,g,-l}$  are different for all three paths. This means that there exist 1-parameter families of tori on the energy surface which start and end with the same torus, such that the action changes smoothly along the path, but the initial and final action are different.

The image of a connected smooth family of tori under the momentum map is a loop in  $(h, g, l)$  space. Monodromy within one energy surface in phase space can occur whenever a connected family of non-critical tori is not simply connected. For loops with constant energy this occurs for  $h > h_c$ . Depending on  $h$ , there exist up to homology (see below) one or two elementary paths with monodromy. One of them encircles the singularity  $\mathcal{L}_1^{1+}$  which appears when  $h$  grows larger than  $h_{c2}$ . The other case is more interesting; it emerges at  $h = h_c$  with a path that encircles not a point singularity but the slit between the cusps  $\mathcal{C}^\pm$ . This slit persists up to the energy  $h = h_{c3}$  where it shrinks to the singular point  $\mathcal{L}_\mu^{2+}$ . From there on, this point singularity inherits the monodromy property, see Fig. 13.

In order to understand the set of possible non-contractible loops of tori, the classification into phases  $\mathbf{T}_s$  and  $\mathbf{T}_p$  in  $(h, g, l)$ -space is not quite appropriate. For monodromy we need to classify *families of tori* in phase space. The difference occurs when the pre-image of the energy-momentum map has disjoint components. Then it is typical that only one component contains critical points, while the other is composed of regular points only. In the asymmetric two-center problem, this is the case with families  $\mathcal{T}_H$  (“heavy family”) and  $\mathcal{T}_L$  (“light family”). In the symmetric case, there are three families of tori, but only one of them, the pre-image of  $\mathbf{T}_p$ , contains non-contractible loops. We call it also the heavy family  $\mathcal{T}_H$ . In the following, we consider the image  $\mathcal{M}_3(\mathcal{T}_H)$  of the heavy family under the momentum mapping.

Now we can state: The heavy family in the two-center problem has monodromy. In Sec. 4 we discussed the singularities inside  $\mathcal{M}_3(\mathcal{T}_H)$ : the line of critical values  $\mathcal{L}_1^{1+}$  emanating from the point  $P$ , and the second more interesting obstacle which is two-dimensional in the energy range  $h_c < h < h_{c3}$ , connecting to the isolated line  $\mathcal{L}_\mu^{2+}$  ( $h > h_{c3}$ ) in the point  $D$ .

In order to give a comprehensive characterization of the monodromy of the system, it is useful to introduce the notion of homology (see [29] for an introduction). In particular, the first homology group  $H_1(\mathcal{M}_3(\mathcal{T}_H), \mathbb{Z})$  is the set of 1-cycles, or simply cycles for short, i. e., the set of oriented non-contractible closed loops. Cycles are considered to be equivalent in  $H_1(\mathcal{M}_3(\mathcal{T}_H), \mathbb{Z})$  if they can be smoothly transformed into each other. The operation of combining, or “adding”, cycles equips  $H_1(\mathcal{M}_3(\mathcal{T}_H), \mathbb{Z})$  with a natural Abelian group structure. It is established by choosing a basis in terms of non-equivalent paths  $p_1, p_2$ , which we choose according to Fig. 23, and then associating with any cycle  $p$  the pair of integers in the decomposition  $p = n_1 p_1 + n_2 p_2$ . Obviously, the first homology group of  $\mathcal{M}_3(\mathcal{T}_H)$  is  $H_1(\mathcal{M}_3(\mathcal{T}_H), \mathbb{Z}) = \mathbb{Z}p_1 + \mathbb{Z}p_2$ , i. e., it is isomorphic to  $\mathbb{Z}^2$ .

Let us examine how the actions change along the cycles  $p_1$  and  $p_2$ . In Fig. 23 the points (1) and (2) on  $p_1$ , and (3) and (4) on  $p_2$ , are located symmetrically with respect to



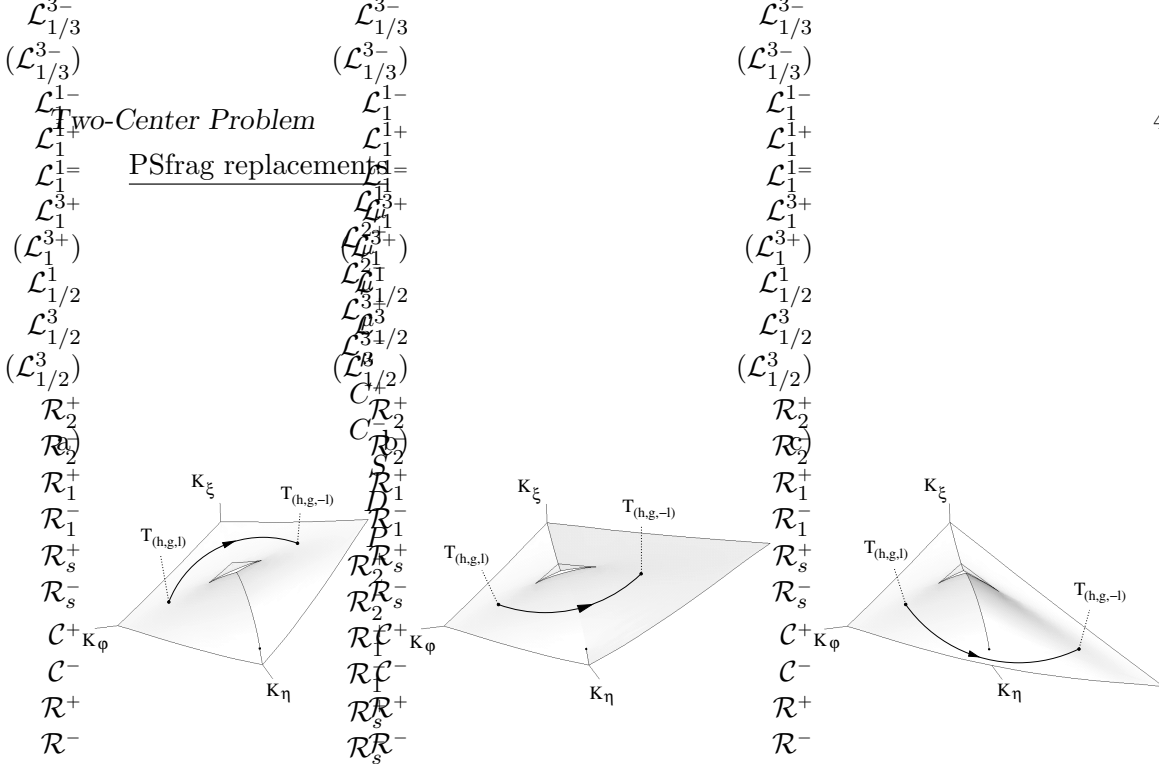


Figure 22: Partially smooth energy surfaces  $\mathcal{E}_h$  of the asymmetric two-center problem with  $h = h_4$  and smoothing matrices (a)  $\mathbf{M}_s$ ; (b)  $\mathbf{M}_i$ ; (c)  $\mathbf{M}_p$ .

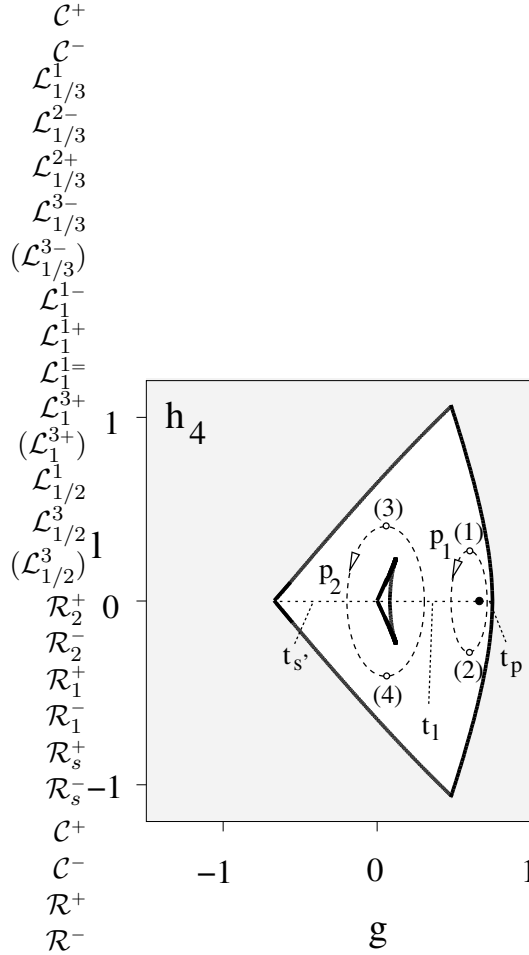


Figure 23: Cycles  $p_1$  and  $p_2$  in the plane  $h = h_4$  of the bifurcation diagram  $\Sigma_{g,t}^h$ , cf. Fig. 13.



the  $g$ -axis, i. e., they differ only in the sign of  $l$ . Consider first the cycle  $p_1$ . Starting at point (1) with the natural actions  $\mathbf{I} = (I_\varphi, I_\eta, I_\xi)^t$  and varying them smoothly along the left half of the cycle to point (2), it follows from the smoothing scheme described above that they are mapped to actions at (2) according to

$$\mathbf{I} \mapsto \tilde{\mathbf{M}}_l \mathbf{I}, \quad \tilde{\mathbf{M}}_l = \mathbf{M}_l \mathbf{R}_1 \quad (73)$$

where  $\mathbf{R}_1$  is the reflection matrix  $\text{diag}(-1, 1, 1)$ . Equivalently, the actions  $\mathbf{I}$  at point (1) are mapped to (2) along the right half of the cycle  $p_1$  according to

$$\mathbf{I} \mapsto \tilde{\mathbf{M}}_p^{-1} \mathbf{I}, \quad \tilde{\mathbf{M}}_p = \mathbf{M}_p \mathbf{R}_1. \quad (74)$$

The *monodromy matrix*  $\mathbf{M}_{p_1}$  of the cycle  $p_1$  is defined as the linear mapping from the actions at point (2) in Eq. (74) to the actions at point (2) in Eq. (73), i.e.

$$\mathbf{M}_{p_1} = \tilde{\mathbf{M}}_l \tilde{\mathbf{M}}_p^{-1} = \tilde{\mathbf{M}}_l \tilde{\mathbf{M}}_p = \begin{pmatrix} 1 & 0 & 0 \\ 0 & 1 & 0 \\ -1 & 0 & 1 \end{pmatrix} \quad (75)$$

where we used that the square of each of the matrices  $\tilde{\mathbf{M}}_s = \tilde{\mathbf{M}}_{s'}$ ,  $\tilde{\mathbf{M}}_l$  and  $\tilde{\mathbf{M}}_p = \mathbf{M}_p \mathbf{R}_1$  gives the identity matrix, i. e., each matrix coincides with its inverse. Monodromy is expressed by the fact that the matrix  $\mathbf{M}_{p_1}$  differs from the identity matrix. It describes a global twisting in the heavy family of 3-tori along the path  $p_1$ . Analogous considerations for the cycle  $p_2$  lead to the monodromy matrix

$$\mathbf{M}_{p_2} = \tilde{\mathbf{M}}_{s'} \tilde{\mathbf{M}}_l^{-1} = \tilde{\mathbf{M}}_{s'} \tilde{\mathbf{M}}_l = \begin{pmatrix} 1 & 0 & 0 \\ 1 & 1 & 0 \\ 0 & 0 & 1 \end{pmatrix}. \quad (76)$$

Note that  $\mathbf{M}_{p_1}$  only changes the  $\xi$ -component of  $\mathbf{I}$  while  $\mathbf{M}_{p_2}$  changes the  $\eta$ -component. As a consequence, the two matrices commute. This makes it easy to compute the monodromy for an arbitrary cycle  $p = n_1 p_1 + n_2 p_2$ :

$$\mathbf{M}_p = \mathbf{M}_{p_1}^{n_1} \mathbf{M}_{p_2}^{n_2} = \begin{pmatrix} 1 & 0 & 0 \\ n_2 & 1 & 0 \\ -n_1 & 0 & 1 \end{pmatrix} = \mathbf{1} + n_1(\mathbf{M}_{p_1} - \mathbf{1}) + n_2(\mathbf{M}_{p_2} - \mathbf{1}). \quad (77)$$

The Abelian character of the first homology group  $H_1(\mathcal{M}_3(\mathcal{T}_H), \mathbb{Z})$  is inherited by the monodromy group generated by  $\mathbf{M}_{p_1}$  and  $\mathbf{M}_{p_2}$ .

The billiard inside a rotationally symmetric ellipsoid also has monodromy [49]. In this case, however, there is only one isolated line of critical values in the image of the momentum map, and as a result it is possible to find a second action besides the angular momentum that is invariant for arbitrary loops. This is similar for the symmetric two-center problem, in which the action  $I_\xi$  is invariant. In the asymmetric case, however, it is not possible to find more than one action that is invariant under monodromy caused by both classes of loops.

## 7 Quantum Monodromy

The monodromy discussed in Sec. 6 has implications for the spectrum of the corresponding quantum system known as *quantum monodromy*. The quantum mechanical two-center

problem is described by the Hamiltonian operator

$$\hat{H} = -\frac{\hbar^2}{2m}\Delta - \frac{\mu_1}{r_1} - \frac{\mu_2}{r_2} \quad (78)$$

where we adopt the molecular interpretation:  $\mu_1 = Z_1e^2$ ,  $\mu_2 = Z_2e^2$ , and  $m$  is the mass of the electron. The main focus will be on the cases  $(Z_1, Z_2) = (1, 2)$  and  $(Z_1, Z_2) = (1, 1)$ , i. e., we consider the Born-Oppenheimer approximation to the molecular ions  $\text{HHe}^{++}$  and  $\text{H}_2^+$ , respectively. As with the classical problem we are only interested in bound states, hence we search for solutions of the stationary Schrödinger equation  $\hat{H}\psi = h\psi$  with  $\psi \in L_2(\mathbb{R}^3)$  and  $h < 0$ . In accordance with the notation of the previous sections,  $h$  denotes the energy and should not be confused with Planck's constant which will always be written as  $2\pi\hbar$ . It is convenient to perform the same scaling as in the classical case. Measuring distances in units of half the distance between the nuclei,  $a$ , and energy in units of  $(Z_1 + Z_2)e^2/a$ , the scaled stationary Schrödinger equation reads

$$\left( -\frac{\tilde{\hbar}^2}{2}\tilde{\Delta} - \frac{\mu}{\tilde{r}_1} - \frac{1-\mu}{\tilde{r}_2} \right) \psi = \tilde{h}\psi \quad (79)$$

where  $\tilde{\Delta}$  is the Laplacian in terms of scaled variables  $(x, y, z)/a$ , and  $\mu = Z_1/(Z_1 + Z_2)$ . Planck's constant is replaced by the dimensionless parameter

$$2\pi\tilde{h} = \frac{2\pi\hbar}{\sqrt{ame^2(Z_1 + Z_2)}}. \quad (80)$$

Except for the tilde indicating the scaled Planck's constant, the tildes will again be omitted in the following.

The eigenvalue equation (79) can be separated with the same coordinates  $(\varphi, \eta, \xi)$  that were defined in Equations (3) and (4) for the classical problem. The usual ansatz  $\psi(\varphi, \eta, \xi) = \phi(\varphi)\chi(\eta, \xi)$  leads to the eigenvalue problem of the angular momentum operator  $\hat{L}_z$  with eigenvalues and eigenfunctions

$$l_m = \tilde{h}m, \quad \phi_m(\varphi) = \exp(im\varphi), \quad m \in \mathbb{Z}. \quad (81)$$

The remaining function  $\chi$  fulfills

$$\frac{1}{\xi^2 - \eta^2}(\hat{H}_\xi + \hat{H}_\eta)\chi(\eta, \xi) = h\chi(\eta, \xi) \quad (82)$$

where

$$\hat{H}_\xi = -\frac{\tilde{\hbar}^2}{2}\left(\frac{\partial}{\partial\xi}(\xi^2 - 1)\frac{\partial}{\partial\xi} - \frac{m^2}{\xi^2 - 1}\right) - \xi, \quad (83)$$

$$\hat{H}_\eta = -\frac{\tilde{\hbar}^2}{2}\left(\frac{\partial}{\partial\eta}(1 - \eta^2)\frac{\partial}{\partial\eta} - \frac{m^2}{1 - \eta^2}\right) - (1 - 2\mu)\eta. \quad (84)$$

Eq. (82) can be separated with the ansatz  $\chi(\eta, \xi) = Y(\eta)X(\xi)$  which yields the couple of ordinary differential equations

$$\begin{aligned} -\frac{\tilde{\hbar}^2}{\xi^2 - 1}\frac{d}{d\xi}\left((\xi^2 - 1)\frac{d}{d\xi}\right)X(\xi) &= \frac{(\xi^2 - 1)(2h\xi^2 + 2\xi - 2g) - \tilde{\hbar}^2m^2}{(\xi^2 - 1)^2}X(\xi), \\ -\frac{\tilde{\hbar}^2}{1 - \eta^2}\frac{d}{d\eta}\left((1 - \eta^2)\frac{d}{d\eta}\right)Y(\eta) &= \frac{(1 - \eta^2)(-2h\eta^2 + 2(1 - 2\mu)\eta + 2g) - \tilde{\hbar}^2m^2}{(1 - \eta^2)^2}Y(\eta), \end{aligned} \quad (85)$$

$g$  being the separation constant. Eq. (85) allows for a direct comparison with the expressions for the separated momenta in the classical case, see Eq. (40). The separation constant  $g$  is the eigenvalue of the operator

$$\hat{G} = \frac{1}{\xi^2 - \eta^2} (\xi^2 \hat{H}_\eta + \eta^2 \hat{H}_\xi), \quad (86)$$

i. e., the set of equations (85) is equivalent to the set of equations  $\hat{H}Y(\eta)X(\xi) = hY(\eta)X(\xi)$  and  $\hat{G}Y(\eta)X(\xi) = gY(\eta)X(\xi)$ . Like in the classical case,  $\hat{G}$  can be decomposed into  $\hat{G} = \hat{H} + \hat{\Omega}$  [27]. With the total angular momentum operator  $\hat{\mathbf{L}} = -i\hbar(\mathbf{r} \times \nabla)$ , the operator  $\hat{\Omega}$  in Cartesian coordinate representation reads

$$\hat{\Omega} = \frac{1}{2} \left( \hat{\mathbf{L}}^2 + \tilde{\hbar}^2 \left( \frac{\partial^2}{\partial x^2} + \frac{\partial^2}{\partial y^2} \right) \right) + \mu \frac{z+1}{r_1} - (1-\mu) \frac{z-1}{r_2}, \quad (87)$$

cf. Eq. (12).

For the quantum mechanical two-center problem there are thus three mutually commuting observables  $\hat{H}$ ,  $\hat{G}$  and  $\hat{L}_z$ . The energy eigenstates can be chosen to be common eigenstates of all three observables, with triples of eigenvalues  $(h, g, l)$ . The joint spectrum  $\sigma_{(\hat{H}, \hat{G}, \hat{L}_z)}$  of  $\hat{H}$ ,  $\hat{G}$  and  $\hat{L}_z$  is obtained from solving Eq. (85). Technically, this is a coupled boundary value problem where both equations have regular singular points at  $\pm 1$  with indices  $\pm|m|/2$ , and an irregular singular point at infinity [39]. For the actual solution one has to resort to a numerical procedure as, e. g., described in [8, 7, 54].

The trace of the classical monodromy in the quantum system becomes apparent in a semiclassical analysis. The classical analogues of the quantum operators  $\hat{H}$ ,  $\hat{G}$  and  $\hat{L}_z$  are the classical phase space functions  $H$ ,  $G$  and  $p_\varphi$ . This can be made mathematically precise in the framework of so-called *microlocal analysis* (see e. g. [12]) so that  $H$ ,  $G$  and  $p_\varphi$  are the zeroth order terms, the *principal symbols*, in a power series expansion of the quantum operators with respect to the scaled Planck's constant (80). The first order semiclassical approximation of the joint spectrum  $\sigma_{(\hat{H}, \hat{G}, \hat{L}_z)}$  in this sense is given by the EBK quantization of the classical tori. Let us first consider the part of  $\sigma_{(\hat{H}, \hat{G}, \hat{L}_z)}$  located in the classical region  $\mathbf{T}_\mathbf{P}$ . Classically, the region  $\mathbf{T}_\mathbf{P}$  represents a single smooth three-parameter family of 3-tori (as opposed to region  $\mathbf{T}_\mathbf{S}$  where each  $(h, g, l)$  represents two 3-tori in phase space). In terms of the natural actions (55) the EBK quantization conditions for the 3-tori of type  $\mathbf{T}_\mathbf{P}$  are

$$I_\varphi = l = \tilde{\hbar}(m + \alpha_\varphi/4), \quad I_\eta = \tilde{\hbar}(n_\eta + \alpha_\eta/4), \quad I_\xi = \tilde{\hbar}(n_\xi + \alpha_\xi/4) \quad (88)$$

with quantum numbers  $(m, n_\eta, n_\xi) \in \mathbb{Z} \times \mathbb{N} \times \mathbb{N}$  and Maslov indices  $(\alpha_\varphi, \alpha_\eta, \alpha_\xi) = (0, 2, 2)$  corresponding to the fundamental paths defined in Eq. (54). The Maslov indices reflect the rotational character of the degree of freedom  $\varphi$  and the oscillatory character of  $\eta$  and  $\xi$  motion. In the space of the natural actions  $(I_\varphi, I_\eta, I_\xi)$  the quantum mechanical eigenvalues form a regular grid of mesh width  $\tilde{\hbar}$ . By (numerical) inversion of the mapping  $(h, g, l) \mapsto (I_\varphi, I_\eta, I_\xi)$ , this grid structure is transmitted smoothly to the space of the eigenvalues  $(h, g, l)$ . Here the fact that the natural actions  $\mathbf{I}$  are not smooth at  $l = 0$  is no problem because the EBK quantization conditions are invariant under a change to the different locally smooth actions  $\mathbf{K}$  defined according to Eq. (65). The actions  $\mathbf{K}$  fulfill again EBK quantization conditions of the form  $\mathbf{K} = \tilde{\hbar}(\mathbf{n} + \boldsymbol{\alpha})$  with a vector of integers  $\mathbf{n}$  and the same vector of Maslov indices  $\boldsymbol{\alpha} = (\alpha_\varphi, \alpha_\eta, \alpha_\xi)^t = (0, 2, 2)^t$ . The reason for this invariance is the fact that the vector of Maslov indices is an eigenvector, with eigenvalue 1, of each of the matrices  $\mathbf{M}_a$ ,  $a \in \{s', p, l\}$ , and the monodromy matrices  $\mathbf{M}_{p_1}$  and  $\mathbf{M}_{p_2}$ :

$$\mathbf{M}_a \boldsymbol{\alpha} = \mathbf{M}_{p_1} \boldsymbol{\alpha} = \mathbf{M}_{p_2} \boldsymbol{\alpha} = \boldsymbol{\alpha}. \quad (89)$$

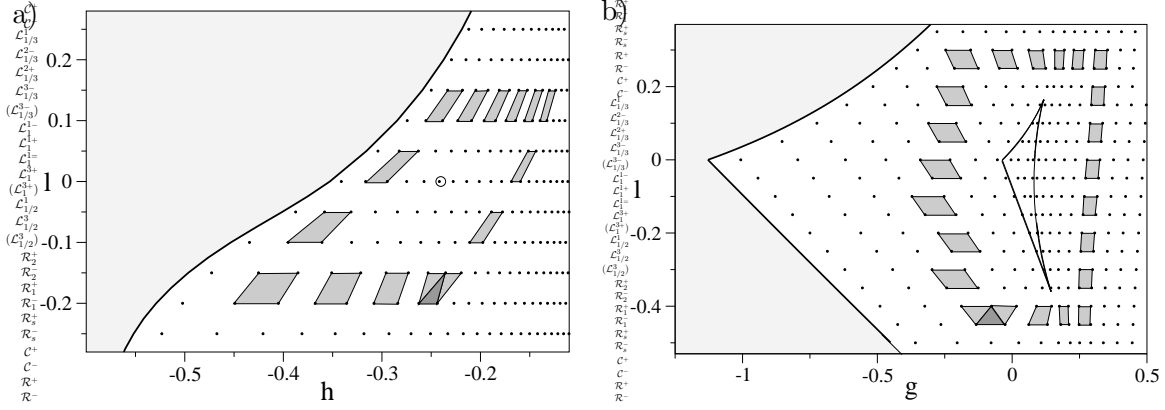


Figure 24: a) Surface of eigenvalues of Born-Oppenheimer  $H_2^+$  with  $n_\eta = 26$ . The left boundary corresponds to the right boundary in Fig. 15, in the sense that  $g$  is maximal as a function of  $l$  at fixed  $h$ . The open circle marks the intersection with  $\mathcal{L}_1^{1+}$ . b) Surface of eigenvalues of Born-Oppenheimer  $HHe^{++}$  with  $n_\xi = 11$ . The triangle in the middle corresponds to the kite shape singularity in Fig. 13. Both pictures are for  $\tilde{\hbar} = 1/20$ .

Such invariance was also found in [49, 48], and we believe that it holds generally in the context of monodromy.

The quantum monodromy of the two-center problem concerns the *global* topology of the grid of eigenvalues  $\sigma(\hat{H}, \hat{L}_z, \hat{G})$ . Since a three-dimensional picture would be too cumbersome we resort to illustrating the quantum monodromy by choosing certain subsets of eigenvalues located on smooth two-dimensional surfaces in  $\mathbf{T}_P$ .

Starting with the case of Born-Oppenheimer  $H_2^+$ , we look for a smooth surface in  $\mathbf{T}_P$  which intersects the line  $\mathcal{L}_1^{1+}$  transversely. A glance at Equations (65), (72), and (76) reveals that surfaces  $K_\eta = \tilde{\hbar}(n_\eta + 1/2)$  with  $n_\eta = \text{const}$  are a good choice: smoothing with either  $\mathbf{M}_l$  or  $\mathbf{M}_p$  gives the same action component  $K_\eta = I_\eta - 2I_\varphi$  for  $l < 0$  in both cases, and furthermore it is invariant under the monodromy transformation  $\mathbf{M}_{p_1}$ . We take  $n_\eta$  sufficiently large ( $n_\eta = 26$ ) and consider the two-dimensional subgrid of eigenvalues on this surface. Fig. 24a shows the projection of the corresponding grid of values  $(h, g, l)$  to the  $(h, l)$ -plane. The grid structure induced by the EBK quantization is evident. The non-trivial global topology of the grid becomes apparent if a lattice cell is transported along a closed path  $p_1$  around the intersection point with  $\mathcal{L}_1^{1+}$ . In accordance with the monodromy matrix  $\mathbf{M}_{p_1}$  this lattice cell returns sheared by one lattice site. Due to this lattice defect there are only two quantum numbers that allow for an unambiguous “smooth” numbering of the eigenstates. A possible choice of “good” quantum numbers in this sense would be  $n_\eta$  and  $m$ , or any combination thereof.

For Born-Oppenheimer  $HHe^{++}$  the quantum monodromy about the line  $\mathcal{L}_1^{1+}$  is of the same nature as in the case of  $H_2^+$ , and we omit the presentation of a separate figure. Instead we illustrate the monodromy associated with the non-local singularity which in a section at constant energy has the shape of a kite, see Fig. 13. A simple surface in action space that intersects this singularity transversely is obtained with  $K_\xi = \tilde{\hbar}(n_\xi + 1/2)$  and  $n_\xi = \text{const}$ , where  $K_\xi = I_\xi - I_\varphi$  for  $l < 0$  for both  $\mathbf{M} = \mathbf{M}_{s'}$  and  $\mathbf{M} = \mathbf{M}_l$ . The surface is invariant under  $\mathbf{M}_{p_2}$ . Fig. 24b shows the grid of eigenvalues on this surface in projection to the  $(g, l)$ -plane. Compared to the bifurcation diagrams  $\Sigma_{g,l}^h$  in Fig. 13, the kite shaped region here is distorted because the surface is not iso-energetic. The non-local defect of the eigenvalue lattice is detected from transporting a lattice cell along a closed path  $p_2$  around the singularity. In accordance with the monodromy matrix  $\mathbf{M}_{p_2}$ , the lattice cell returns sheared by one lattice site. If  $n_\xi$  is further increased the kite shaped region on  $K_\xi = \tilde{\hbar}(n_\xi + 1/2)$  eventually shrinks to a point in the Hopf bifurcation discussed in Sec. 4,

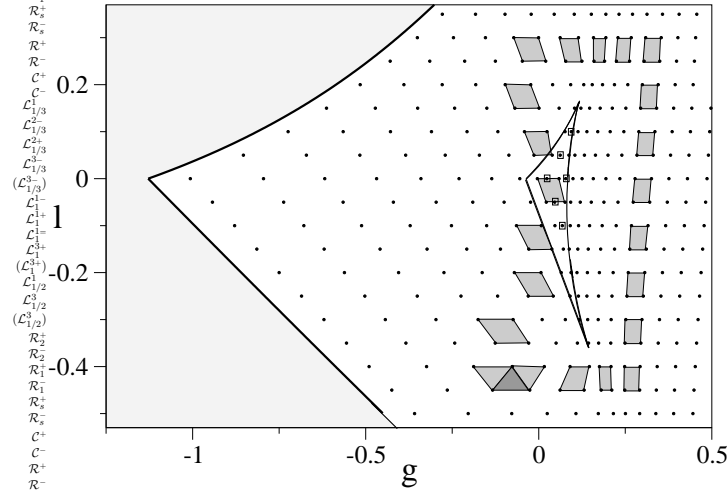


Figure 25: The same surface of eigenvalues of Born-Oppenheimer  $\text{HHe}^{++}$  as in Fig. 24b now with a different transport of a lattice cell. Small squares mark eigenvalues which correspond to tori of the light family  $\mathcal{T}_L$ .

and the quantum monodromy about this point gives a similar picture as in Fig. 24a.

For eigenstates with eigenvalues in  $\mathbf{T}_P$  and not too far from this singularity, there are again only two “good” quantum numbers, e. g.  $n_\xi$  and  $m$ . But for energies  $h > h_{c2}$  where both singularities coexist, neither  $n_\xi$  nor  $n_\eta$  are good quantum numbers; only the angular momentum number  $m$  remains as a globally useful label for the eigenstates of the Born-Oppenheimer  $\text{HHe}^{++}$  molecule.

Fig. 24b also shows quantum states in region  $\mathbf{T}_S$ , i. e., inside the kite. This is possible because  $K_\xi$  is smooth across the non-local singularity which is solely due to collisions of roots of the polynomial  $P_{1/3}^l(\eta)$  – the bifurcations of tori only involve the  $\eta$  degree of freedom. Within region  $\mathbf{T}_S$  there are two classical 3-tori for each  $(h, g, l)$ , and the EBK quantization in Eq. (88) has to be modified to incorporate the tunnelling between these tori. Semiclassically, this can be achieved by a so-called *uniform semiclassical quantization* [38, 14] based on a WKB ansatz for the separated quantum mechanical wave functions. For the two-center problem this has been worked out in detail in [35]. A refined treatment using the more general *phase integral method* can be found in the series of papers [3, 4, 5].

The higher density of the spectrum inside  $\mathbf{T}_S$ , as compared to the surrounding  $\mathbf{T}_P$ , reflects the existence of the two families of tori,  $\mathcal{T}_H$  and  $\mathcal{T}_L$ . As the two families are mixed by the tunnelling, it is not strictly possible to relate a given eigenstate to one or the other. But to the extent that the tunnelling effect is small (in particular, at small values of  $\tilde{h}$ ), the two families may be discerned in the spectrum. In this sense, the small squares in Fig. 25 can be said to belong to the family  $\mathcal{T}_L$  whereas the dots belong to the family  $\mathcal{T}_H$ . The distinction becomes more and more difficult near the right boundary of the kite where the two families merge along a separatrix. Consider now what happens at the left border of the kite. The family  $\mathcal{T}_L$  ceases to exist whereas the family  $\mathcal{T}_H$  continues smoothly across it and into the region  $\mathbf{T}_P$ . Accordingly, if only the lattice corresponding to tori  $\mathcal{T}_H$  is taken into account, it is possible to transport a lattice cell across the left boundary to the interior of region  $\mathbf{T}_S$ . The same is not possible at the right border which is a singularity for both families of tori.

## 8 Concluding Remarks

The present paper consists of two major parts. The first (Secs. 2-4) is a collection of largely known classical results on the qualitative dynamics of the two-center problem and its bifurcation behavior. The second (Secs. 5-7) is an analysis of the system in terms of action variables.

We found it useful to collect and present the existing information as it is widely scattered in the literature of more than 150 years, and has accordingly been expressed in a number of different frameworks. A coherent picture emerges when the energy momentum map from phase space to the space of constants of motion is introduced and analyzed for criticality. This method requires Liouville integrability of the system, but that was established early on for all versions of Euler's two-center problem: planar and three-dimensional, symmetric and asymmetric. Jacobi gave the clue for separation in terms of elliptic coordinates. He found an integral of the motion,  $G$ , generating a flow in phase space which is independent of the Hamiltonian flow and commuting with it. Like  $H$ ,  $G$  is not the generator of a compact symmetry group; its flow, in general, fills a 3-torus densely. But the combination of the invariance of  $H$  and  $G$  guarantees the integrability of the planar problem. Generalization to the three-dimensional problem is almost trivial because the compact symmetry group generated by the angular momentum  $p_\varphi$  may be factored out.

Standard methods were used to analyze the bifurcations of the energy momentum map. For the planar problem, the main result is presented in Fig. 3. The set of critical values  $(g, h)$  defines four regions of regularity for the asymmetric case, three for the symmetric. The regular types of motion were characterized by the topology of the Liouville tori. The set  $\Sigma^0$  of bifurcation values  $(g, h)$ , and the nature of their pre-images, were studied in detail, including the stability of critical periodic orbits. The corresponding results for the three-dimensional two-center problem were not given as a picture of the bifurcation set  $\Sigma$  in  $(h, g, l)$ -space, but rather in terms of its projections to the  $(h, l)$ -plane in Fig. 9, and its different types of cross section at constant  $l$  (Figures 10 and 11 for the asymmetric case, Fig. 14 for the symmetric) or at constant  $h$  (Fig. 13 for the asymmetric, Fig. 15 for the symmetric case). Of particular interest was the question how the two-dimensional bifurcation set  $\Sigma^0$  of the planar problem is contained in the more comprehensive set  $\Sigma$  of the full problem. The important finding was that although the values  $(h, g, l)$  belonging to the  $\mathbf{T_P}$  family of tori is a connected set, it is not simply connected but in its interior contains two sets of singularities: a one-dimensional line  $\mathcal{L}_1^{1+}$  and a fan like object which is two-dimensional in the energy range  $h_{c1} < h < h_{c3}$  but shrinks to the line  $\mathcal{L}_\mu^{2+}$  at energies  $h > h_{c3}$ .

In the second part we computed action variables and used them for a discussion of the system's quantum mechanics. The Liouville-Arnold theorem establishes the local existence of action variables in the regular regions of the conserved quantities; it leaves open the question to what extent these variables can be made global. We started with the computation of "natural" actions, those defined by the separating variables. It turned out that they are elliptic integrals of various kinds, depending on whether or not the system is planar and/or symmetric. The "surfaces" of constant energy  $h$  in action space are given in Figures 16 and 17 for the planar system (asymmetric and symmetric, respectively), and correspondingly for the full problem in Figures 19, 20. From these surfaces it is straightforward to discuss rotation numbers and questions of stability against perturbations, in the sense of the Kolmogorov-Arnold-Moser theorem. But rather than pursuing this question, we addressed the problem of finding, for the family of tori  $\mathbf{T_P}$ , global actions that are smooth at the pre-images of regular values  $(h, g, l)$ . Inspection of Fig. 19 shows that the natural actions do not quite fulfill this requirement: they exhibit discontinuities in slope for  $l = 0$  even though the bifurcation analysis had shown that, except for special values

$(h, g)$ , the line  $l = 0$  is regular.

The reason for the non-existence of globally smooth actions in  $\mathbf{T}_P$  was traced to the Hamiltonian monodromy of the two-center problem. The multiple connectedness of  $\mathbf{T}_P$  equips it with a homology group of type  $\mathbb{Z}^2$ , and each non-contractible cycle is associated with a non-trivial monodromy matrix which we calculated.

In the final part of the paper we showed that classical monodromy leads to quantum monodromy, i. e. the impossibility to label the lattice of quantum states globally and uniquely by quantum numbers. This was explicitly worked out for the molecular ions  $\text{HHe}^{++}$  and  $\text{H}_2^+$ , with the distance between the nuclei considered as fixed (Born-Oppenheimer approximation) and an effective Planck constant assumed unrealistically small. Therefore, the application to  $\text{HHe}^{++}$  and  $\text{H}_2^+$  should not be taken too serious, but Rydberg states in polyelectronic molecules might exhibit the properties discussed here if the bonding is maintained by the non-excited electrons.

## Acknowledgments

We are grateful to Axel Junge for supplying the data of his computation of the quantum spectrum of the two-center problem. P. H. R. expresses thanks to Hans-Joachim Scholz who participated in the very early stages of this work and with whom he produced an unfinished 16 mm scientific film on the matter. H. R. D. thanks Jim E. Howard for helpful discussions. This work was partially supported by the EU network HPRN-CT-2000-0113 *MASIE – Mechanics and Symmetry in Europe*. H. R. D was partially supported by EPSRC grant GR/R44911/01. H. W. acknowledges support from the Deutsche Forschungsgemeinschaft (Wa 1590/1-1).

## References

- [1] R. Abraham and J. E. Marsden. *Foundations of Mechanics*. Benjamin-Cummings, Reading, MA, 2nd edition, 1978.
- [2] V. I. Arnold. *Mathematical Methods of Classical Mechanics*, volume 60 of *Graduate Texts in Mathematics*. Springer, New York, 1978.
- [3] N. Athavan, P. O. Fröman, N. Fröman, and M. Lakshmanan. Quantal two-center Coulomb problem treated by means of the phase-integral method. I. General theory. *J. Math. Phys.*, 42(11):5051–5076, 2001.
- [4] N. Athavan, M. Lakshmanan, and N. Fröman. Quantal two-center Coulomb problem treated by means of the phase-integral method. II. Quantization conditions in the symmetrical case expressed in terms of complete elliptic integrals. Numerical illustration. *J. Math. Phys.*, 42(11):5077–5095, 2001.
- [5] N. Athavan, M. Lakshmanan, and N. Fröman. Quantal two-center Coulomb problem treated by means of the phase-integral method. III. Quantization conditions in the general case expressed in terms of complete elliptic integrals. Numerical illustration. *J. Math. Phys.*, 42(11):5096–5115, 2001.
- [6] W. G. Baber and H. R. Hassé. The two centre problem in wave mechanics. *Cambridge Phil. Soc. Proc.*, 31:564–581, 1935.
- [7] D. R. Bates and T. R. Carson. Exact wave functions of  $\text{HHe}^{2+}$ . *Proc. R. Soc. London, Ser. A*, 234:207–217, 1956.
- [8] D. R. Bates, K. Ledsham, and A. L. Stewart. Wave Functions of the Hydrogen Molecular Ion. *Philos. Trans. R. Soc. London, Ser. A*, 246:215–240, 1953.
- [9] A. Bolsinov, H. R. Dullin, and A. Wittek. Topology of energy surfaces and existence of transversal Poincaré sections. *J. Phys. A*, 29:4977–4985, 1996.
- [10] L. Brillouin. La mécanique ondulatoire de Schrödinger; une méthode générale de résolution par approximations successives. *C. R. Acad. Sci.*, 183:24–26, 1926.
- [11] C. Burrau. Über einige in Aussicht genommene Berechnungen betreffend einen Spezialfall des Dreikörper-Problems. *Vierteljahresschrift Astron. Ges.*, 41:261–265, 1906.
- [12] A.-M. Charbonel. Comportement semi-classique du spectre conjoint d’opérateur pseudo-différentiels qui commutent. *Asymptotic Analysis*, 1:227–261, 1988.
- [13] C. L. Charlier. *Die Mechanik des Himmels*. Veit & Comp., Leipzig, 1902.
- [14] M. S. Child. Semiclassical theory of tunneling and curve-crossing problems: a diagrammatic approach. *J. Mol. Spectroscopy*, 53:280–301, 1974.
- [15] M. S. Child. Quantum states in a champagne bottle. *J. Phys. A*, 31:657–670, 1998.
- [16] M. S. Child, T. Weston, and J. Tennyson. Quantum monodromy in the spectrum of  $\text{H}_2\text{O}$  and other systems: new insight into the level structure of quasi-linear molecules. *Mol. Phys.*, 96:371–379, 1999.
- [17] C. A. Coulson and A. Joseph. A constant of the motion for the two-centre Kepler problem. *Int. J. Quant. Chem.*, 1:337–347, 1967.



- [18] R. H. Cushman and L. M. Bates. *Global Aspects of Classical Integrable Systems*. Birkhäuser, Basel, Boston, Berlin, 1997.
- [19] R. H. Cushman and D. A. Sadovskii. Monodromy in perturbed Kepler systems: Hydrogen atom in crossed fields. *Europhys. Lett.*, 47:1–7, 1999.
- [20] R. H. Cushman and D. A. Sadovskii. Monodromy in the hydrogen atom in crossed fields. *Physica D*, 142:166–196, 2000.
- [21] A. Deprit. Le problème des deux centres fixes. *Bull. Soc. Math. Belg.*, 14:12–45, 1962.
- [22] Y. Duan and J. M. Yuan. Periodic orbits of the hydrogen molecular ion. *Eur. Phys. J. D*, 6:319–326, 1999.
- [23] Y. Duan, J. M. Yuan, and C. Bao. Periodic orbits of the hydrogen molecular ion and their quantization. *Phys. Rev. A*, 52(5):3497–3502, 1995.
- [24] J. J. Duistermaat. On global action-angle coordinates. *Comm. Pure Appl. Math.*, 33:687–706, 1980.
- [25] H. R. Dullin, M. Juhnke, and P. H. Richter. Action integrals and energy surfaces of the Kovalevskaya top. *Bifurcation and Chaos*, 4(6):1535–1562, 1994.
- [26] A. Einstein. Zum Quantensatz von Sommerfeld und Epstein. *Verh. DPG*, 19:82–92, 1917.
- [27] H. A. Erikson and E. L. Hill. A note on the one-electron states of diatomic molecules. *Phys. Rev.*, 75(1):29–31, 1949.
- [28] A. T. Fomenko. Topological classification of all integrable Hamiltonian differential equations of general type with two degrees of freedom. In T. Ratiu, editor, *The Geometry of Hamiltonian Systems*, pages 131–339, New York, 1991. Springer.
- [29] T. Frankel. *The Geometry of Physics*. Cambridge University Press, Cambridge, 1997.
- [30] J. M. Greene. A method for determining a stochastic transition. *J. Math. Phys.*, 20:1183–1201, 1979.
- [31] Cushman R. H. and J. J. Duistermaat. The quantum mechanical spherical pendulum. *Bull. Amer. Math. Soc.*, 19:475–479, 1988.
- [32] J. E. Howard and T. D. Wilkerson. Problem of two fixed centers and a finite dipole: a unified treatment. *Phys. Rev. A*, 52(6):4471–4492, 1995.
- [33] C. G. J. Jacobi. *Vorlesungen über Dynamik*. Chelsea Publ., New York, 1969.
- [34] G. Jaffé. Zur theorie des Wasserstoffmolekülions. *Z. Phys.*, 87:535–544, 1933.
- [35] A. Junge. *Analyse der Quantenspektren der Molekülionen  $H_2^+$  und  $HHe^{++}$* . Diplomarbeit, Universität Bremen, 2001.
- [36] J. B. Keller. Corrected Bohr-Sommerfeld quantum conditions for nonseparable systems. *Ann. Phys. (NY)*, 4:180–188, 1958.
- [37] H. A. Kramers. Wellenmechanik und halbzahlige Quantisierung. *Z. Phys.*, 39:828–840, 1926.
- [38] W. H. Miller. Semiclassical treatment of multiple turning-point problems - phase shifts and eigenvalues. *J. Chem. Phys.*, 48(4):1651–1658, 1968.

- [39] P. M. Morse and H. Feshbach. *Methods of Theoretical Physics*. McGraw-Hill, New York, 1953.
- [40] S. Vũ Ngọc. Quantum monodromy in integrable systems. *Commun. Math. Phys.*, 203:465–479, 1999.
- [41] S. Vũ Ngọc. Bohr-Sommerfeld conditions for integrable systems with critical manifolds of focus-focus type. *Commun. Pure Appl. Math.*, 53:143–217, 2000.
- [42] P. Pajunen.  $H_2^+$  as a tunneling problem; application of first-order and third-order JWKB approximation. *Mol. Phys.*, 43(4):753–771, 1981.
- [43] W. Pauli. Über das Modell des Wasserstoffmoleküls. *Ann. Phys. (Leipzig)*, 68:177–240, 1922.
- [44] P. H. Richter, A. Wittek, M. P. Kharlamov, and A. P. Kharlamov. Action integrals for ellipsoidal billiards. *Z. Naturforsch.*, 50a:693–710, 1995.
- [45] D. A. Sadovskii and B. I. Zhilinskii. Monodromy, diabolic points, and angular momentum coupling. *Phys. Lett. A*, 256:235–244, 1999.
- [46] M. P. Strand and W. P. Reinhardt. Semiclassical quantization of the low lying electronic states of  $H_2^+$ . *J. Chem. Phys.*, 70:3812–3827, 1979.
- [47] T. N. Thiele. Recherches numériques concernant des solutions périodiques d’un cas spécial du problème des trois corps. *Astron. Nachr.*, 138:1–10, 1896.
- [48] H. Waalkens. Quantum monodromy in trapped Bose condensates. *Europhys. Lett.*, 58:162–168, 2002.
- [49] H. Waalkens and H. R. Dullin. Quantum monodromy in prolate ellipsoidal billiards. *Ann. Phys. (NY)*, 295:81–112, 2002.
- [50] H. Waalkens, A. Junge, and H. R. Dullin. Quantum monodromy in the two-center problem. *J. Phys. A*, 36:L307–L314, 2003.
- [51] J. Waldvogel. *Die Verallgemeinerung der Birkhoff-Regularisierung für das räumliche Dreikörperproblem*. PhD thesis, ETH Zürich, 1966. Dissertation.
- [52] G. Wentzel. Eine Verallgemeinerung der Quantenbedingungen für die Zwecke der Wellenmechanik. *Z. Phys.*, 38:518–529, 1926.
- [53] J. Wiersig and P. H. Richter. Energy surfaces of ellipsoidal billiards. *Z. Naturforsch.*, 51a:219–241, 1996.
- [54] T. G. Winter, M. D. Duncan, and N. F. Lane. Exact eigenvalues, electronic wavefunctions and their derivatives with respect to the internuclear separation for the lowest 20 states of  $HHe^{2+}$  molecule. *J. Phys. B*, 10(2):285–304, 1977.
- [55] Nguyen Tien Zung. A note on focus-focus singularities. *Differential Geom. Appl.*, 7(2):123–130, 1997.